The ω-Amidase/NIT2 is a novel redox-sensitive key regulator of glutamine metabolism in endothelial cells

Dissertation
zur Erlangung des Doktorgrades
der Naturwissenschaften

vorgelegt beim Fachbereich
Biochemie, Chemie und Pharmazie
der Johann Wolfgang Goethe-Universität
in Frankfurt am Main

von Herrn Niklas Müller
aus Göttingen

Frankfurt am Main, 2022
(D30)

vom Fachbereich Biochemie, Chemie und Pharmazie der

Johann Wolfgang Goethe-Universität angenommen.

Dekan:	Prof. Dr. Clemens Glaubitz (Johann Wolfgang Goethe-Universität, Frankfurt)
Gutachter:	Prof. Dr. Alexander Gottschalk (Johann Wolfgang Goethe-Universität, Frankfurt)
	Prof. Dr. Katrin Schröder (Johann Wolfgang Goethe-Universität, Frankfurt)

Datum der Disputation: 21.07.2022

Contents

1. Introduction 1

1.1 Reactive oxygen species (ROS) 1

1.2 Endothelial cell metabolism 10

1.3 The Glutaminase II pathway 16

2. Aim of this study 21

3. Materials and methods 22

3.1 Materials 22

3.2 Methods 34

4. Results 52

4.1 DAO as a tool to study redox signaling in HUVECs 52

4.2 Metabolic and transcriptomic response of HUVECs upon exposure to different types of ROS 58

4.3 Redox-sensitivity of ω-amidase/NIT2 67

4.4 Deletion of ω-amidase/NIT2 affects endothelial function 73

4.5 Metabolic importance of the glutaminase II pathway in HUVECs 76

4.5 NIT2 interacts with key enzymes of glutamine metabolism 80

5. Discussion 85

5.1 Summary and significance of this work 85

5.2 DAO as a tool to study redox signaling 86

5.3 Redox-sensitivity of ω-amidase/NIT2 89

5.4 Physiological relevance of the glutaminase II pathway 92

5.5 NIT2 is associated with key enzymes of glutamine metabolism 94

5.6 Glutamine metabolism revised 95

6. Outlook 97

7. Deutsche Zusammenfassung 98

8. Bibliography 103
9. Appendix 130
9.1 Supplementary figures 130
9.2 Supplementary tables 134
9.3 List of figures 136
9.4 List of tables 138
9.5 Abbreviations 139
9.6 Declaration 143
9.7 Acknowledgements 145
9.8 Curriculum vitae 146
9.9 Publications 147
9.10 Selbstständigkeitserklärung 148

1. Introduction

1.1 Reactive oxygen species (ROS)

1.1.1 ROS and redox-homeostasis

The term reactive oxygen species (ROS) describes oxygen-derived free radicals such as superoxide anions ($O_2^{\bullet -}$), hydroxyl radicals ($HO^{\bullet}$) and non-radical species such as hydrogen peroxide (H_2O_2) [1–3]. They occur in various cell compartments including the cytoplasm, mitochondria or cell membrane as a part of normal metabolic function (**Fig. 1**) [4].

Superoxide anions are generated naturally as a leakage of the mitochondrial electron transport chain (complexes I and III) and as a side product of lipoxygenases or xanthine oxidases [5]. Furthermore, superoxide is released into the outer cellular space as the main effector of the oxidative burst in immune cells by the NADPH (nicotinamide adenine dinucleotide phosphate) oxidase NOX2 [6,7]. Due to its negative charge, superoxide cannot pass through the plasma membrane and reacts slowly and very unselectively as an oxidant. In the cell, superoxide dismutates to H_2O_2 catalyzed by cytosolic and mitochondrial superoxide dismutases (SOD) [8]. Moreover, H_2O_2 is generated by amine oxidases, dioxygenases, xanthine dehydrogenase, peroxisomes, dual oxidases or from the activity of the NADPH oxidase isozyme NOX4 [6,7,9]. Physiological intracellular H_2O_2 concentrations range from 1 – 10 nM and can reach up to approximately 100 nM. Furthermore, H_2O_2 has a relatively long life time (~10 s) compared to superoxide and hydroxyl radicals [10–12].

H_2O_2 carries no charge and can diffuse across cell membranes [13]. From a chemical point of view, H_2O_2 is a strong oxidant and shows some selective reactivity towards low pK_a thiols and transition metals in proteins [14]. Intracellular H_2O_2 concentrations are maintained within signaling (< µM) ranges by the enzyme catalase ($2\ H_2O_2 \rightarrow 2\ H_2O + O_2$), glutathione peroxidases and peroxiredoxins [1,12]. Therefore, H_2O_2 is an important mediator of redox signaling when generated at low concentrations and in a controlled manner [12,15]. In contrast, hydroxyl radicals are a product of the Fenton reaction in the presence of H_2O_2 and Cu^{2+} or Fe^{2+} but $HO^{\bullet}$ immediately reacts with biological molecules precluding it as a carrier of a redox signal [16,17].

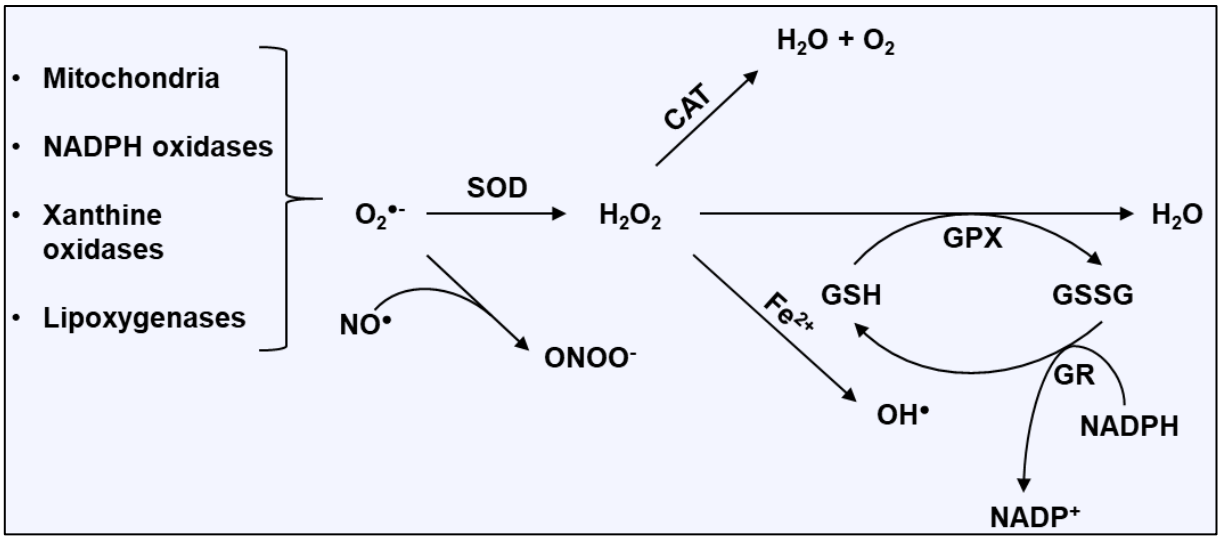

Figure 1. Sources of ROS in mammalian cells
The mitochondria, NADPH oxidases, xanthine oxidases and lipoxygenases are sources of superoxide anions in mammals. Superoxide ($O_2^{\bullet-}$) dismutates to hydrogen peroxide (H_2O_2) in a reaction catalyzed by superoxide dismutase (SOD). Furthermore, superoxide can react with nitric oxide ($NO^\bullet$) to generate peroxinitrite anions ($ONOO^-$). Transition metals in proteins drive the Haber-Weis reaction to generate hydroxyl radicals ($HO^\bullet$). Glutathione peroxidases (GPX) and catalase (CAT) reduce free hydrogen peroxide to water (H_2O). GSH represents the reduced monomeric glutathione while GSSG represents the oxidized glutathione disulfide (figure adapted from Allen *et al.* 2008 [1]).

Cells have evolved several defense mechanisms to control ROS production. This includes redox compartmentalization and an antioxidant system. Redox homeostasis is controlled by antioxidants that maintain ROS levels at physiological concentrations [18].

Low-molecular-weight compounds such as vitamins and glutathione (GSH, L-γ-glutamyl-L-cysteinylglycine) are essential to maintain redox homeostasis [19]. Reduced GSH is present in all cellular compartments and is thus the major soluble antioxidant. Its antioxidant effects are manifested in several ways: GSH detoxifies H_2O_2 and lipid peroxides in reactions catalyzed by glutathione peroxidase (GSH-Px) [20]. Additionally, GSH can donate an electron to H_2O_2 to generate H_2O and O_2. Nevertheless, this reaction is very slow and therefore unlikely to occur in a biological system. The ratio of reduced glutathione (GSH) to oxidized glutathione (GSSG) is an important determinant of the cellular redox state. GSSG is reduced back to GSH by the GSH reductase (GSR) which uses NAD(P)H as an electron donor. Glucose-6-phosphate dehydrogenase (G6PD), the first and rate limiting step of the pentose phosphate pathway (PPP), reduces $NADP^+$ to produce NADPH by converting glucose-6-phosphate to 6-phosphogluconolactone. Therefore, the enzyme is an important

determinant of the GSH buffering capacity (GSH/GSSG) and an essential antioxidant enzyme [19–22].

The major antioxidant enzymes are superoxide dismutase (SOD), heme-dependent catalase (CAT) and selenium-dependent glutathione peroxidases (GSH-Px). Additionally, other proteins such as heme oxygenase-1 (HMOX-1) and specialized redox proteins like thioredoxins (TRX), thioredoxin reductase (TRR), peroxiredoxins (PRX) and glutaredoxins (GLRX) have to be considered [19].

As superoxide is the primary type of intracellular ROS, dismutation to H_2O_2 catalyzed by SOD is a key aspect of the antioxidant response to maintain superoxide levels low. Mammals express three different SOD isozymes: CuZn-SOD, Mn-SOD, and EC-SOD [19]. CuZn-SOD resides in the cytosol and Mn-SOD is localized in the mitochondrial matrix. EC-SOD is secreted into the extracellular space and binds to matrix proteins. H_2O_2 generated by SOD enzymes can be reduced to H_2O by catalase and by other enzymes [19,23].

Importantly, GSH-Pxs are part of the redox cycle to reduce H_2O_2. They are a family of tetrameric enzymes containing a selenocysteine in the active center. In the course of H_2O_2 detoxification, the selenol of GSH-Px is oxidized and subsequently re-reduced by two GSH molecules to form GSSG [24,25]. In humans, four different selenium-containing GSH-Pxs isozymes are expressed: GSH-Px-1 is the most abundant isozyme that reduces both H_2O_2 and fatty acid peroxides but it does not reduce esterified peroxyl lipids. Those are reduced by the membrane-bound isozyme GSH-Px-4. GSH-Px-2 is expressed in the gastrointestinal track while GSH-Px-3 resides in the extracellular compartment, especially in plasma [19,22,26].

Furthermore, thiol-containing enzymes such as thioredoxins, thioredoxin reductase and peroxiredoxins are closely associated with the disposal of H_2O_2. Peroxiredoxins are oxidized at their functional cysteines and then are restored by thioredoxin in conjunction with NADPH-dependent thioredoxin reductase [24]. Humans express two different TRX and TRR isozymes existing in both cytosol and mitochondria while there are six different isozymes of PRXs (1-6) that differ in their compartmentalization. All of these antioxidants require NADPH as a reducing equivalent which maintains the active form of catalase and is a cofactor of TRX and GSH reductase [19].

1.1.2 Redox signaling

For decades, ROS were classified as harmful by-products of cellular aerobic metabolism as they can oxidize DNA, lipids or proteins. This led to the concept of oxidative stress which is considered to be a central feature of several physiological dysfunctions such as cancer, diabetes and atherosclerosis [15,27,28,28,29]. This changed with the observation that exogenous H_2O_2 could mimic growth factor activity as increasing levels of ROS can activate signaling pathways such as growth-factor-induced receptor tyrosine phosphorylation [30,31]. It is currently accepted that ROS production in a controlled manner in response to growth factors, cytokines and calcium signals can elicit redox signaling [4,27,30].

The term redox signaling describes a process of signaling events that occur upon a change in the oxidation state of a signaling molecule. The amino acid cysteine is the main target for oxidation in proteins but also unsaturated fatty acids, the amino acid methionine or transition metals can be oxidized [32]. Proteins that contain low pK_a cysteine residues (in the thiolate form, S^-) can selectively be oxidized by H_2O_2 leading to changes in charge, size, hydrophobicity, and polarity of a protein which consequently changes its tertiary structure [33,34]. This oxidation forms a sulfenic acid (-SOH) which can react with another thiol close-by to form a disulfide bridge. This directly affects the secondary, and the tertiary structure of the protein. Additionally, the formation of mixed disulfides such as *S*-glutathionylation of cysteine residues is considered to be another important redox modification with considerable steric effects on target proteins [24,33]. High concentrations of H_2O_2 can further oxidize the thiolate anion to sulfinic ($-SO_2H$) or sulfonic ($-SO_3^-$) acid (**Fig. 2**) [30,35].

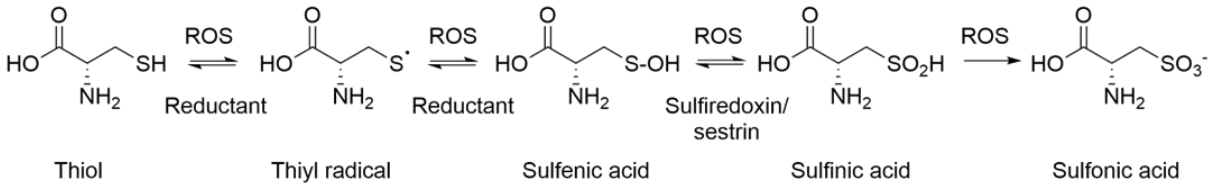

Figure 2. Cysteine residues and their different oxidation states
ROS such as H_2O_2 can oxidize cysteine residues to sulfenic acid which can be reduced back by different reductants such as GSH and thioredoxin. Further oxidation of sulfenic acid to sulfinic acid can be reduced specifically by sulfiredoxin. The oxidation to sulfonic acid is not reversible (figure adapted from Jortzik *et al.* 2012 [35]).

Cysteine (together with tryptophan) is the least abundant amino acid in proteins but around 90% of cysteine residues are evolutionary conserved showing their importance as structural elements, for redox reactions and redox signaling events [10,32,33]. Disulfide bridges are essential for correct protein folding but exposed cysteine residues (e.g. at the protein surface) are also accessible to oxidative modifications and therefore likely to be redox-active. Some surface cysteines are thought to act as scavengers protecting a catalytic cysteine from oxidation [24]. Furthermore, a buried cysteine can become accessible to oxidation by a protein conformational change. Interestingly, epidermal growth factor (EGF) contains cysteine residues with specified oxidation patterns that are regulated by redox-independent structural regulation of EGF-downstream targets [36].

Nevertheless, many redox-regulated proteins such as phosphatases, kinases or transcription factors show moderate reactivity with H_2O_2 and are often expressed at a low level. Therefore, the specificity and efficiency of H_2O_2 as a signaling molecule is a complex topic [37–39]. One theory, the *floodgate* model, suggests that it is essential to overcome the redox buffering capacity provided by peroxiredoxins, so H_2O_2 can directly oxidize target proteins. Peroxiredoxins are H_2O_2 scavengers that harbor a peroxidatic cysteine which can be oxidized to a sulfenic acid (-SOH) by H_2O_2. This sulfenic acid typically reacts with another thiol close-by to form a disulfide bond. Within their catalytic cycle, this disulfide bond is usually reduced by thioredoxin. When H_2O_2 concentrations are high, peroxiredoxins can be hyperoxidized at their catalytic cysteine to form a sulfinic ($-SO_2H$) or sulfonic acid ($-SO_3^-$) which inactivates their catalytic activity [40,41]. This would allow endogenous H_2O_2 concentrations to build up which promotes redox signaling by direct oxidation of target proteins and other biomolecules [42].

The other theory is called the *redox-relay* hypothesis [43]. Based on the observation that the reaction of H_2O_2 with thiols is too slow to outcompete peroxiredoxins, it has been postulated that peroxiredoxins indirectly facilitate H_2O_2 sensing and oxidize target proteins [39,44–46]. Peroxiredoxins are so sensitive to H_2O_2 that they might outcompete other potential target proteins and thereby act as carriers of a redox signal [47]. Mammalian peroxiredoxins transfer H_2O_2-derived oxidizing equivalents to the transcription factor STAT3 or to the kinases ASK1 and MEKK4 [39,45,46,48]. It is likely that both mechanisms occur within the cell.

1.1.3 Redox-dependent metabolic function

Several metabolic enzymes have been identified that are susceptible to oxidative modifications. Those modifications occur in both cytosolic (e.g. enzymes of the glycolysis) as well as in mitochondrial enzymes (e.g. tricarboxylic acid (TCA) cycle enzymes). Rewiring of cell metabolism is a key for the ability of cells to cope with oxidative and environmental cues [24,49].

Cytosolic AMP-activated protein kinase (AMPK) is an important regulator of several metabolic pathways. Dysregulation of AMPK is associated with oxidative stress-related diseases. The enzyme senses ADP/ATP and AMP/ATP ratios, activating glucose and fatty acid uptake in times of low cellular energy reserves. Interestingly, AMPK activity is regulated by its intracellular redox state making it a role model for a redox-controlled metabolic enzyme [50]. AMPK activation is regulated by H_2O_2-mediated *S*-glutathionylation of Cys299 and Cys304 under energy-sufficient conditions [51]. Interestingly, oxidative modifications can also have opposite effects on AMPK activity. Peroxynitrite-dependent AMPK phosphorylation occurs at Thr172 that leads to phosphorylation of acetyl-CoA carboxylase at Ser79. This modification inactivates AMPK which leads to an increase in fatty acid oxidation [52].

Numerous other enzymes have been shown to be regulated by redox-dependent modifications. For example: endothelial nitric oxidase synthase (eNOS) can generate superoxide anions through its oxygenase domain when the co-factor tetrahydrobiopterin (BH_4) is missing. The generated superoxide reacts with the synthesized nitric oxide (NO) to form peroxynitrite ($ONOO^-$) [4]. $ONOO^-$ enhances the pentose phosphate pathway (PPP) activity by stimulation of glucose-6-phosphate dehydrogenase leading to elevated levels of NADPH. This is consistent with H_2O_2-depedent inactivation of glyceraldehyde 3-phosphate dehydrogenase (GAPDH) leading to an increase in metabolites of the upper glycolysis pathway which then will be metabolized by the PPP to generate NADPH [53,54]. From a signaling point of view, short term activation of the PPP may be cell protective by increasing reducing equivalents while chronic stimulation of this pathway will constantly raise NADPH concentrations which can lead to an excessive production of ROS by NOX enzymes [4,55].

As previously mentioned, mitochondria are a source of ROS (**Fig. 3**) [4,24]. Briefly, electrons from NADH enter the respiratory chain at complex I. When the NADH/NAD^+ ratio is high, superoxide anions are released into the matrix by the interaction of O_2 with reduced flavin mononucleotide (FMN). Mitochondria can also generate ROS by *reverse* electron transfer (RET), a process that drives electrons from reduced ubiquinol back towards complex I. When succinate concentrations are high, succinate is oxidized by intact mitochondria. Thereby the concentration of reduced ubiquinol increases. Complex I can then catalyze a *reverse* electron transfer when electrons from reduced ubiquinol are transferred back to complex I by the proton motive force [4,56].

Interestingly, several mitochondrial enzymes are susceptible to oxidative modifications what regulates their activity. The pyruvate dehydrogenase complex (PDHC) converts pyruvate, the final product of glycolysis, to acetyl-CoA. Pyruvate dehydrogenase (PDH) – the first enzyme in the PDHC – is inhibited by the pyruvate dehydrogenase kinase 2 (PDHK2) regulating the entry of pyruvate into the TCA cycle. This mechanism is controlled in a redox-sensitive manner via reversible oxidation of Cys45 and Cys392 in PDHK2 which increases the activity of PDH [57]. Within the TCA cycle, aconitase and the α-ketoglutarate dehydrogenase complex (αKGDHC) can be modified by ROS. Aconitase isomerizes citrate to isocitrate and is inhibited by superoxide anions which temporally oxidize the iron-sulfur cluster [58,59]. αKGDHC can undergo ROS-mediated inhibition by reversible *S*-glutathionylation of the lipoic acid binding site of the E2 enzyme component. This temporarily shuts down the enzyme and reduces NADH production along with the mitochondrial respiratory capacity [60].

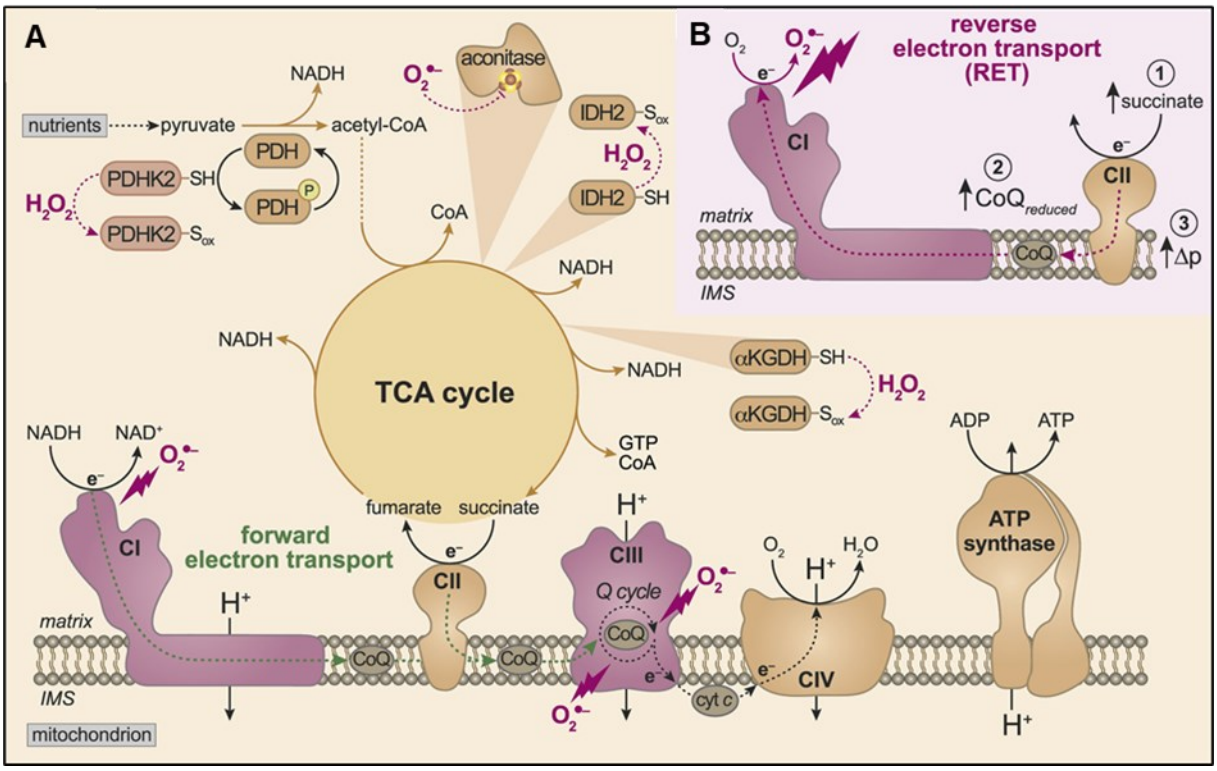

Figure 3. Mitochondria as a source of ROS and their effects on energy metabolism
(**A**) The mitochondrial electron transport chain (ETC) including the complexes I – IV. Pyruvate, the final product of glycolysis, is converted to acetyl-CoA by the pyruvate dehydrogenase complex (PDHC). The activity of pyruvate dehydrogenase (PDH) – the first enzyme component of the PDHC – is regulated by phosphorylation catalyzed by the redox-sensitive kinase PDHK2. Furthermore, several TCA cycle enzymes such as aconitase or the α-ketoglutarate dehydrogenase complex (αKGDHC) are susceptible to oxidative modifications. (**B**) Reverse electron transfer (RET) occurs when electrons from succinate enter the ETC but are passed from reduced coenzyme Q (CoQ) back to complex I. Thereby superoxide anions are generated (figure from Lennicke and Cochemé 2021 [24]).

1.1.4 Redox-related changes in gene expression

ROS play an important role downstream of physiological signal cascades. Changes in gene expression are a central aspect of cellular stress defense that include pro-survival gene expression programs for ROS detoxification, DNA damage repair or cell-death-induction. Furthermore, several transcription factors (TF) are regulated in a redox-dependent manner [24,61].

NRF2 (nuclear factor erythroid 2-related factor 2) senses changes in cellular redox status by its adaptor protein KEAP1 (Kelch-like ECH-associated protein 1). Upon binding of KEAP1, NRF2 is ubiquitinated and degraded by the proteasome. An increase in ROS levels will lead to oxidation of cysteine residues in KEAP1, inducing a conformational change and releasing NRF2 which will translocate into the nucleus. NRF2 is a basic leucine zipper (bZIP) transcription factor facilitating the expression of

antioxidant proteins such as heme oxygenase-1 or thioredoxin reductase 1 [62–65]. Several NRF2 target genes are important mediators of redox homeostasis generating required cofactors (e.g. GSH and NADPH) [24].

Nuclear factor kappa B (NF-κB) is important to mediate the inflammatory response, cell proliferation and cell death [66]. This TF is activated by a phosphorylation cascade which leads to the degradation of its inhibitor IκB [24,67]. The NF-κB signaling pathway is controlled in a redox-dependent way by two mechanisms: First, by H_2O_2-mediated activation of the inhibitor of nuclear factor kappa-B kinase (IKK) which leads to the phosphorylation of IκB and thereby to its proteasomal degradation. Second, by the oxidation of a cysteine residue of the p50 subunit in NF-κB. This subunit is part of the DNA-binding domain and its oxidation decreases the transcriptional activity of NF-κB [24,68–71].

Furthermore, hypoxia-inducible factor 1α (HIF1α) is a TF essential for the cellular response to decreased oxygen levels [72]. Its redox-sensitive inhibitor, prolyl hydroxylase domain-containing protein 2 (PHD2), hydroxylates HIF1α in normoxic conditions leading to the degradation of HIF1α. With increasing levels of ROS, cysteine residues in PHD2 are oxidized which leads to the formation of a disulfide bond-mediated PHD2 homodimer. Thereby, PHD2 is inactivated and HIF1α can be stabilized in normoxia [24,73,74]. Similarly, transcription factors of the forkhead box O (FOXO) family can undergo disulfide-mediated dimerization with transportin (TNPO). This enhances its nuclear import to regulate gene expression [24,75].

Under physiological conditions, the tumor suppressor p53 maintains redox-homeostasis by encoding for genes with antioxidant functions (e.g. GPX1 and SOD2). Furthermore, it regulates genes related to the cell cycle, apoptosis and DNA repair to ensure cell survival and functionality. However, under persistent oxidative stress, p53 becomes hyperactivated and exhibits pro-oxidative activities [76]. This leads to cell death or cell cycle arrest. Therefore, p53 exhibits dual regulation of oxidative metabolism by inhibiting or inducing cellular senescence [61,77,78].

1.2 Endothelial cell metabolism

1.2.1 Principles of endothelial cell metabolism and angiogenesis

The vascular system is entirely lined by a single layer of endothelial cells (ECs) forming a barrier to facilitate the exchange of nutrients and oxygen between the bloodstream and surrounding tissues. ECs can change from quiescence to a highly proliferative state upon pro-angiogenic stimuli, primarily through vascular endothelial growth factor (VEGF). Furthermore, ECs produce ATP mainly via glycolysis while oxidizing only <1% of the generated pyruvate in the tricarboxylic acid (TCA) cycle [79–83]. This is supported by the fact that high nitric oxide (NO) levels inhibit mitochondrial respiration and a high glycolytic rate reduces oxygen consumption [84–86].

It has become apparent that endothelial cell metabolism is a key driver in processing a pro-angiogenic stimulus. During angiogenesis, new capillaries sprout from pre-existing vessels following a gradient of angiogenic stimuli. Angiogenesis is driven by the surrounding tissue´s requirements for nutrients and oxygen. This triggers the production of VEGF and other pro-angiogenic stimuli. When VEGF reaches the existing vessel it binds to its receptor (VEGFR2) on ECs whereby the pre-existing vessel “relaxes” and a new sprout may arise. Thereby, endothelial cell-cell contacts loosen and the pericytes detach leading to a breakdown of the basement membrane [81,87]. The process of retinal angiogenesis has been studied intensively showing that it occurs in a highly organized manner. The endothelial cell that is exposed to the highest amounts of VEGF becomes a so called “tip cell”. This cell leads the new sprout in the direction of the growth factor source. During the migration process the sprout elongates by multiplying the number of “stalk cells” that follow the tip cell [80,81,88].

The specification process between tip and stalk cells is highly dynamic and depends on selection of the “fittest” ECs for the tip position. This process is termed “tip cell overtaking” [89]. The tip cell expresses the Notch ligand delta-like 4 (DLL4) which binds to Notch receptors in adjacent ECs. This causes the Notch intracellular domain (NICD) to be released, which reduces VEGFR2 expression while increasing VEGFR1 expression. The increased ratio between VEGFR1/VEGFR2 imposes a stalk cell phenotype by lowering the responsiveness to VEGF [81]. This leads to continuous “cell shuffling” keeping the ECs with the lowest VEGFR1/VEGFR2 ratio at the tip position.

Recent research shows that metabolic pathways (e.g. glucose and glutamine metabolism) are essential for vessel sprouting and genetic signaling (**Fig. 4**) [83,90–93]. These findings show the importance of understanding endothelial cell metabolism regarding the limited success of growth factor-centric treatment therapies in pathological angiogenesis [81,94]. Certainly, the endothelium, by dysfunction or excessive sprouting, can be the origin of some severe and often lethal diseases [81].

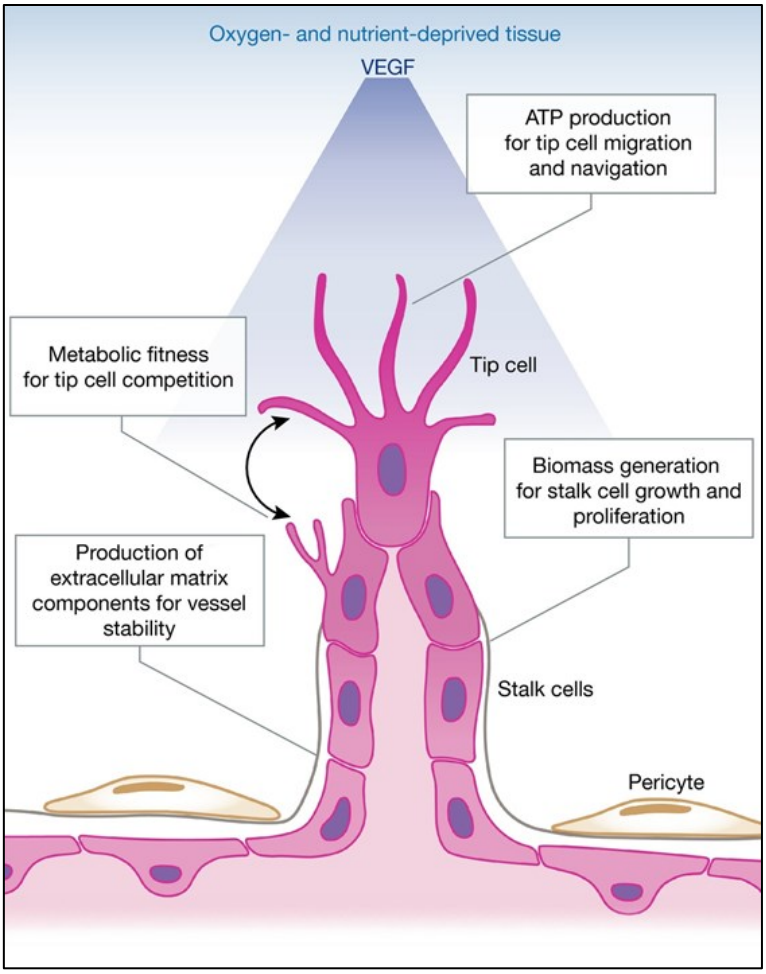

Figure 4. Metabolic demands of angiogenesis
Endothelial cells (ECs) can invade avascular tissues and thereby face metabolic challenges. A VEGF gradient (shown in blue) can activate ECs to proliferate, sprout and migrate. In the process of sprouting, ECs increase their ATP as well as their biomass production which is essential for angiogenesis (figure from Andrade and Potente 2017 [93]).

1.2.2 Glucose metabolism of endothelial cells

ECs energy production, in the form of ATP, highly relies on glycolysis instead of oxidative phosphorylation. In human umbilical vein endothelial cells (HUVECs), the glycolytic flux was considered to be >200-fold higher than glucose oxidation [83]. This matches the fact that ECs have a relative small mitochondrial volume. Nevertheless, being highly glycolytic has several advantages for ECs. The production of ROS as a leakage of oxidative phosphorylation is kept at a minimum and ECs are pre-conditioned for hypoxic environments [81,95–97].

The glycolytic flux stimulated by VEGF elevates the expression of the glucose transporter 1 (GLUT1) and glycolytic enzymes such as lactate dehydrogenase-A (LDH-A) and 6-phosphofructo-2-kinase/fructose-2,6-bisphosphatase-3 (PFKFB3). PFKFB3, a key regulator of glycolysis, is well studied in ECs. Genetic silencing reduces glycolytic flux and impairs *in vitro* ECs sprouting as well as *in vivo* outgrowth and branching [83,98]. Additionally, PFKFB3-silenced HUVECs experience problems in vessel sprouting due to loss of tip cell formation [83]. Computational modeling predicted that glycolytic ATP drives ECs rearrangements and that PFKFB3 inhibition normalizes distorted ECs rearrangements in the sprout due elevated VEGF stimulation [99]. Shear stress on quiescent endothelium by blood flow leads to the induction of flow-responsive transcription factor Krüppel-like factor 2 (KLF2) which suppresses PFKFB3 expression by binding to a KLF2-binding site within the PFKFB3 promoter [100]. This results in a reduced glycolysis rate and decreased glucose uptake as well as reduced mitochondrial density. This ensures a metabolically quiescent state in the mature endothelium [81].

1.2.3 Glutamine metabolism of endothelial cells

Glutamine is the most abundant amino acid in the human body occurring in relatively high concentrations (plasma: 500 – 800 µM/L [101]; HUVECs: 8 nmol/10,000 cells/h (consumption) [92]) [102]. Glutamine is converted to its deamidated derivative glutamate by glutaminases (GLS1, GLS2). Subsequently, glutamate is converted to α-ketoglutarate by glutamate dehydrogenase (GLUD1) or by transamination with a suitable α-keto acid substrate. This α-ketoglutarate then enters the TCA cycle as a source of carbons (**Fig. 5**) [82,103].

Mammals express two different GLS isozymes, a kidney-type GLS1 and liver-type GLS2 that serve different functions. GLS1, the predominant isozyme in HUVECs, feeds the TCA cycle with anaplerotic glutamine-derived carbons. GLS2 converts glutamine to glutamate and ammonia in the periportal hepatocytes. This ammonia is then used for urea synthesis and is thus crucial in linking amino acid metabolism to urea synthesis. Interestingly, GLS2 is a rare example of an enzyme that is feed forward stimulated by its product. As a secondary feature, GLS2 shunts carbons and nitrogen into glutathione required for redox homeostasis [82,91,104]. In cancer cells, GLS1 expression is controlled by c-MYC while GLS2 expression is driven by p53. Whether a similar functional difference between both enzymes also exists in ECs is still unknown [80,81,105].

The high glycolytic rate of cancer cells is linked to the need for carbons required for the synthesis of biomass [106]. It is accepted that glutamine serves as a source of carbon atoms for biosynthetic pathways [82]. Tracer studies with $^{13}C_5$-L-glutamine revealed that in HUVECs more than 70% of the TCA cycle carbons are derived from glutamine. Pharmacological inhibition or genetic silencing of GLS1 in HUVECs reduces proliferation and angiogenic sprouting. Nevertheless, interfering with glutamine metabolism does not affect ECs migration which instead relies on aerobic glycolysis [91,92].

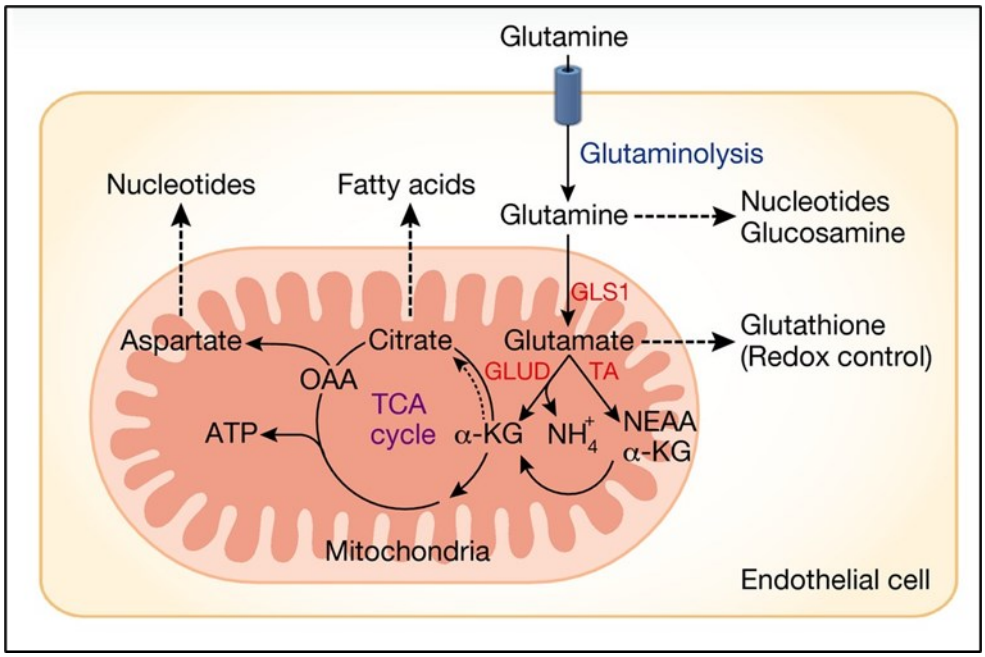

Figure 5. Glutamine metabolism of endothelial cells
Glutamine is deamidated to glutamate by GLS. Glutamate is required for redox-homeostasis. Furthermore, glutamate can be converted into α-ketoglutarate by glutamate dehydrogenase (GLUD1) or glutamate transaminases. α-KG, α-ketoglutarate; TA, transamination; NEAA, non-essential amino acids; OAA, oxaloacetate (figure from Andrade and Potente 2017 [93]).

Apart from being a source of carbon atoms, glutamine is a source of nitrogen. Its γ-nitrogen is incorporated into both the purine and the pyrimidine ring structures making glutamine essential for nucleotide synthesis. Adenine and guanine receive their nitrogen on position 3 and 9 from glutamine. The rate-limiting step in purine synthesis (the transfer of NH_3 released from glutamine into 5-phosphoribosyl-1-pyrophosphate (PRPP) to form 5-phosphoribosyl-1-amine (PRA)) is catalyzed by glutamine phosphoribosylpyrophosphate amidotransferase. The amino group on position 9 will form the N-glycosidic bond of the nucleotide. The nitrogen at position 3 is introduced by 5′-phospho-ribosylformylglycinamidine synthetase. Additionally, the cytosolic carbamoyl phosphate synthetase II introduces the amide nitrogen of glutamine at position 3 of uracil, cytosine, and thymine [80–82].

Furthermore, ECs express considerable amounts of glutamine synthetase (GLUL) but the enzyme has negligible synthesizing capacity. This is indeed very interesting, because if glutamine is used as an energy source why do the cells have so much GLUL if glutamine levels are not rate limiting? Research has shown a role of GLUL beyond that of glutamine synthesis [107]. Knockdown of the enzyme reduces membrane

localization and activation of the GTPase Ras homolog family member J (RHOJ) while activating other Rho GTPases and Rho kinases in HUVECs. These enzymes regulate the dynamic assembly of the cytoskeleton. Therefore, loss of the GLUL enzyme induces actin stress fibers and inhibits endothelial cell motility [107].

Nevertheless, glutamine metabolism in ECs has not been studied intensively although glutaminolysis is very high as compared to other cell types such as lymphocytes [108]. Understanding ECs glutamine metabolism is important considering the similarities between ECs and cancer cells and the importance of glutamine metabolism in cancer progression [109].

1.3 The Glutaminase II pathway

Mammals possess two metabolic pathways to metabolize glutamine to α-ketoglutarate. The most widely studied pathway, also known as the glutaminase I pathway, is the hydrolysis of glutamine to glutamate by glutaminases (GLS1, GLS2) followed by the conversion of glutamate to α-ketoglutarate. However, a second pathway, namely the glutaminase II pathway, is widespread in nature but rarely studied (**Fig. 6**). Within this pathway, glutamine is transaminated with various α-keto acids to α-ketoglutaramate (KGM) and the corresponding L-amino acid. Subsequently, the ω-amidase/NIT2 (nitrilase family member 2) hydrolyzes KGM to α-ketoglutarate and ammonia [103,110,111]. There is evidence that KGM cyclizes at neutral pH values to its lactam form (2-hydroxy-5-oxoproline) being the pre-dominant form (~99.7%) while only 0.3% occur as the open-chain form (the actual substrate of NIT2) [112,113]. Although, transamination reactions are often highly reversible, the glutaminase II pathway is considered to be largely irreversible as the chemical equilibrium of KGM is driven towards its lactam form. The pathway was discovered in the 1950s by Meister and colleagues [114,115] but has not been studied extensively as the major intermediate of the pathway, KGM, is currently not available commercially [103,111]. However, it can be made enzymatically [114,116,117]. Recently (2020) an organic synthesis procedure has been published [118].

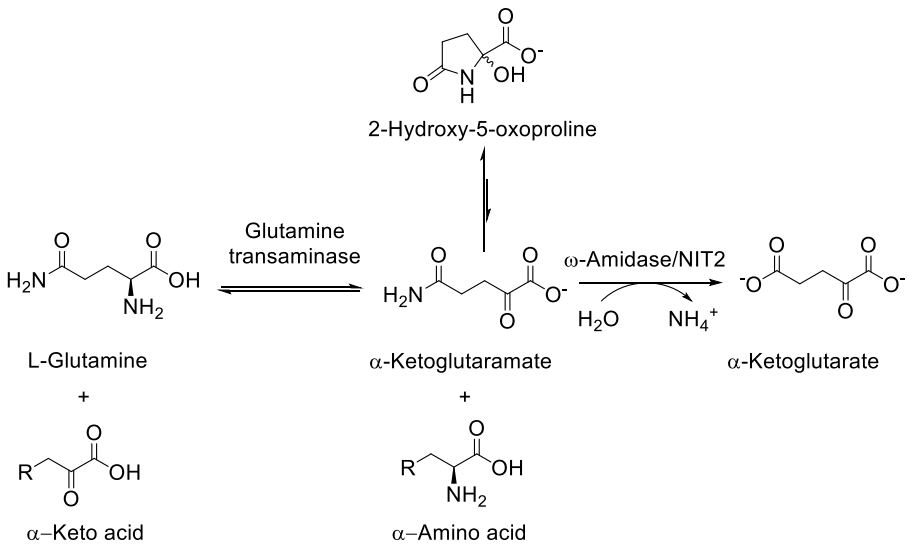

Figure 6. The glutaminase II pathway
L-Glutamine is transaminated with a suitable α-keto acceptor to form α-ketoglutaramate (KGM) and the corresponding α-amino acid. KGM can cyclize to a lactam form (2-hydroxy-5-oxoproline) at neutral pH values. The linear form of KGM is hydrolyzed to α-ketoglutarate and ammonia by the ω-amidase/NIT2. The conversion of KGM to α-ketoglutarate is irreversible (figure adapted from Cooper *et al.* 2016 [111]).

1.3.1 Transamination of glutamine

Two glutamine transaminases, glutamine transaminase K (GTK, kidney isozyme) and glutamine transaminase L (GTL, liver isozyme), are expressed in mammals. Genomic sequencing studies revealed that GTK is identical to kynurenine aminotransferase I (KATI/KYATI/CCBL1) while GTL is equivalent to kynurenine aminotransferase III (KAT3/KYAT3/CCBL2) [119–121]. Both enzymes catalyze the transamination between kynurenine and α-keto acid acceptor. Interestingly, GTK and GTL have broad amino acid and α-keto acid specificities showing highest catalytic efficiency (V_{max}/K_M) with L-glutamine (GTK: 157 $min^{-1}.mM^{-1}$; GTL: 194 $min^{-1}.mM^{-1}$) [110,122–125]. Transamination of kynurenine is an important process in the catabolism of tryptophan but physiological kynurenine concentrations range from <0.05 µM to 2 µM while glutamine concentrations in mammalian tissues range from 1.5 – 5 mM [110]. Considering this, it is likely that glutamine is the preferred (but not the only) amino acid substrate for both enzymes *in vivo* and far more important quantitatively than transamination of kynurenine [103,110].

Both glutamine transaminase isozymes belong to the pyridoxal-5´-phosphate (PLP)-dependent enzyme family. They share the highest sequence similarity and similar active site pockets among all four KYAT enzymes [126]. For GTK, cytosolic and a mitochondrial isoform have been reported due to the presence of two different mRNAs coding for a protein with and without a mitochondrial targeting sequence [124]. GTL carries an N-terminal mitochondrial target sequence and is predicted to be localized in the mitochondria [127,128].

1.3.2 The ω-Amidase/NIT2

The enzyme ω-amidase was discovered in the 1950s by Meister and his colleagues [114,115]. In humans, the NIT2 gene was shown to be identical to ω-amidase [116,129]. The enzyme belongs to the family of hydrolases and was named ω-amidase, because it catalyzes the hydrolysis of various terminal monoamides of 4- and 5-C dicarboxylic acids generating a dicarboxylate and ammonia [103,112,114,115]. In addition to KGM, α-ketosuccinamate (KSM), the corresponding α-keto acid to asparagine, is a known substrate of ω-amidase/NIT2 [110,130].

ω-Amidase has a molecular mass of 30.6 kDa and consists of two independent monomers. Each monomer occurs in an asymmetrical four layered α/β/β/α conformation containing a carbon-nitrogen fold. The enzyme contains a conserved catalytic triad in the active center, which includes a nucleophilic cysteine (C153), a glutamate (E43) and a lysine (K112). Additionally, another glutamate (E128) assists in substrate positioning and explains why the enzyme has no activity with asparagine or glutamine [131–134]. From a mechanistic point of view, the substrate first binds to the active site, then ammonia is released and a thioester intermediate is formed at the cysteine. Subsequently, water binds and the carboxylic acid product is set free (**Fig. 7**) [134]. ω-Amidase activity was predominantly detected in the cytosol of rat liver and kidney, while some activity was reported in the mitochondria [103,117]. How ω-amidase is imported into the mitochondria remains unknown.

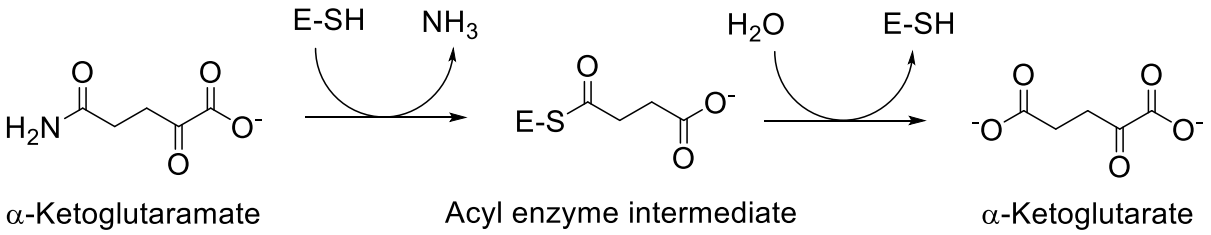

Figure 7. Reaction catalyzed by the ω-amidase/NIT2
KGM as a substrate first binds to the active site of the enzyme, then ammonia is released and a thioester intermediate is formed at the cysteine. Subsequently, water binds and α-ketoglutarate is released (figure adapted from Hersh 1971 [112]).

1.3.3 Linkage of nitrogen and sulfur metabolism

During the synthesis of polyamines, the first carbon of methionine goes off as CO_2 while the carbons 2 – 4 as well as the amine nitrogen are incorporated into polyamines. Additionally, both the sulfur and the methyl group are incorporated into 5´-methylthioadenosine (MTA) [135]. A key element of the glutaminase II pathway is linking sulfur and nitrogen metabolism in mammals by closing the methionine salvage pathway. In this salvage pathway, the original sulfur and methyl moiety are reincorporated into methionine. The carbons 1- 4 come from the ribose portion of MTA. This pathway exists in bacteria, archaea, fungi, animals and plants to prevent loss of sulfur and methyl moieties [103,136,137]. The four carbons of the ribose portion of MTA, and the thiomethyl group of MTA, are incorporated into KMBA (α-keto-γ-methylthiobutyrate, the corresponding α-keto acid of methionine) in mammalian tissues [138–140]. The salvage pathway is closed by transamination of KMBA to methionine with a suitable amino acid (**Fig. 8**). Evidence has been presented that glutamine transaminases and ω-amidase/NIT2 act to close the methionine salvage pathway in bacteria and plants linking nitrogen and sulfur metabolism [103,141].

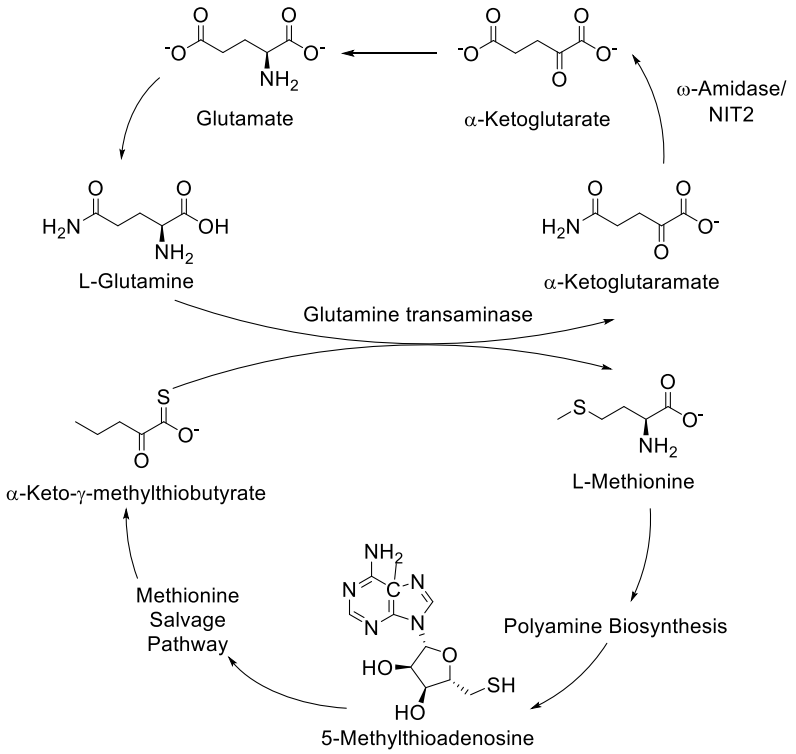

Figure 8. The methionine salvage pathway
Linkage between the methionine salvage pathway and the glutamine transaminase reaction. Glutamine is used as a transaminase substrate to close the methionine salvage pathway (the conversion of α-keto-γ-methiolbutyrate (KMBA) to methionine). For simplicity not all co-substrates and enzymes are shown. (figure adapted from Cooper and Kuhara 2014 [110]).

1.3.4 Metabolic importance of the glutaminase II pathway

Rapidly dividing cells such as cancer cells or ECs rely on glutamine as an energy source. Interestingly, the contribution of the glutaminase II pathway as a source of anaplerotic α-ketoglutarate has not been studied systematically. This is mainly because the pathway is not generally well known to the scientific community and the major intermediate KGM is not commercially available, and until recently could only be made by an enzymatic procedure [112,142]. However, KGM has recently been made by an organic synthesis procedure [103,118]. Therefore, only few studies of the glutaminase II pathway in cells have been published.

Recent tracer experiments showed that the glutaminase II pathway contributes to glutamate production in pancreatic cancer after pharmacological inhibition of GLS1 [143]. Meister showed that rat liver hepatoma cells have considerable ω-amidase activity [115]. Others have shown glutamine transaminase activity in brain tissues and in a dedifferentiated human astrocytoma [103] as well as immunohistochemical staining for ω-amidase and GTK in normal human pancreatic, bladder and prostate cells [144]. A cell atlas that combines transcriptomic, proteomic, immunofluorescence and mass spectrometry data maps the *in situ* localization of 12,003 proteins at the single cell level has been published. The authors of this atlas found that the NIT2 gene is expressed in nearly all cell lines examined [145].

Contradictory results were shown with respect to cancer. Overexpression of NIT2 in HeLa cells was found to inhibit cell growth through arrest in the G(2) phase of the cell cycle [146] while NIT2 overexpression was linked to the high proliferation rate of tongue squamous cell carcinomas [147].

No study has been conducted to the molecular importance of NIT2 and the glutaminase II pathway in ECs.

2. Aim of this study

ROS are important mediators of both physiological and pathophysiological signal transduction in the cardiovascular system. The effect of ROS on cellular processes depend on the concentration, localization and duration of exposure, while the cellular stress response mechanisms to this are essential to mitigate the negative effects of acute oxidative stress. However, the metabolic and transcriptomic response of ECs to different types and concentrations of ROS is not fully understood. As ROS production is transient, appropriate tools to study the complex cellular response to intracellular oxidants, particularly over the course of time, have been lacking. Many assumptions on the biological role of H_2O_2 in signaling events have been made by adding extracellular H_2O_2 to cultured cells. However, this does not reflect the dynamics of intracellular H_2O_2 flux in the regulation of signaling events.

To compare the metabolic and transcriptomic effects of intracellularly generated H_2O_2 to other types of ROS, we utilized a chemogenetic approach based on overexpression of human D-amino acid oxidase (DAO). DAO oxidizes D-amino acids to their corresponding imino acids and H_2O_2. The imine is then non-enzymatically hydrolyzed to its corresponding α-keto acid [148,149]. The enzyme is stereospecific for D-amino acids (e.g. D-alanine) and exposure to D-amino acids allows turnover with production of intracellular H_2O_2. This makes DAO a useful tool to study how intracellular production of H_2O_2 modules cellular response.

With this tool in hand, we will analyze the different metabolic and transcriptomic responses of HUVECs to DAO-derived H_2O_2 in comparison to exposure to exogenous H_2O_2 or menadione (to generate intracellular $O_2^{\bullet-}$) in a time dependent manner. Furthermore, we aim to identify novel redox sensitive metabolic pathways in ECs.

3. Materials and methods

3.1 Materials

3.1.1 Chemicals

Table 1. List of chemicals

Chemical	Vendor/Supplier
[$^{13}C_1$]-D-Glucose	Sigma-Aldrich, Taufkirchen, Germany
[$^{13}C_1$]-Pyruvate	Sigma-Aldrich, Taufkirchen, Germany
[$^{13}C_1$]-α-Ketoglutaric acid	Sigma-Aldrich, Taufkirchen, Germany
[$^{13}C_2$]-Citric acid	Sigma-Aldrich, Taufkirchen. Germany
[$^{13}C_2$]-L-Glutamic acid	Sigma-Aldrich, Taufkirchen, Germany
[$^{13}C_2$]-Succinic acid	Sigma-Aldrich, Taufkirchen, Germany
[$^{13}C_5$]-Itaconic acid	Toronto Research Chemicals, Toronto, Canada
[$^{13}C_5$-$^{15}N_2$]-L-Glutamine	Cambridge Isotopes Laboratories Inc., Tewksbury, USA
[6-^{13}C]-Glucose-6-phosphate	Sigma-Aldrich, Taufkirchen, Germany
2-Acrylamido-2-methylpropane sulfonic acid (AMPS)	AppliChem, Darmstadt, Germany
3-[(3-Cholamidopropyl)dimethylammonio]-1-propanesulfonate hydrate (CHAPS)	Roche, Bremen, Germany
4-(2-Hydroxyethyl)-1-piperazineethanesulfonic acid (HEPES)	Roth, Karlsruhe, Germany
4',6-Diamidino-2-phenylindole (DAPI)	Sigma-Aldrich, Taufkirchen, Germany
4H-Furo[3,2-b]pyrrole-5-carboxylic acid	Sigma-Aldrich, Taufkirchen, Germany
5x EvaGreen QPCR Mix II (ROX)	Bio&Sell, Feucht, Germany
Acrylamide	Serva, Heidelberg, Germany
Agar	AppliChem, Darmstadt, Germany
Agarose	Bio&Sell, Feucht, Germany
D-Alanine	Roth, Karlsruhe, Germany
L-Alanine	Roth, Karlsruhe, Germany
Ammoniumbicarbonate (ABC)	Thermo Fisher Scientific, Dreieich, Germany
Ampicillin sodium salt	Sigma-Aldrich, Taufkirchen, Germany
Bis-2-(5-phenylacetamido-1,3,4-thiadiazol-2-yl)ethyl sulfide (BPTES)	Sigma-Aldrich, Taufkirchen, Germany
Bromophenol blue	AppliChem, Darmstadt, Germany
Casyton	Roche, Bremen, Germany
Citric acid	Roth, Karlsruhe, Germany

Coomassie® Brilliant Blue G 250	Serva, Heidelberg, Germany
Deoxyribose nucleotides (dNTPs)	Bioline, London, United Kingdom
Dextran	Roth, Karlsruhe, Germany
Dextrose	Roth, Karlsruhe, Germany
Dimethyl sulfoxide (DMSO)	Sigma-Aldrich, Taufkirchen, Germany
Dithiothreitol (DTT)	Invitrogen, Burlington, Canada
DNase I, RNase free	Promega, Mannheim, Germany
Dulbecco`s Phosphate Buffered Saline (DPBS)	Gibco Life Technologies, Carlsbad, USA
Dynabeads™ MyOne™ Streptavidin C1	Thermo Fisher Scientific, Dreieich, Germany
Ethidium bromide	Roth, Karlsruhe, Germany
Ethylene glycol tetraacetic acid (EGTA)	AppliChem, Darmstadt, Germany
Ethylenediaminetetraacetic acid (EDTA)	AppliChem, Darmstadt, Germany
EtOH absolute	Sigma-Aldrich, Taufkirchen, Germany
EZ-Link™ Iodoacetyl-PEG2-Biotin	Thermo Fisher Scientific, Dreieich, Germany
Fetal calf serum (FCS)	Thermo Fisher Scientific, Dreieich, Germany
Gelatin	Sigma-Aldrich, Taufkirchen, Germany
Gentamycin	Roth, Karlsruhe, Germany
L-Glutamine	Gibco Life Technologies, Carlsbad, USA
Hydrogen Peroxide 30% (H_2O_2)	Roth, Karlsruhe, Germany
Hygromycin B	Gibco Life technologies, Carlsbad, USA
Imidazole	Bio-Rad, Munich, Germany
Isopropyl alcohol	Sigma-Aldrich, Taufkirchen, Germany
α-Ketoglutaramate	Travis T. Denton, Spokane, USA
α-Keto-γ-(methylthio)butyric acid sodium salt (KMBA)	Sigma-Aldrich, Taufkirchen, Germany
Lipofectamine™ 2000	Life technologies, Carlsbad, USA
Lipofectamine™ RNAiMAX	Life technologies, Carlsbad, USA
Loading Dye, 6x	Life technologies, Carlsbad, USA
Luminol	Sigma-Aldrich, Taufkirchen, Germany
Menadione	Sigma-Aldrich, Taufkirchen, Germany
Methanol	Sigma-Aldrich, Taufkirchen, Germany
Methanol, Ultra LC/MS grade	Roth, Karlsruhe, Germany
Okadaic acid (OA)	AppliChem, Darmstadt, Germany
Orthovanadate (OV)	AppliChem, Darmstadt, Germany
Penicilin	Thermo Fisher Scientific, Dreieich, Germany
Penicillin/Streptomycin	Corning, Manassas, USA

Peptone from casein (pancreatic digest)	AppliChem, Darmstadt, Germany
Phenylmethanesulfonylfluoride (PMSF)	Sigma-Aldrich, Taufkirchen, Germany
Phorbol 12-myristate 13-acetate (PMA)	EnzoLifeSciences, Lörrach, Germany
Pierce™ Streptavidin Agarose	Thermo Fisher Scientific, Dreieich, Germany
Polyethyleneimine (PEI)	Sigma-Aldrich, Taufkirchen, Germany
Precision Plus Protein Standard Dual Color	Bio-Rad, Munich, Germany
Puromycin dihydrochloride	Thermo Fisher Scientific, Dreieich, Germany
Random Primers	Promega, Madison, USA
Reverse Transcriptase Superscript III	Life Technologies, Carlsbad, USA
ROTI®Block	Roth, Karlsruhe, Germany
ROTI®GelStain	Roth, Karlsruhe, Germany
ROTI®Histofix 10%	Roth, Karlsruhe, Germany
ROTI®Quant	Roth, Karlsruhe, Germany
ROTIPHORESE® Gel 30 (37,5:1)	Roth, Karlsruhe, Germany
Sodium chloride	Sigma-Aldrich, Taufkirchen, Germany
Sodium citrate	Sigma-Aldrich, Taufkirchen, Germany
Sodium dodecyl sulfate (SDS)	Roth, Karlsruhe, Germany
Streptavidin Agarose Resin	Thermo Fisher Sceintific, Dreieich, Germany
Succinamic acid	Sigma-Aldrich, Taufkirchen, Germany
SYPRO Orange Protein Gel Stain	Thermo Fisher Scientific, Dreieich, Germany
Tetramethylethylenediamine (TEMED)	AppliChem, Dreieich, Germany
Tris(hydroxymethyl)aminomethane (TRIS)	Roth, Karlsruhe, Germany
Triton X-100	Roth, Karlsruhe, Germany
Trypsin-EDTA	Sigma-Aldrich, Taufkirchen, Germany
Tween-20	Sigma-Aldrich, Taufkirchen, Germany
VEGF(165), recombinant human	R&D, Minneapolis, USA
Zymosan	Sigma-Aldrich, Taufkirchen, Germany

3.1.2 Equipment

Table 2. List of equipment

Equipment	Product descriptor	Vendor
Autoclave	3150 ELV	Tuttnauer, Beit Shemesh, Israel
Cell Counter	Casy	Schärfe System, Reutlingen, Germany
Centrifuge	5415 R (F45-24-11)	Eppendorf, Hamburg, Germany
	Micro Star 17R (75003424)	VWR, Dreieich, Germany
	Heraeus Megafuge 16 (75003629)	Thermo Fisher Scientific, Dreiech, Germany
	Sorvall RC 6+ (F13-14x50cy or F10-6x500y)	Thermo Fisher Scientific, Dreieich, Germany
	Concentrator plus	Eppendorf, Hamburg, Germany
Chromatography	Äkta FPLC	GE Healthcare, Solingen, Germany
	Dionex Ultimate 3000	Thermo Fisher Scientific, Dreieich, Germany
	Nanospray Flex Ion-Source	Thermo Fisher Scientific, Dreieich, Germany
Columns	HisTrap™ FF crude	GE Healthcare, Solingen, Germany
	C18 reversed-phase precolumn	Thermo Fisher Scientific Scientific, Dreieich, Germany
	Reprosil C18 resin	Dr. Maisch GmbH, Ammerbuch, Germany
	C18 column	Waters, Milford, USA
	Luna Omega 1.6 µm PS C18	Phenomenex, Aschaffenburg, Germany
	UHPLC Fully Porous C18	Phenomenex, Aschaffenburg, Germany
Cycler	iCycler Detection System (MyiQTM)	BioRad, Munich, Germany
	iCycler iQ™ Single-Color Real Time PCR	BioRad, Munich, Germany
Freezer	HERAfreeze basic (-80°C)	Heraeus Instruments, Hanau, Germany
Gel documentation system	Intas Gel-Stick Imager	Royal Biotech, Frankfurt am Main, Germany
Heating block	Thermomixer compact	Eppendorf, Hamburg, Germany
Incubator	Hera Cell 150i CO_2 Incubator	Thermo Fisher Scientific, Dreieich, Germany
	IL 23	VWR, Dreieich, Germany
Infrared scanner	Odyssey	LI-COR Biosciences, Bad Homburg, Germany
LC system	Agilent 1290 Infinity LC system	Agilent, Waldbronn, Germany

Luminometer	Berthold 6-channel device LB9505	Berthold, Wildbad, Germany
Magnetic stirrers	Heidolph MR Hei-Mix L	NeoLab, Heidelberg, Germany
Mass analyzer	Orbitrap	Thermo Fisher Scientific, Dreieich, Germany
Mass spectrometer	QTrap 5500	Sciex, Dreieich, Germany
	QExactive Plus	Thermo Fisher Scientific, Dreieich, Germany
Microscope	Evos XL Core	Thermo Fisher Scientific, Dreieich, Germany
	LSM800	Zeiss, Göttingen, Germany
Microwave	900&Grill	Severin, Sundern, Germany
PCR device	Eppendorf Mastercycler Gradient	Eppendorf, Hamburg, Germany
pH meter	PP-50	Sartorius, Göttingen, Germany
Pipette	1 µL - 10 µL	Eppendorf, Hamburg, Germany
	0.1 – 2.5 µL	
	2 - 20 µL	
	20 - 200 µL	
	100 - 1000 µL	
Power supply	CS – 300V	Roth, Karlsruhe, Germany
qPCR device	AriaMx Real-Time PCR	Agilent Technologies, California, USA
Rotor	Stuart SB3	Stuart, Staffordshire, United Kingdom
Scale	Analytical Balance	Sartorius, Göttingen, Germany
	MC1	Sartorius, Göttingen , Germany
Shaker	GFL-3013	Thermo Fisher Scientific, Dreieich, Germany
	MaxQ 4000 Benchtop Orbital	Thermo Fisher Scientific, Dreieich, Germany
Spectrophotometer	NanoDrop® ND-1000	Nanodrop Technologies, Rockland, USA
Sterile bench	Laminarflow HB 2448	Heraeus Instruments, Hanau, Germany
	Herasafe HS 12	Heraeus Instruments, Hanau, Germany
	SCI-tive Hypoxia Work Station	Baker Russkin, Sanford, USA
Vortex mixer	Vortex Genie 2	Scientific Industries, New York, USA
Water purification system	Milli-Q Q-POD	Millipore, Billerica, USA
Western Blot	Chamber	BioRad, Munich, Germany

3.1.3 Materials

Table 3. List of materials

Material	Vendor
AriaMx Low Profile Strip Tubes	Agilent Technologies, United Kingdom
BioFlex Culture Plate, untreated	Flexcell® International Corp., Burlington, USA
Cell culture dish, with vents, 100 x 20 mm, sterile	Greiner Bio-One, Frickenhausen, Germany
Dishes TC Easy-Grip 35 x10 mm,sterile	BD Biosciences, Heidelberg, Germany
Dishes TC Easy-Grip 60 x15 mm,sterile	BD Biosciences, Heidelberg, Germany
Dishes 6 well, with lid, sterile	Greiner Bio-One, Frickenhausen, Germany
Dishes 8 well, with lid, for IF	Ibidi, Gräfeling, Germany
Test and centrifugal tubes (15 mL, 50 mL)	Sarstedt, Nümbrecht, Germany
Nitrocellulose transfer membrane	NeoLab, Heidelberg, Germany
Whatman paper/ gel-blotting paper	A. Hartenstein, Würzburg, Germany

3.1.4 Buffers and solutions

Table 4. List of buffers and solutions

Buffer	Recipe
ACD buffer	7.36 g Citric acid, 14.71 g sodium citrate, 9.91 g dextrose to 250 mL ddH_2O
Alkylation buffer	40 mM HEPES; 50 mM NaCl; 1 mM EGTA; inhibitors; 100 mM NEM, pH 7.4; 2 mM sodium orthovanadate (OV); 10 nM okadaic acid (OA); protein inhibitor mix (PIM) containing antipain, aprotinin, chymostatin, leupeptin, pepstatin and trypsin-Inhibitor (10 nM each); 40 µg/mL phenylmethylsulfonyl fluoride (PMSF)
BIAM-resolution buffer	20 mg/mL BIAM (EZ-Link™ Iodoacetyl-PEG2-Biotin); 50 mM Tris-HCl, pH 8.5; 8 M Urea; 5 mM EDTA; 1% SDS
BIAM-resolving buffer	50 mM Tris-HCl, pH 8,5; 5 mM EDTA; 20% SDS; 10% Triton
Dextran (6%)	15 g Dextran, 2.25 g NaCl to 250 mL ddH_2O
DNA loading dye (6x)	10 mM Tris-HCl (pH 7.6) 30% v/v glycerol; 0.25% w/v bromophenol blue; 0.25% w/v xylene cyanol; to 10 mL ddH_2O
Hank's solution	Hank´s balanced salts (HBSS) 1.75 g sodium bicarbonate to 5 L ddH_2O
HEPES-Tyrode (HT) buffer	119 mM NaCl, 5 mM KCl, 25 mM HEPES, 2 mM $CaCl_2$, 2 mM $MgCl_2$, 6 g/L glucose, pH 7.4
Laemmli buffer (3x)	125.3 mM Tris/-HCl pH 6.8; 17% glycerol; 4% SDS; 40 mM DTT; 0.004% bromophenol blue
Methocel	6 g Methocel (autoclave powder); add 250 mL endothelial basal medium (EBM) and mix at 60°C for 20 min; add 250 mL EBM and mix overnight 4°C; centrifuge 4000 rpm, 4°C and for 2 h
NEM-resolution buffer	50 mM NEM; 50 mM Tris-HCl, pH 8,5; 8 M urea; 5 mM EDTA; 20% SDS

Running buffer (10x)	25 mM Tris; 190 mM glycine; 0.1% SDS
Sample buffer	8.5% Glycerol, 2% SDS, 6.25% Tris/HCl, pH 6.8, 20 mM DTT, 0.013% bromophenol blue, for non-reducing sample buffer no DTT was added
TAE (50x)	242 g Tris; 57.1 mL glacial acetic acid; 10 mL EDTA (0.5 M); pH to 8.0; to 1 L ddH_2O
Transfer buffer (10x)	25 mM Tris; 190 mM glycine; 20% methanol
Triton lysis buffer	20 mM Tris/HCl pH 7,5; 150 mM NaCl; 10 mM sodium diphosphate decahydrate (NaPPi); 20 mM sodium fluoride (NaF); 1% Triton X-100; 2 mM sodium orthovanadate; 10 nM okadaic acid; protein inhibitor mix containing antipain, aprotinin, chymostatin, leupeptin, pepstatin and trypsin-Inhibitor (10 nM each); 40 µg/mL phenylmethylsulfonyl fluoride
Wash buffer (10x)	0.3% Tween-20; 50 mM Tris/-HCl pH 7.5; 150 mM NaCl

3.1.5 Bacterial growth medium

Table 5. Bacterial growth medium

Medium	Recipe
2-YT medium	Tryptone (16 g/L), yeast extract (10 g/L), NaCl (5 g/L)

3.1.6 Cell culture media

Table 6. List of cell culture media

Medium	Recipe
Endothelial Cell Growth Medium (Pelo Biotech, Planegg)	Human recombinant epidermal growth factor (EGF), EndoCGS-Heparin, 8% FCS, 10 mM L-glutamine, 50 U/mL penicillin, 50 µg/ mL streptomycin
Endothelial Basal Medium (Pelo Biotech, Planegg)	0.1% FCS, 10 mM L-glutamine
HEK293/ Lenti-X Cell Medium	DMEM GlutaMAXX™ (Gibco), 8% FCS, 50 U/mL penicillin 50 µg/mL streptomycin
Trypsin (Thermo Fisher Scientific)	10X

3.1.7 Human eukaryotic cells

Table 7. List of eukaryotic cells

Cell type	Cell type	Manufacturer
Human embryonic kidney (HEK) 293 cells	Cell line	ATCC, Manassas, USA
Human umbilical vein endothelial cells (HUVECs)	Primary cells	Lonza (CC-2519, Lot No.186864; 191772; 192485; 76524; 76921, 7F3111) Walkersville, USA
Lenti-X™ 293T cells	Cell line	Takara, Tokyo, Japan

3.1 8 Competent cells

Table 8. List of competent cells

Strain	Vendor
5-Alpha Competent *E. Coli*	New England Biolabs, Frankfurt am Main, Germany
NEB Stable Compentent *E. Coli*	New England Biolabs, Frankfurt am Main, Germany
XL10-Gold Ultracompetent Cells	Stratagene, Bellingham, USA

3.1.9 Synthetic oligonucleotides

Table 9. List of synthetic oligonucleotides including overhangs

Gene	Forward Primer (5´-3´)	Reverse Primer (5´-3´)
GLS1_gRNA	CACCGCATCATACCCATAACATTG	AAACCAATGTTATGGGTATGATGC
KYAT1_gRNA	CACCGACACCCCCAACAACCCCCT	AAACAGGGGGTTGTTGGGGGTGTC
KYAT3_gRNA	CACCGGCCTGAATCAGTATACACG	AAACCGTGTATACTGATTCAGGCC
NIT2	AGCCCATTGGGAGTTACTTC	CTTCTTCTGTGCCAGCTTTG
NIT2_BioID	ACACCTTCGAAATGACCTCTTTCCGCTTGGC	ACACCGCGGCCGCTTAGTGATGGTGGTGATGAT
NIT2_gRNA	CACCGGCAGCATATATCTCATTGG	AAACCCAATGAGATATATGCTGCC
NIT2C146A	ACTCCTTACGCCAGAGTGGGT	ATCAAATGTGGAGAAACTATCAC
NIT2C146S	TACTCCTTACAGCAGAGTGGGTC	TCAAATGTGGAGAAACTATC
NIT2C153S	TCTGGGCATCTCCTACGACATGC	CCCACTCTGCAGTAAGGAG
NIT2C44S	TTTGCCGGAATCCTTTAATTCTC	GAAACTATTTTGGCTCCTTG
NIT2C76S	AGCAAAGGAATCCTCCATCTACTTG	ACTTCAGAAAGCTTCTGTG
NIT2C97S	ATATAACACCTCCGCTGTGTTTGG	AATTTCCCAGCATCCTCTTC
NTC1	CACCGTTCCGGGCTAACAAGTCCT	AAACAGGACTTGTTAGCCCGGAAC
pLVX_DAO His Tag	ACACCTTCGAAATGCGTGTGGTGGTG	ACACCGCGGCCGCTTAGTGATGGTGGTG

3.1.10 Plasmids

Table 10. List of plasmids

Plasmid	Manufacturer/Supplier
CAG yDAO-HyPer7-NES	Eurofins Genomics LLC, Louisville, Kentucky, USA
Cre-recombinase	#62730 Addgene, Watertown, USA
LentiCRISPR v2	Frank Schnütgen, Goethe-University, Frankfurt, Germany
pBS513 EF1alpha-cre	#11918 Addgene, Watertown, USA
pcDNA3.1	Christoph Schürmann, Goethe-University, Frankfurt, Germany
pCMV6 DAO-10X His Tag	Sino Biological (HG13371-CH), Wayne, USA
pCMV6-NIT2-10X His Tag	Sino Biological (HG23517-CH), Wayne, USA
pLVX CAAX CIBN	Xavier Trepat [150], Institute for Bioengineering of Catalonia, Barcelona, Spain
pLVX-BioID2 PuroRes	Tim Schader, Goethe-University, Frankfurt, Germany
pLVX-DAO-10X His Tag PuroRes	Niklas Müller, Goethe-University, Frankfurt, Germany
pLVX-NIT2-BioID2 PuroRes	Niklas Müller, Goethe-University, Frankfurt, Germany
psPAX2	#12260 Addgene, Watertown, USA
VSV-G	#12259 Addgene, Watertown, USA

3.1.11 Cloning enzymes

Table 11. List of cloning enzymes

Name	Manufacturer
FastDigest AfeI	Thermo Fisher Scientific, Dreieich, Germany
FastDigest BamHI	Thermo Fisher Scientific, Dreieich, Germany
FastDigest Bsp119I	Thermo Fisher Scientific, Dreieich, Germany
FastDigest Buffer Green 10X	Thermo Fisher Scientific, Dreieich, Germany
FastDigest EcoRI	Thermo Fisher Scientific, Dreieich, Germany
FastDigest Esp3I/BsmBI	Thermo Fisher Scientific, Dreieich, Germany
FastDigest NheI	Thermo Fisher Scientific, Dreieich, Germany
FastDigest NotI	Thermo Fisher Scientific, Dreieich, Germany
Phusion™ High Fidelity DNA Polymerase	Thermo Fisher Scientific, Dreieich, Germany
T4 DNA Ligase	Thermo Fisher Scientific, Dreieich, Germany

3.1.12 Antibodies

Table 12. List of antibodies

Name	Host	Manufacturer	ID
6x-His tag	Rabbit	Bethyl Laboratories, Montgomery, USA	A190-114A
β-Actin	Mouse	Sigma-Aldrich, Taufkirchen, Germany	A1978
BioID	Mouse	Abcam, Cambridge, UK	ab232733
D-Amino acid oxidase	Rabbit	Abcam, Cambridge, UK	ab140127
Dihydrolipoamide S-succinyltransferase	Mouse	Abcam, Cambridge, UK	ab110306
Dihydrolipoamide S-succinyltransferase	Rabbit	Sigma-Aldrich, Taufkirchen, Germany	HPA003010
Glutamate dehydrogenase	Rabbit	Sigma-Aldrich, Taufkirchen, Germany	HPA061369
Glutamate dehydrogenase	Mouse	R&D systems, Minneapolis, USA	MAB8027
Glutaminase 1	Rabbit	Abcam, Cambridge, UK	ab156876
Glutamine transaminase K/ kynurenine aminotransferase 1	Rabbit	Sigma-Aldrich, Taufkirchen, Germany	HPA021176
Glutamine transaminase L/ kynurenine aminotransferase 3	Rabbit	Sigma-Aldrich, Taufkirchen, Germany	HPA026538
Heat shock protein family E	Goat	R&D systems, Minneapolis, USA	AF3298
Heat shock protein family E	Rabbit	Sigma-Aldrich, Taufkirchen, Germany	HPA038755
IRDye680 anti-chicken/goat/mouse/rabbit	Donkey	LI-COR Biosciences, Bad Homburg, Germany	926-680x
IRDye800 anti-chicken/goat/mouse/rabbit	Donkey	LI-COR Biosciences, Bad Homburg	926-800x
Nitrilase family member 2	Rabbit	Abcam, Cambridge, UK	ab183074
Peroxiredoxin 1	Mouse	R&D systems, Minneapolis, USA	MAB3488
Peroxiredoxin 2	Goat	R&D systems, Minneapolis, USA	AF3489
Peroxiredoxin 3	Rabbit	Bethyl Laboratories, Montgomery, USA	A304-744
Peroxiredoxin-4	Goat	R&D systems, Minneapolis, USA	AF5460
Peroxiredoxin-SO_3	Rabbit	Abcam, Cambridge, UK	ab16830

3.1.13 Kits

Table 13. List of kits

Kit	Manufacturer
Duolink® Proximity Ligation Assay Kit	Sigma-Aldrich, Cambridge, UK
Ezfaast Amino Acid Analysis Kit	Phenomenex, Aschaffenburg, Germany
GeneJET Plasmid Miniprep Kit	Thermo Fisher Scientific, Dreieich, Germany
Mitochondria/Cytosol Fractionation Kit	Abcam, Cambridge, UK
peqGOLD XChange Plasmid Maxi-EF Kit	Peqlab, Erlangen, Germany
Q5® Site-Directed Mutagenesis	New England Biolabs, Frankfurt, Germany
QIAquick Gel Extraction Kit	Qiagen, Hilden, Germany
QIAquick PCR Purification Kit	Qiagen, Hilden, Germany
RNA Mini Kit	Bio&SELL, Feucht bei Nürnberg, Germany
RNA Mini spin column	Qiagen, Hilden, Germany

3.1.14 Software

Table 14. List of software

Software	Manufacturer
AxioVision SE64 Rel. 4.9	Zeiss, Oberkochen, Germany
Citavi 6	Swiss Academic Software, Wädenwil, Switzerland
Clone Manager 9	Scientific and Educational Software, Cary, USA
Cytoscape	Cytoscape Consortium; Seattle, USA
GraphPadPrism 9.2.0	GraphPad Software, San Diego, USA
Microsoft Excel 2016	Redmond, USA
Microsoft PowerPoint 2016	Redmond, USA
Microsoft Word 2016	Redmond, USA
Nanodrop, Version 3.5.1	Coleman Tech., Orlando, USA
PEAKS	Bioinformatics Solutions Inc., Waterloo, Canada
R (4.1.1)	https://www.r-project.org
R Studio	RStudio Inc., Boston, USA
Salmon 1.5.2	https://salmon.readthedocs.io/en/latest/
SnapGene (5.3)	GSL Biotech, San Diego, USA
Stavrox X3.4.12	Michael Götze, Halle, Germany
TargetP - 2.0 [151]	DTU Health Tech, Lyngby, Denmark
ZEN Imaging software	Zeiss, Oberkochen, Germany
Zoom Incucyte	Sartorius, Göttingen, Germany

3.1.15 Packages

Table 15. List of packages

Name	Source
ClusterProfiler (4.0.5)	Bioconductor
DEseq2 (1.32.0)	Bioconductor
ggplot2 (3.3.5)	CRAN
stats (4.1.1)	RStudio Inc., Boston, USA

3.1.16 Databases

Table 16. List of databases

Name	Source
Hg38 trancriptome	Ensembl
UniProtKB	https://www.uniprot.org

3.2 Methods

3.2.1 Cell Culture

3.2.1.1 Thawing of eukaryotic cells

Frozen cell aliquots were thawed in a water bath at 37 °C and resuspended in 5 mL fresh growth media. Subsequently, cells were centrifuged for 4 min at 100x*g*. The cell pellet was resuspended in 2 mL media and transferred onto a (pre-coated) cell culture dish.

3.2.1.2 Eukaryotic cell culture

Pooled human umbilical vein endothelial cells (HUVECs) were cultured in a humidified atmosphere of 5% CO_2 at 37 °C on dishes coated with gelatin. HUVECs were grown in enhanced endothelial cell growth medium. HEK293 and Lenti-X cells were grown in DMEM (high glucose, GlutaMAXX™) containing 8% FCS and 0.5% penicillin/streptomycin. HUVECs were used at passages 3 – 5 while HEK293 and Lenti-X cells were used at passages 4 – 40. For each experiment, at least three different batches of HUVECs were used.

3.2.1.3 Passaging and cell counting

Cell culture dishes were pre-coated with gelatin (0.2%) for 30 min at room temperature. Cells were washed twice with 1x DPBS and detached with trypsin-EDTA. After centrifugation for 4 min at 100x*g*, the cell pellet was resuspended in growth medium. A fraction of the cell suspension was added to an isotonic saline solution (Casyton) and counted using the Casy Cell Counter. Subsequently, cells were seeded on pre-coated dishes.

3.2.1.4 Cell stimulation

Experiments requiring stimulation were performed at 90% cell confluence in basal medium without growth factors and supplemented with 0.1% FCS and 10 mM L-glutamine. Control cells were treated with the corresponding solvent or basal medium.

3.2.1.5 Overexpression procedures

HEK293 cells were transfected at 80% density with Lipofectamine2000 according to the manufacturer's instructions. Briefly, for a 3.5 cm dish two separate solutions were prepared (A: 35 µL MEM and 3.5 µL Lipofectamine2000; B: 50 µL MEM and 1.5 µg

plasmid). After 5 min, solution A and B were mixed, incubated for 20 min and added dropwise to the target cells. Media exchange was performed after 6 h. Cells were used 48 h after transfection.

3.2.1.6 Generation of pseudotyped lentivirus

Pseudotyped lentiviruses were produced by transfection using PEI (polyethyleneimine, DNA:PEI ratio 1:5) of LentiX cells with the corresponding lentiviral overexpression plasmid together with lentiviral packaging plasmids psPAX2 and VSV-G as previously described [152]. Viral supernatants were collected, filtrated and snap-frozen on the third day after transfection. Virus aliquots were documented according to the biosafety rules (S2) and maintained at -80 °C until transduction.

3.2.1.7 Lentiviral transduction

Target cells were transduced with viral particles for 24 h using polybrene (8 µg per ml medium) and then selected 48 h post-transduction with puromycin (2 µg/ml) and/or hygromycin (400 µg/ml) for 7-10 days. For antibiotic selection, media exchanges were performed daily. Knockouts or knock-ins were verified by western blot analysis. Transduced cells were aliquoted (~500,000 cells per aliquot) and stored in FCS containing 10% DMSO at -150 °C (long-term) or -80 °C (short-term).

3.2.1.8 Isolation of neutrophil granulocytes

Neutrophil granulocytes were isolated from buffy coats by density gradient separation as previously described [153]. Zymosan was opsonized with fresh human serum (20 mg/ml) by incubation at 37 °C for 30 min. The serum was then removed, the zymosan washed with PBS, and then resuspended in PBS (15 mg/ml). Opsonized zymosan was kept on ice until further use. For the BIAM switch assay, 20.000.000 granulocytes (per plate) were directly added to the HUVECs and subsequently activated with opsonized zymosan (3 mg/ml) for 15 min at 37 °C followed by the BIAM procedure.

3.2.1.9 Immunofluorescence

Cells were seeded on 8-well immunofluorescence plates. The next day, mitochondria were stained using the MitoTracker Deep Red kit according to the manufacturer's instructions. Subsequently, cells were washed with PBS, fixed with 4% paraformaldehyde, quenched with glycine (2%), washed again with PBS and permeabilized with 0.05% Triton X-100. After blocking with 3% BSA for 30 min, the

cells were incubated at 4 °C overnight with a 1:200 dilution of the primary antibody. Cells were washed with 0.3% Tween20 in PBS and incubated with a 1:500 dilution of secondary antibody for 30 min. The cells were then washed again with 0.3% Tween20 and counterstained with DAPI (1:500). Images were captured with a laser confocal microscope LSM800 and analyzed with ZEN lite software.

3.2.1.10 Proximity ligation assay (PLA)

The PLA was performed as described in the manufacturer's protocol (Duolink® Proximity Ligation Assay Kit Orange). HUVECs were fixed in phosphate buffered formaldehyde solution (4%), permeabilized with Triton X-100 (0.2%), blocked with serum albumin solution (3%) in phosphate-buffered saline and incubated overnight with primary antibodies. Samples were washed and incubated with the respective. PLA-probes for 1 h at 37 °C. After washing, samples were ligated for 30 min (37 °C). After an additional washing step, the amplification with polymerase was performed for 100 min (37 °C). The nuclei were stained using DAPI. Images (with Alexa Fluor, 546 nm) were acquired by confocal microscope.

3.2.2 Molecular biology

3.2.2.1 Transformation of competent cells by heat shock

An aliquot of competent cells was thawed on ice. Afterwards, 10 ng of plasmid DNA was added and incubated together on ice for 30 min. Subsequently, a heat shock at 42 °C for 30 s was performed followed by a second incubation on ice for 5 min. Then, 950 µL of bacterial growth media was added and the cells were incubated at 37 °C for one hour at 500 rpm. Cells were plated out on a pre-warmed LB-agar plate supplemented with the appropriate antibiotics for selection. The plate was incubated over night at 37 °C.

3.2.2.2 Preparation of plasmid DNA

A single bacterial colony was inoculated into LB-medium (5 mL for MiniPrep/ 200 mL for MaxiPrep) supplemented with the corresponding antibiotic, grown at 37 °C at 250 rpm overnight and harvested the next morning by centrifugation (2,400x*g* for 10 min, 4°C). The plasmid DNA was purified using the GeneJET Plasmid Miniprep Kit or the peqGOLD XChange Plasmid Maxi EF Kit according to the manufacturer's instructions. The DNA concentration was determined spectroscopically by measuring the

absorption at 260 nm using a NanoDrop ND-1000 spectrophotometer. The DNA sequence was validated by sequencing at Microsynth Seqlab (Göttingen, Germany).

3.2.2.3 Agarose gel electrophoresis

To separate DNA fragments, agarose gels were prepared by mixing 1% (*w/v*) agarose with TAE buffer. The suspension was heated to permit the agarose to dissolve. Prior to casting, ROTIGelStain solution (5 µl) was added. DNA samples were mixed with DNA loading buffer (6x) prior to loading. A DNA ladder was used as a standard. Electrophoresis was performed in TAE buffer at 120 V for 30 min – 60 min. DNA fragments were visualized by ROTIGelStain fluorescence under UV irradiation. For cloning procedures, the corresponding DNA fragments were cut out of the gel and extracted using the QIAquick Gel Extraction Kit according to the manufacturer's instructions.

3.2.2.4 Polymerase chain reaction

DNA fragments were amplified by polymerase chain reaction (PCR) using Phusion High-Fidelity DNA polymerase in a thermocycler. Customized primers were synthesized by Sigma-Aldrich. For cloning procedures, primers contained overhangs suitable for restriction digestion. PCR products were separated by agarose gel electrophoresis. To determine the optimal annealing temperature, a thermal gradient PCR was performed. The PCR approach was performed as listed below:

Table 17. PCR approach

Component	Volume (µL)	Final concentration
5x F-518 buffer	10	1x
DMSO (100%)	1.5	3%
Deoxynucleotide (dNTP) mix (10 mM)	2.5	200 µM
Forward primer (10 µM)	5	1 µM
Reverse primer (10 µM)	5	1 µM
Template DNA	0.5	0.4 ng/µL
Phusion polymerase (2 U/ µL)	0.75	0.03 U/µL
Nuclease-free water	to 50 µL	x

Table 18. PCR program

Function	Cycle	Time (min)	Temperature (°C)
Initial denaturation	1	02:00	98
Denaturation	35	00:10	98
Hybridization		01:00	55 - 65
Elongation		01:00 / 1000 nt	72
Elongation	1	10:00	72
Cooling	1	Until further use	4

3.2.2.5 Restriction digestion

Restriction enzymes for digestion of plasmids or PCR products were used with the provided buffer. The following reaction mixture was incubated at 37 °C for 30 min:

Table 19. Protocol for restriction digestion

Component	Volume (µL)	Final concentration
10x FastDigest Green Buffer	5	1x
Restriction enzyme 1	1	0.1-0.4 U/µL
Restriction enzyme 2	1	0.1-0.4 U/µL
DNA	x	0.02 µg/µl
Nuclease-free water	To 50 µL	x

3.2.2.6 DNA ligation

Digested DNA inserts were ligated into a vector with compatible cohesive ends using the T4 DNA ligase with the provided buffer. The vector to insert ratio was 1:5. The reaction mixture was incubated at room temperature for 1 h and then transformed into competent cells.

Table 20. Protocol for DNA ligation

Component	Volume (µL)	Final concentration
10x T4 ligase buffer	2	1x
DNA insert	5	x
DNA vector	1	x
T4 Ligase	1	0.1 U/µL
Nuclease-free water	To 20 µL	x

3.2.2.7 Cloning of lentiviral overexpression plasmids

The pLVX2-CIBN-GFP-CAAX vector [150] including a puromycin resistance gene was a gift from Xavier Trepat (Institute of Bioengineering of Catalonia, Barcelona, Spain) and the pLVX2-BioID2 PuroRes vector was generated by Dr. Tim Schader (Institute for Cardiovascular Physiology, Frankfurt am Main, Germany). Human D-amino acid oxidase 10x His-Tag was amplified from pCMV6-h-D-Amino Acid Oxidase (HG13372-CH, Sino Biological Inc., Wayne, USA) and human NIT2 10x his-tag was amplified from pCMV-h-NIT2 (HG23517-CH, Sino Biological Inc., Wayne, USA). Both, vector and PCR product were digested by restriction enzymes and purified by gel extraction and ligated as described above. The final plasmids were purified and sequenced.

3.2.2.8. Site-directed mutagenesis

Mutagenesis was performed with the Q5 Site-Directed Mutagenesis Kit according to the instructions of the manufacturer. To generate primer sequences and an annealing temperature, the provided online tool NEBaseChanger (NEB) was used. The original plasmid served as template and was amplified with PCR to obtain the individual mutants. The final plasmids were verified by sequencing.

3.2.2.9 Lentiviral CRISPR/Cas9 cloning for genome editing

The lentiviral CRISPR/Cas9 v2 (LCV2) plasmids (puromycin or hygromycin resistance gene for selection) were a gift from Frank Schnütgen (Hematology, Goethe-University, Frankfurt). Guide RNAs were designed using the publicly available CRISPR algorithm (www.benchling.com). Only guide RNAs targeting exons were selected. Oligonucleotides were cloned into the vector via the BsmBI/Esp3I restriction site by “Golden Gate” cloning as previously described [154]. After cloning, the gRNA-containing vectors were purified and sequenced.

3.2.3 Biochemistry

3.2.3.1 Protein isolation, SDS-PAGE and western blotting

Cells were washed twice with Hanks solution and snap-frozen in liquid nitrogen. After cell lysis with Triton X-100 buffer, the extract was centrifuged (10 min, 16,000x*g*, 4 °C). The protein concentration of the supernatant was determined by the Bradford assay. Bradford reagent (ROTI®-Quant) was added to 1:100 diluted samples and absorbance was determined at 595 nm. The protein sample concentration was calculated by using a bovine serum albumin (BSA) protein standard curve with known concentrations. The cell extract was boiled in Laemmli buffer at 95 °C for 5 min. Proteins were separated by sodium dodecyl sulfate polyacrylamide gel electrophoresis (SDS-PAGE). 30 µg of total protein were loaded on a 25 mM Tris/HCl buffered polyacrylamide gel (5% polyacrylamide, pH 6.8) containing 190 mM glycine at 60 V. Next, the protein sample was separated in a TRIS/HCl buffered polyacrylamide gel (pH 8.8) at 120 V. Thereafter, the gels were blotted onto a methanol activated nitrocellulose membrane and blocked in ROTI®block. After incubation with the primary antibody, infrared-fluorescent-dye-conjugated secondary antibodies were used and signals detected with an infrared-based laser scanning detection system.

3.2.3.2 Redox western blots

For peroxiredoxin western blots, cells were exposed to H_2O_2, D-alanine, L-alanine or menadione for 10 min. Alternatively, cells were pre-incubated with the thioredoxin reductase inhibitor auranofin (3 µM, 20 min). Free thiols were blocked with N-ethylmaleimide (NEM, 100 mM). After a wash step with PBS-NEM (100 mM), cells were scraped in alkylation buffer for solubilization. Samples were supplemented with non-reducing sample buffer (-DTT) and separated on an SDS-PAGE gel, followed by western blot analysis.

3.2.3.3 BIAM switch assay

HUVECs were starved overnight in EBM. On the next day, cells were exposed to H_2O_2 (300 µM in EBM) or EBM followed by blocking of free thiols with NEM (100 mM) for 10 min and then washed gently with PBS-NEM (100 mM). Cells were denatured and scraped from the plate in 1.2 ml of cold (4 °C) 20% trichloroacetic acid (TCAA) followed by two washing steps (TCAA 10%, TCAA 5%) and centrifugation for 30 min at 10.000*xg* at 4°C. The pellet was resolved in 200 µL NEM-resolution buffer on a shaker

for 1 h at 37 °C and 1000 rpm. Reaction was stopped by adding 1 ml of ice-cold (-20°C) acetone. Excess NEM was removed by centrifugation for 30 min (10.000x*g*, 4°C) and washing the pellet twice with 1 ml of ice-cold acetone. Initial reduction of oxidized thiols was performed with 200 µL of 4 mM DTT solution for 5 min followed by incubation with 200 µL BIAM (EZ-Link™ Iodoacetyl-PEG2-Biotin)-resolution buffer on a shaker for 1 h at 37°C and 1000 rpm. Excess of BIAM was removed by adding 1 ml of ice-cold acetone and centrifugation for 30 min, 10.000x*g* at 4°C and washing twice with 1 ml of ice-cold acetone. Proteins were resolved in 200 µL resolving buffer. 500 µg protein of the cell sample were used for the pull down of BIAM-labeled proteins with 50 µL streptavidin agarose beads per sample. For western blot analysis, all streptavidin beads of a sample were boiled at 95 °C for 5 min in 50 µL sample buffer.

3.2.3.4 Identification of potentially oxidized cysteines in NIT2

All proteomics experiments were carried out by Dr. Ilka Wittig (Proteomics Core Facility, Institute for Cardiovascular Physiology, Goethe-University Frankfurt/Main). The human NIT2-10x His-Tag plasmid was overexpressed for 48 h in HEK293 cells. Prior to exposure to 300 µM H_2O_2 or medium for 15 min, the cells were starved for 4 h in basal medium with 0.1% FCS. Free thiols were blocked by NEM as described above. Subsequently, cells were lysed in Triton X-100 buffer supplemented with 100 mM NEM. The extract was centrifuged (10 min, 16,000*xg*, 4 °C). Lysate was loaded on HisTrap™ column packed with Ni-sepharose and purified using the Äkta FPLC. Purified NIT2 protein was eluted with a 20 – 500 mM imidazole gradient over 20 min with a flow rate of 1 ml/min. Collected fractions were combined as indicated and proteins were separated on a non-reducing SDS-page and stained with Coomassie. Gel bands were cut out of the gel.

Gel pieces were destained in 60% methanol and 50 mM ammonium bicarbonate (ABC). Proteins were either reduced in 10 mM DTT, 50 mM ABC for 1 h at 56°C and alkylated for 45 min in 30 mM iodoacetamide or left unreduced. Samples were digested for 16 h with trypsin (sequencing grade) at 37 °C in 50 mM ABC, 0.01% Protease Max and 1 mM $CaCl_2$. Peptides were eluted in 30% acetonitrile and 3% formic acid, centrifuged into a fresh 96 well plate, dried in a vacuum concentrator and resolved in 1% acetonitrile and 0.5% formic acid.

Liquid chromatography/mass spectrometry (LC/MS) was performed on Thermo Scientific™ Q Exactive Plus equipped with an ultra-high performance liquid chromatography unit (Thermo Scientific Dionex Ultimate 3000) and a Nanospray Flex Ion-Source. Peptides were loaded on a C18 reversed-phase precolumn followed by separation on a with 2.4 µm Reprosil C18 resin in-house packed picotip emitter tip (diameter 100 µm, 15 cm from New Objectives) using a gradient from 4% acetonitrile, 0.1% formic acid to 30% eluent B (99% acetonitrile, 0.1% formic acid) for 30 min and an additional gradient to 60% for 5 min at a flow rate 400 µL/min and washout with 99% B for 5 min.

MS data were recorded by data dependent acquisition. The full MS scan range was 300 to 2000m/z with resolution of 70000, and an automatic gain control (AGC) value of 3E6 total ion counts with a maximal ion injection time of 160 ms. Only higher charged ions (2+) were selected for MS/MS scans with a resolution of 17500, an isolation window of 2 m/z and an automatic gain control value set to E5 ions with a maximal ion injection time of 150 ms. MS1 Data were acquired in profile mode.seconds.

MS Data were analyzed by PEAKS 7 [155]. Proteins were identified using proteome database UniProtKB for *Homo sapiens* with 74823 entries, released in 05/2020. The enzyme specificity was set to trypsin with one nonspecific end. Carbamidomethylation (+57.02), trioxidation (+47.98), disulfide bridge unpaired fragmentation (-2.02), dioxidation (+31.99), glutathione disulfide (+305.07) and hydrolysis of N-ethylmalemide from cysteines modified with N-ethylmalemide (+125.12) were selected as variable modifications. A false discovery rate (FDR) for the identification protein and peptides was 1%. For quantification of modified cysteines in NIT2 spectral counting of peptides with modified cysteines was performed.

3.2.3.5 Identification of NIT2 interaction partners by BioID2

HUVECs stably overexpressing the BioID2 or the NIT2-BioID2 constructs were seeded out on a 6 cm dish, the next day freshly prepared biotin (final concentration 50 µM) was directly added to the medium for 4 h. Cells were lysed in Triton X-100 buffer. 500 µg of protein of cell lysate was used for the precipitation of biotinylated proteins with 50 µL streptavidin magnetic beads per sample. Beads (n=6) were analyzed by mass spectrometry to identify the interaction partners of NIT2. For western blot analysis, beads were boiled in 50 µL of 1.5x sample buffer.

For MS, beads were supplemented with 6 M guanidinium chloride (GdmCl), 50 mM Tris/HCl,10 mM TCEP and incubated at 95 °C for 5 min. Reduced thiols were alkylated with 40 mM chloroacetamide and sample were diluted with 25 mM Tris/HCl, pH 8.5, 10% acetonitrile to obtain a final GdmCl concentration of 0.6 M. Proteins were digested with 1 µg trypsin (sequencing grade) overnight at 37 °C under gentle agitation. Digestion was stopped by adding TCAA to a final concentration of 0.5% *w/v*. Peptides were loaded on multi-stop-and-go tip (StageTip) containing three C18-disks and three SCX-disks. Purification and elution of peptides was performed as described in Rappsilber *et al*. [156]. Peptides were eluted in wells of microtiter plates and peptides were dried and resolved in 1% acetonitrile, 0.1% formic acid.

For data analysis MaxQuant 1.6.17.0 [157], Perseus 1.6.1.3 [158] and Excel (Microsoft Office 2016) were used. The human reference proteome set (Uniprot, May 2020, 74823 entries) was used to identify peptides and proteins with a FDR less than 1%. Reverse identifications and common contaminants were removed. Proteins were filtered to be identified at least 4 times (n=6) in one experimental group. Missing values were replaced by background values from normal distribution. Significant interacting proteins were determined by Student´s t-Test and permutation based FDR (q value).

3.2.3.6 Mitochondria/ cytosol fractionation

Isolation of a highly enriched mitochondrial fraction from a cytosolic fraction of HUVECs was performed using the mitochondria/cytosol fractionation kit according to the manufacturer’s instructions.

3.2.4 Bioanalytics

3.2.4.1 NIT2 activity assay

The hydroxaminolysis activity assay for NIT2 was performed as previously described [159]. The reaction mixture of 50 µl contained 20 mM succinamate as substrate, 5 mM DTT, 100 mM potassium phosphate buffer (pH 7.4), 100 mM neutralized hydroxylamine-HCl and 12.5 µg of purified NIT2 enzyme (basal or with different concentrations of H_2O_2 as indicated). After incubation at 37 °C, 150 µl of a reaction mixture (0.37 M $FeCl_3$, 0.67 M HCl, and 0.2 M trichloroacetic acid) was added. The absorbance of the succinyl hydroxamate ferric complex was determined at 535 nm. The assay was carried out with or without DTT. The delta was calculated by subtraction

and the difference considered to be due to the activity of the enzyme. For comparisons with NIT2 mutants, NIT2 WT activity was set to 100%.

3.2.4.2 Thermal shift assay

The thermal shift assay was performed together with Dr. Steffen Brunst (Pharmaceutical Institute, Goethe-University, Frankfurt/Main) as previously described [160,161]. Briefly, differential scanning fluorimetry was performed using a PCR plate at a total volume of 40 µL (basal or with different concentrations of H_2O_2 as indicated). Purified NIT2-WT (C_{final} 5 µM) or NIT2C146A (C_{final} 5 µM), Triton X-100 (0.001% w/v), and SYPRO Orange (Thermo Fisher Scientific) (2.5x) were mixed in phosphate buffer with or without DTT (100 mM KPO_4, 5 mM DTT). The samples were measured on an Icycler IQ single-color real time PCR system (λ_{ex} = 490 nm, λ_{em} = 570 nm) and emission was recorded during a temperature gradient of 0.2 °C increase per 24 s (25 – 80 °C). Raw data from both, NIT2-WT and NIT2 C146A, measurements were analyzed directly using a Boltzmann sigmoidal fit in GraphPad Prism. The V_{50} values were considered as the melting temperatures. All samples were measured in triplicates.

3.2.4.3 ROS measurements

Horse radish peroxidase (HRP) can catalyze a reaction between an oxidizing agent (such as H_2O_2) and a hydrogen donor (e.g. a chemiluminescence substrate, such as luminol). H_2O_2 production was measured by HRP coupled chemiluminescence as described previously [162]. Briefly, luminol (100 µm) catalyzed by horseradish peroxidase (HRP, 1U/ml) was used as a probe. 100,000 cells were measured in Hepes-Tyrode (HT) buffer in a Berthold 6-channel luminometer at 37°C. PEG-catalase (500 U/ml) was directly added to the sample during the measurement.

For AmplexRed assay/HRP® assay, cells were seeded out on 12-well plates. The next day, cells were washed with HT buffer and 300 µl of pre-warmed assay buffer (50 µl Amplex Red, 2 U/ml horseradish peroxidase in HT buffer) was added. Cells were treated with D- or L-alanine and left in the incubator for 30 min. 200 µl were transferred to a 96-well plate and the fluorescence was measured (Exc./Em. 540/585 nm) and normalized to protein amount as determined by the Bradford protein assay. To calculate the catalase-sensitive portion fluorescence PEG-catalase (500 U/ml) was added to the assay buffer 30 min before starting the assay.

For functionality of HyPer7, HEK293 cells were transfected with the CAG-LoxP-yDAO-HyPer7-NES construct and a cre-recombinase. Imaging was performed using a LSM 510 Meta. DAO-HyPer7-NES was excited sequentially via 427/10 and 504/12 band-pass excitation filters. Emission was determined every 20 s using a 525/50 bandpass emission filter. After 5-10 images were acquired, D-alanine was added to the cells.

3.2.5 Metabolomics

3.2.5.1 Untargeted metabolomics and data analysis

HUVECs were grown in sister cultures at 37 °C that were treated identically. One dish was used for metabolic analysis while the corresponding sister culture was used to isolate the total RNA for RNA sequencing (MACE) and data normalization. HUVECs at 80% confluence, were starved overnight in endothelial basal medium supplemented with 10 mM L-glutamine and 0.1% FCS. The next day, cells were exposed to H_2O_2 (10 µM or 300 µM), menadione (5 µM), D-alanine (3 mM) or basal medium (control sample) for 3, 10, 30, 90, 270 or 900 min. After exposure, cells were washed with ice-cold PBS and subsequently harvested in 80% LC/MS-grade methanol (Carl Roth, Germany) containing internal standards. Untargeted global metabolomics was performed by Metabolon Inc. (Morrisville, North Carolina, USA) using a Waters ACQUITY ultra-performance liquid chromatography (UPLC) and a Thermo Scientific Q-Exactive high resolution/accurate mass spectrometer interfaced with a heated electrospray ionization (HESI-II) source and Orbitrap mass analyzer operating at 35,000 mass resolution as previously described [163–165]. Briefly, cell samples were extracted with methanol to remove the protein fraction. The extract was divided into five fractions: two for analysis by two separate reverse phase (RP)/UPLC-MS/MS methods with positive ion mode electrospray ionization (ESI), one for analysis by RP/UPLC-MS/MS with negative ion mode ESI, one for analysis by hydrophilic interaction chromatography (HILIC)/UPLC-MS/MS with negative ion mode ESI, and one sample as a backup. Raw data were extracted, peak-identified, and quality control-processed by Metabolon. Compounds were identified by comparison to library entries with over 3300 commercially available purified standard compounds or identified by the spectrum [164]. A batch correction was performed by Metabolon.

Following log transformation and imputation of missing values, if any, with the minimum observed value for each compound, Mixed Model Contrasts were used to identify

biochemicals that differed significantly between experimental. In parallel, metabolomic results were normalized to the RNA values of the corresponding sister culture, missing values were imputed, and statistically analyzed using log transformed data using the two-sample t-test with Welch´s correction. The final output were fold changes (FC) between the experimental groups and the associated p values. P values of < 0.05 were considered significant. Visualizations and plots of metabolomics data were generated using the ggplot (3.3.5) package in R (4.1.1). Each treatment was analyzed with respect to its control.

3.2.5.2 Analysis of TCA cycle metabolites

All targeted metabolomic experiments were carried out by Dr. Stephan Klatt (Metabolomics Core Facility, Institute for Vascular Signaling, Goethe-University Frankfurt/Main). Plasma samples were lysed by adding 10x the volume of methanol (here: 500:50 µL). Next, 10 µL of a 5 µg/mL (of each compound) internal standard mix was added containing the following 8 ^{13}C-labelled metabolites: α-ketoglutaric acid-1-^{13}C, Citric acid-2-^{13}C, Glucose-6-phosphate-6-^{13}C, D-Glucose-1-^{13}C, L-Glutamic acid-2-^{13}C, Pyruvate-1-^{13}C, Succinic acid-2-^{13}C and Itaconic acid-5-^{13}C. Samples were centrifuged at 15,000xg for 5 min at room temperature. The clear supernatant was transferred to a new tube and dried in a vacuum centrifuge. Dried samples were reconstituted in 50 µL water containing 0.5% formic acid, shortly centrifuged to remove remaining debris and transferred to MS glass vials ready to be analyzed.

For analysis of HUVECs, cells were grown on a 10 cm dish until confluence, washed with ice-cold PBS and scratched carefully on ice. After centrifugation (2,400x*g*, 4 min), the cell pellets were lysed by adding 600 µL of 90% methanol and two freeze-thaw cycles, and centrifuged as mentioned above. 300 µL of the clear supernatant were transferred into a clean vial. The supernatant was mixed with internal standard mix, dried and reconstituted as mentioned above. Medium supernatant was mixed with 10 X the volume of methanol (here: 500:50 µL), and metabolites were extracted in the same way as explained for plasma.

Negative ionization ESI-LC MS/MS was performed on an Agilent 1290 Infinity LC system coupled to a QTrap 5500 mass spectrometer. Ion source parameters were as follows: CUR 35 psi, CAD medium, Ion Spray Voltage – 4500 V, TEM 40 °C, GS1 50 psi, GS2 50 psi. In total, 27 TCA metabolites were included in this targeted Multiple

Reaction Monitoring (MRM) screen, including 8 ^{13}C-labeled internal standards and a total of 49 MRMs. TCA metabolites were identified with authentic standards and/or via retention time, elution order from the column and 1-2 transitions. Reversed-phase LC separation was performed by using a Luna Omega 1.6 µm PS C18 (2.1 x 100 mm) column in combination with a UHPLC Fully Porous PS C18 (2.1 mm) as a security guard. Compounds were eluted at a flow rate of 0.4 ml/min and with the following 9.5 min gradient: 0-1 min 99.9% A, 1-4 min 20% A, 4-6.5 min 0.1 % A, 6.5-7.5 min 0.1 % A, 7.5-7.9 min 99.9% A and 7.9-9.5min 99.9% A. Solvent A consisted of water containing 0.5% formic acid and solvent B consisted of 100 % methanol containing 0.5% formic acid. The column oven temperature was set to 40 °C, and the autosampler was set to 4 °C. The injection volume was 5-8 µL.

3.2.5.3 Analysis of amino acids

Extraction of amino acids was done according to the EZfaast protocol with the following modifications: 10 µL of internal standard mix were added to each sample, containing homoarginine, methionine-d_3 and homophenylalanine. Samples were diluted 1:2 in water containing 0.01% formic acid before extraction. Sample reconstitution was done in 50 µL 2:1. Next, samples were centrifuged at 16,000x*g* for 10 min at 4 °C. 300 µL of supernatant were transferred to new tubes and dried down in a vacuum centrifuge. Dried samples were reconstituted in 10 µL of 20 mM HCl. Next, 70 µL of 200 mM boric acid buffer was added, followed by 20 µL of 6-aminoquinolyl-*N*-hydroxysuccinimidyl carbamate (AQC) reagent. Metabolites that contain one or more amine groups are derivatized by AQC. This reagent is used to increase detection of the amine in the MS and enables standard reverse-phase chromatography. Samples were briefly vortexed, centrifuged and incubated for 10 min at 56 °C to derivatize amines. The reaction was stopped by cooling the samples to 4 ºC. Samples were centrifuged one more time, and the supernatant was transferred to MS-vials. Medium supernatants were prepared as follows: 10X the volume of methanol was added to the supernatants (here: 500:50 µL), and metabolites were extracted in the same way as explained above.

Positive ionization ESI-LC MS/MS was performed on an Agilent 1290 Infinity LC system coupled to a QTrap 5500 mass spectrometer. In total, 76 metabolites were included in this targeted Multiple Reaction Monitoring (MRM) screen, including three internal standards and a total of 77 MRMs. Amino acids were identified with authentic

standards and/or via retention time, elution order from the column and 1-2 transitions. Reversed-phase LC separation was performed by using the EZfaast column. Compounds were eluted at a flow rate of 0.25 ml/min and with the following 17 min gradient: 0 min 32% A, 0-13 min 17% A and 13.01-17 min 32% A. Solvent A consisted of 100% water containing 10 mM ammonium formate and solvent B consisted of 100% methanol containing 10 mM ammonium formate. The column oven temperature was set to 40 °C, and the autosampler was set to 4 °C. The injection volume was 1 µL.

3.2.5.4 Establishment of α-ketoglutaramate as a standard for targeted analysis

α-Ketoglutaramate (KGM) is the corresponding α-keto acid of L-glutamine. It is the main metabolite of the glutaminase II pathway and was kindly provided by Travis T. Denton (College of Pharmacy & Pharmaceutical Sciences, Washington State University, Spokane, USA) and synthesized as previously described [118].

The fragmentation behavior of KGM was evaluated on the QTrap 5500 mass spectrometer via direct injection. Different collision energies (CE) were tested in negative ionization mode, and a CE of 40 gave the best fragmentation pattern with the fragments of m/z 144 (parental ion), m/z 126 (most abundant), m/z 82 (2nd most abundant) and m/z 42 (3rd most abundant).

3.2.6 Transcriptomics

3.2.6.1 RNA isolation

Total RNA was isolated using the RNA Mini Kit (Bio&Sell) according to the manufacturer's instructions. The RNA concentration was determined using the NanoDrop1000 device.

3.2.6.2 MACE sequencing and data analysis

RNA of sister cultures was isolated with the RNA Mini Kit combined with on-column DNase digestion to avoid contamination by genomic DNA. The libraries were prepared using GenXPro MACE kit v.2.0. RNA was sheared to an average size of 350 bps followed by poly-A specific cDNA synthesis. The PCR product was purified by SPRI (solid phase reversible immobilization) purification and the final product was quality controlled on a PerkinElmer LabChip GXII. The fragments were ligated to "TrueQuant" (from GenXPro, containing unique molecule identifiers). This unique identifier helps to remove PCR duplicates. MACE-tags were amplified with 10 PCR cycles and the

libraries were sequenced on an Illumina NextSeq 500 machine by GenXPro (Frankfurt/Main, Germany). MACE sequencing reads for all samples were quantified against the *hg38* transcriptome (obtained from *Ensembl)* using *Salmon* (1.5.2) [166,167]. Reads not aligned to the transcriptome were discarded at this point. Differential gene expression analysis was performed using *DESeq2* (1.32.0) [168]. Raw transcript counts were summed per gene and used in the standard *DESeq2* differential gene expression analysis workflow, using a negative binomial test over gene counts in each of the combinations of conditions. Batch information was also included in the contrast formula. PCA plots were generated using the raw gene counts after variance stabilizing transformation (VST), using the *DESeq2* function *plotPCA*. Significant differences in gene expression between conditions were those with an adjusted (Benjamini-Hochberg) *P* value < 0.05. Differentially expressed genes per contrast were subjected to pathway enrichment analysis in *R* using *ClusterProfiler* (4.0.5) and the *enrichKEGG* function [169]. Significantly enriched pathways versus a default random background geneset were those with an adjusted (Benjamini-Hochberg) *P* value < 0.05. Visualizations and plots were generated using *ggplot2* (3.3.5) [170]. Gene heatmaps were hierarchically clustered in *R* using *hclust* with Euclidean distances and the *ward.D* method.

3.2.7 Physiological assays

3.2.7.1 Spheroid outgrowth assay

Spheroid outgrowth assays were performed as previously described [171]. HUVECs spheroids were stimulated for 16 h with human recombinant VEGF-A 165 (50 ng/ml). Images were generated with the Evos XL Core. The quantitative analysis of sprout number and cumulative length was calculated with the AxioVision software.

3.2.7.2 Proliferation assay

3,000 Cells were seeded out on a 96-well plate. Nuclei were stained using the IncuCyte Nuclight Rapid Red Dye according to the manufacturer's instructions. Proliferation was monitored by live cell imaging using the IncuCyte ZOOM platform.

3.2.7.3 Cell migration

A scratch wound-healing assay was performed in 96-well plates. The HUVECs monolayer was scratched using the Incucyte WoundMaker. Cell migration into the

scratched area was monitored by live cell imaging and analyzed using the IncuCyte ZOOM platform.

3.2.8 Animal experiments

3.2.8.1 Knock-in mice

Synthetic constructs for the generation of transgenic mice were obtained from Eurofins (Ebersberg, Germany). The constructs contain the target sequence to be inserted into the mouse genome including homologous flanking regions to the mouse genome for targeted insertion (knock-in). Synthetic constructs were sent to the University of Tsukuba (Department of Anatomy and Embryology, Faculty of Medicine, Tsukuba, Ibaraki, Japan) for generation of CRIPSR-mediated knock-in mice [172].

3.2.8.1 Sample preparation

For the isolation of protein, tissue was pulverized in liquid nitrogen. A small amount of organ powder was lysed in Triton X-100 buffer and subsequently samples were rotated for 30 min at 4°C. Thereafter, the tissue lysate was centrifuged (10 min, 16,000xg at 4°C) and the supernatant was used for Western blot analysis. Endothelial proteins and smooth muscle cell (SMC) proteins were enriched from aortic rings with a mild triton-based lysis. Mouse lung endothelial cells were isolated by using CD144 coated beads as described previously [173].

3.2.9 Protein modelling

The human NIT2 protein structure was modelled by Prof. Dr. Eugen Proschak (Pharmaceutical Institute, Goethe-University, Frankfurt/Main) and visualized based on the structure of mouse NIT2 [134,174] by manually exchanging the amino acids that differ between human and mouse. This was done using the software MOE 2019.10. Potentially oxidized cysteines in mouse NIT2 were predicted using a machine learning algorithm as previously described [175].

3.2.10 Statistics

Data are represented as mean ± standard error of the mean. Calculations were performed with Prism 9.2.0. The latter was also used to test for normal distribution and similarity of variance. In the case of multiple testing, a Bonferroni correction was applied. For multiple group comparisons, analysis of variance followed by post hoc testing was performed. Individual statistics of dependent samples were performed by

paired t-test, of unpaired samples by unpaired t-test, and, if not normally distributed, by the Mann-Whitney *U* test. P values of <0.05 were considered significant. Unless otherwise indicated, *n* indicates the number of individual experiments.

4. Results

4.1 DAO as a tool to study redox signaling in HUVECs

4.1.1 DAO is an efficient tool to produce H_2O_2 intracellularly

To establish a method that allows controlled production of intracellular H_2O_2 in endothelial cells (ECs), we cloned the human D-amino acid oxidase (DAO) gene into a lentiviral plasmid to express the enzyme in human umbilical vein endothelial cells (HUVECs). DAO converts D-amino acids into their corresponding α-imino acids and H_2O_2. Thereby, H_2O_2 is generated intracellularly after the addition of D-alanine. The imine is then non-enzymatically hydrolyzed to its corresponding α-keto acid (**Fig. 9A**) [149,176,177]. Immunofluorescence shows expression of DAO (red) in HUVECs compared to cells that were transduced with a control virus containing an empty vector (**Fig. 9B**).

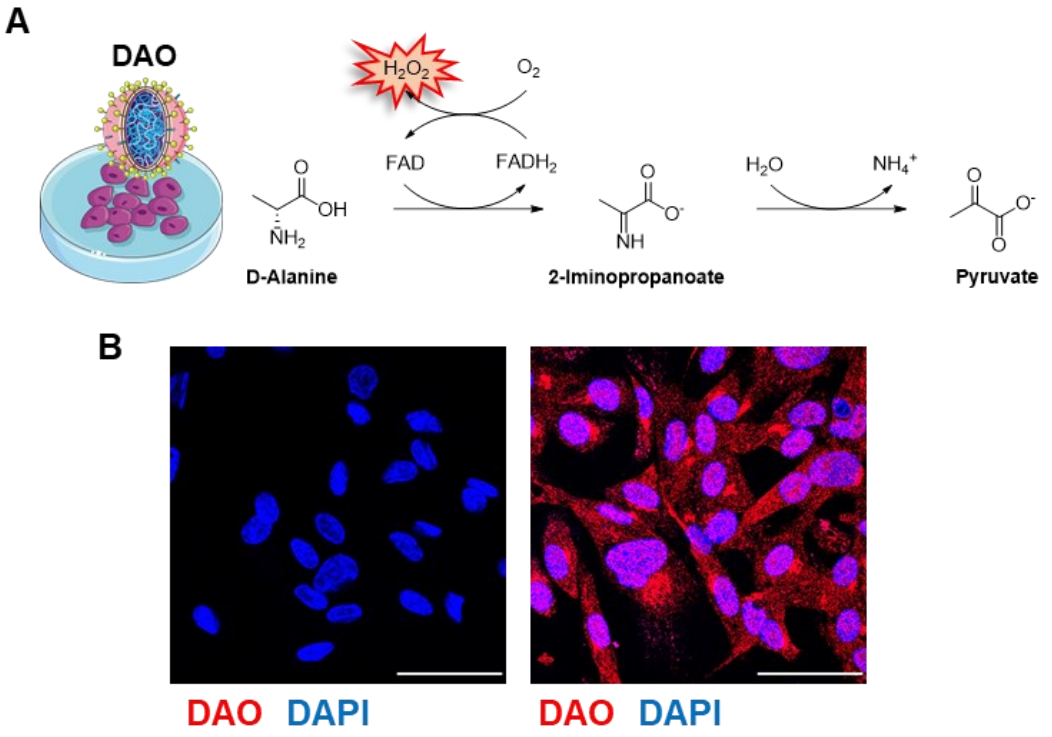

Figure 9. DAO as a tool to generate intracellular H_2O_2
(**A**) Reaction catalyzed by DAO. (**B**) Overexpression of DAO in HUVECs is shown by immunofluorescence. 40x magnification. Scale bar indicates 50 µm. Figure published in Müller *et al.* (2022) [177].

To test the activity of the enzyme, DAO-derived H_2O_2 was measured by two different assays: luminol/HRP chemiluminescence and AmplexRed®/HRP fluorescence. Addition of 3 mM D-alanine resulted in a strong increase in luminol/HRP chemiluminescence in comparison to 3 mM L-alanine (**Fig. 10A**). Likewise in the AmplexRed® assay, increasing concentrations of D-alanine (1-10 mM) raised the fluorescence signal (**Fig. 10B**). Importantly, pre-incubation with PEG-catalase significantly reduced the signal elicited by D-alanine. Thus, DAO, when overexpressed in HUVECs, continuously produces H_2O_2 upon stimulation with D-alanine and could serve as a tool to study redox signaling in HUVECs.

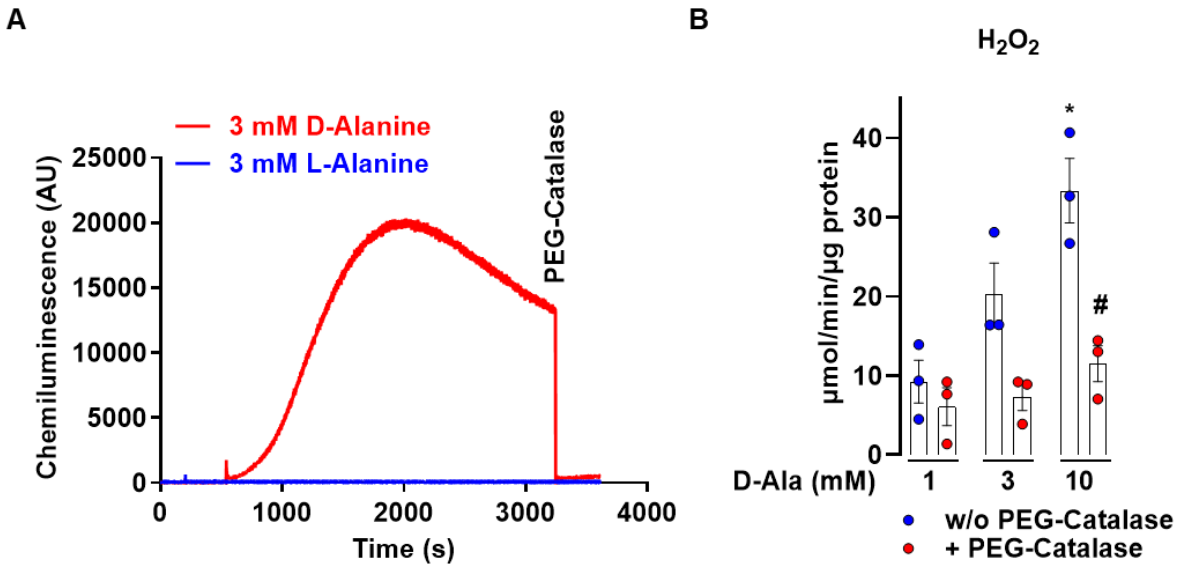

Figure 10. Characterization of DAO as a tool to generate intracellular H_2O_2 in HUVECs
H_2O_2 measurements in HUVECs using luminol/HRP (**A**) and AmplexRed®/HRP (**B**) coupled chemiluminescence. *p<0.05 10 mM D-alanine vs. 1 mM D-alanine; #p<0.05 10 mM D-alanine plus vs. minus PEG-catalase. One-way-ANOVA with Bonferroni correction. Figure published in Müller *et al.* (2022) [177].

After establishing a system to generate intracellular H_2O_2, we examined redox sensor proteins in detail to detect disturbances in redox homeostasis by DAO-derived H_2O_2. Peroxiredoxins (Prx), being thiol-specific antioxidants, not only scavenge H_2O_2 but also can serve as redox sensors. H_2O_2 can react with the peroxidatic cysteine residue to form a sulfenic acid (-SOH) and thereby protect other cellular components from oxidative damage. This sulfenic acid condenses with the thiol group at the resolving cysteine of another close-by Prx to form a disulfide bond. This disulfide bond can be

reduced by thioredoxin. Thereby, Prx can form a dimer or multimer with other Prx enzymes. Prx dimers or monomers are considered to be a robust readout for intracellular H_2O_2 [162,178]. Furthermore, high concentrations of H_2O_2 can lead to hyperoxidation of the peroxidatic cysteine which leads to the formation of a sulfinic (-SO_2H) or a sulfonic (-SO_3^-) acid. Cysteine sulfinic acid can be reduced back to a thiol by sulfiredoxin or sestrin while the oxidation to sulfonic acid is irreversible [179]. The assay was performed with different concentrations of D- and L-alanine as well as exogenously added H_2O_2 at a high concentration of 300 µM. Free thiols were blocked using N-ethylmaleimide (NEM) to avoid any artificial oxidation of cysteine residues. Prx-dimerization is detectable by western blot analysis under non-reducing (-DTT) conditions.

DAO-derived H_2O_2 led to a dose-dependent increase in dimerization of Prx-1 and Prx-2 isozymes but not of Prx-3. Moreover, exposure to D-alanine increased formation of the thioredoxin-S-S-peroxiredoxin dimer. Interestingly, not even the highest concentration of D-alanine (10 mM) led to hyperoxidation (Prx-SO_3). However, Prx-SO_3 was readily detected after exposure of cells to 300 µM extracellular H_2O_2 (**Fig. 11A**).

We speculated that Prx-SO_3 would only be detectable if the thioredoxin reductase system, which restores reduced peroxiredoxin, is inhibited. To assess this, we pre-incubated cells with auranofin (inhibitor of the thioredoxin reductase) prior to the addition of D-alanine. Furthermore, menadione, a polycyclic aromatic ketone to generate intracellular superoxide anions was included [180]. Blocking the thioredoxin reductase increased the thioredoxin-S-S-peroxiredoxin dimer but did not lead to Prx-SO_3 formation upon exposure to D-alanine. Strikingly, pre-incubation with auranofin also did not lead to hyperoxidation (Prx-SO_3), when the cells were treated with menadione. Instead, it led to a complete loss of the Prx1 monomer (**Fig. 11B**).

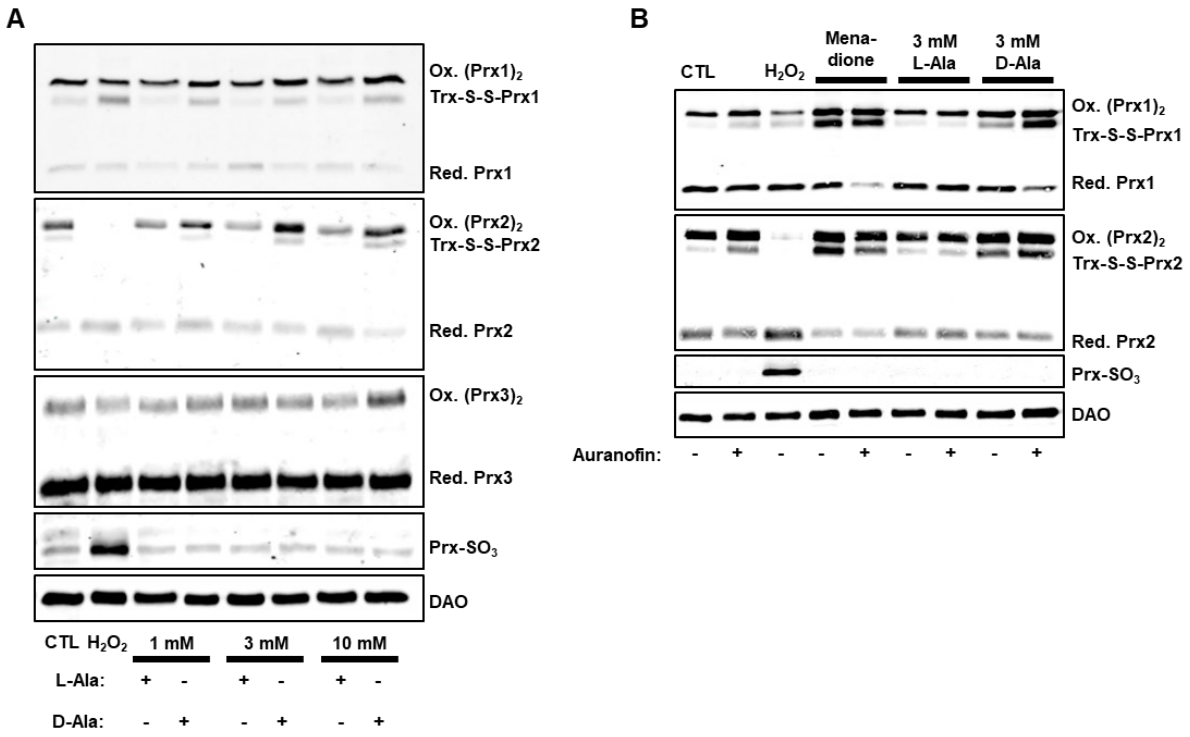

Figure 11. DAO-derived H_2O_2 oxidizes peroxiredoxins in HUVECs
(**A**) Western blot for peroxiredoxins (Prx) after exposure to different concentrations (as indicated) of L- or D-alanine or H_2O_2 (300 µM) under non-reducing (-DTT) conditions. (**B**) Western blot for peroxiredoxins (Prx) after exposure to different concentrations (as indicated) of L- or D-alanine, menadione (5 µM) or H_2O_2 (300 µM) with or without pre-treatment with auranofin (20 min, 3 µM) under non-reducing (-DTT) conditions. (**A**/**B**) Free thiols were blocked with NEM. A total of 30 µg of protein were loaded to each lane. Figure published in Müller *et al.* (2022) [177].

4.1.2 DAO knock-in mouse

To translate the DAO approach into an *in vivo* model, we generated a DAO knock-in mouse line. A DAO-HyPer7-NES construct under the control of the CAG promoter was designed *in-silico* together with Prof. Dr. Ralf Gilsbach (Institute for Cardiovascular Physiology, Goethe University, Frankfurt/Main) using SnapGene (5.3). Due to higher catalytic activity, the construct included the yeast homologue of DAO. The enzyme was fused to HyPer7, a bright, pH-stable and sensitive fluorescent ratiometric H_2O_2 reporter protein [181]. After oxidation, the excitation/ absorption spectrum of HyPer7 is changed in a ratiometric way, with a decrease at 400 nm and an increase of the 499 nm peak. Promoter and coding sequence were separated by three SV40 poly(A) signals that were flanked by one LoxP site each (**Fig. 12**). This allows gene expression after recombination using a Cre-recombinase. Thereby, a cell-type specific transgene-expressing mouse can be generated (e.g. crossing with Cdh5Cre mice). Additionally, the construct contained specific overhangs for integration into the Hipp11 locus of mice. The murine Hipp11 intergenic region can facilitate highly efficient integration of a large transgene by means of CRISPR/Cas9 mediated homology directed repair. The Hipp11 locus is an active region of the genome that allows stable expression of transgenes (safe harbor).

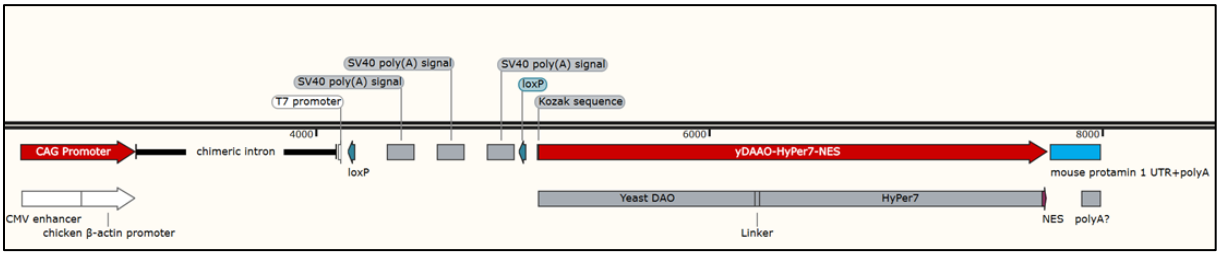

Figure 12. A synthetic construct to generate a cell type specific DAO knock-in mouse
The yeast isoform of DAO fused to HyPer7 under control of the CAG promoter. The construct contains specific overhangs for integration into the Hipp11 locus.

Functionality of the synthetic construct was tested by overexpression in HEK293 cells. Addition of 10 mM D-Alanine resulted in a strong formation of H_2O_2 as elicited by luminol/HRP coupled chemiluminescence when simultaneously overexpressing a cre-recombinase. No signal was elicited by addition of 10 mM D-alanine when the cre-recombinase was missing (**Fig. 13A**). Furthermore, imaging of HyPer7 showed an increase of the 499 nm peak and a decrease of the 400 nm peak after addition of 10

mM D-alanine as shown by an increase in red fluorescence (**Fig. 13B**). The DAO knock-in mouse line will allow cell type specific production of intracellular H_2O_2 by feeding D-alanine to the mice. Thereby, it is possible to identify the consequences of ROS formation for the cellular function, the gene expression and the intercellular communication.

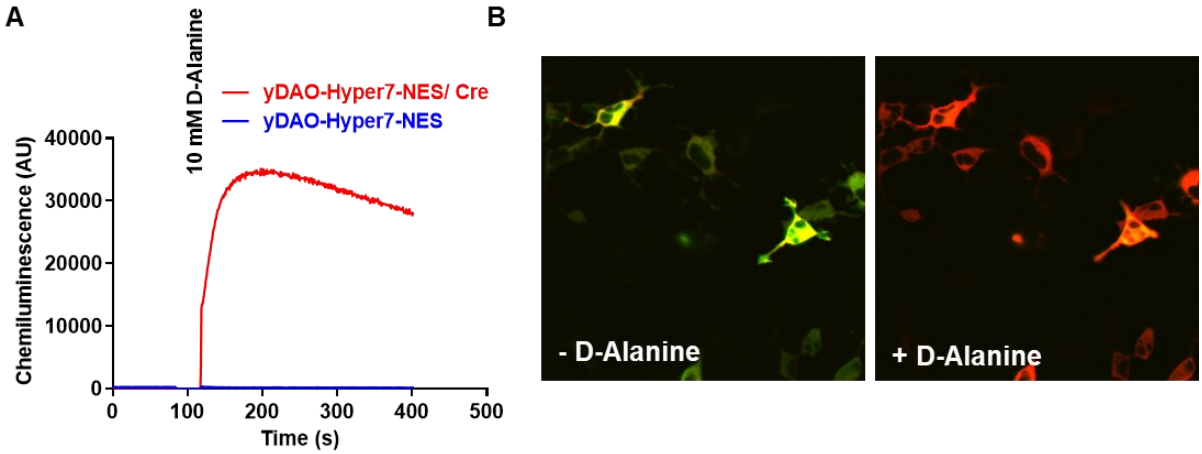

Figure 13. Characterization of yDAO-HyPer7 construct in HEK293 cells
(**A**) Luminol/HRP coupled chemiluminescence of HEK293 cells overexpressing a yDAO-HyPer7 plasmid with (red) or without (blue) simultaneous overexpression of a plasmid encoding for a cre-recombinase. (**B**) Images of HyPer7 in HEK293 cells overexpressing yDAO-HyPer7 together with a cre-recombinase before (left) and after (right) the addition of D-alanine. 40x magnification.

4.2 Metabolic and transcriptomic response of HUVECs upon exposure to different types of ROS

4.2.1 Experimental design

Conclusions regarding the biological role of H_2O_2 in signaling are based on findings generated by the addition of extracellular H_2O_2 to cultured cells. However, this does not reflect the dynamics of intracellular H_2O_2 flux in the regulation of signaling events. Therefore, an untargeted large-scale experiment was designed to study the short-term and long-term metabolic and transcriptomic changes to different types and concentrations of ROS in HUVECs. HUVECs stably overexpressing DAO (DAO-HUVECs) were exposed to 3 mM D-alanine to generate intracellular H_2O_2. For comparison to extracellular H_2O_2, cells were exposed to different concentrations of exogenous H_2O_2 (10 µM and 300 µM). Additionally, we included menadione (5 µM), a polycyclic aromatic ketone, to acutely generate intracellular superoxide anions ($O_2^{\bullet-}$) by redox-cycling [180]. Each stimulation time point included a control sample in which the cells were exposed to basal medium. The samples were subjected to global untargeted metabolomics and RNA sequencing (MACE). All samples were measured in triplicates resulting in 90 samples for metabolic profiling and 60 samples for MACE sequencing (**Fig. 14**).

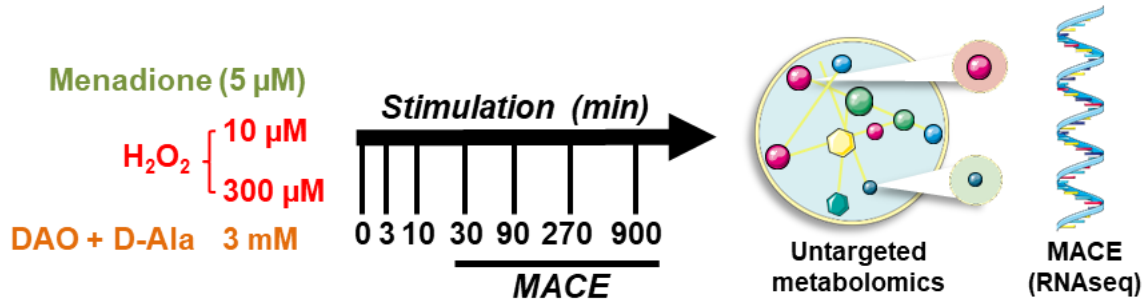

Figure 14. Experimental design
Experimental design to study the short-term and long-term metabolic and genetic response of HUVECs to different types and concentrations of ROS. Figure published in Müller *et al.* (2022) [177].

In total, 387 compounds of known or predicted identity (named biochemicals) were identified by non-targeted metabolite profiling by Metabolon Inc. (Morrisville, USA). The total number of significantly changed ($p<0.05$) biochemicals compared to the control (all stimulation time points combined) for each treatment is shown in **Table 21**.

Table 21. Total biochemicals (RNA-normalized) changed in untargeted metabolomics approach

Treatment	Total biochemicals p<0.05
10 µM H_2O_2	81
300 µM H_2O_2	384
3 mM D-Alanine	44
5 µM Menadione	114

4.2.2 ROS differentially alter the metabolic and transcriptomic response of HUVECs

Untargeted metabolomics revealed a high degree of dissimilarity in the number of intracellular metabolites altered by the different types of ROS (**Fig. 15**). DAO-derived H_2O_2 induced only a subtle change in the metabolome over the course of time. Low H_2O_2 (10 µM) and menadione (5 µM) showed a similar trend but with a peak at time 270 min. The major changes in the metabolome were elicited by high concentrations of exogenous H_2O_2 (300 µM).

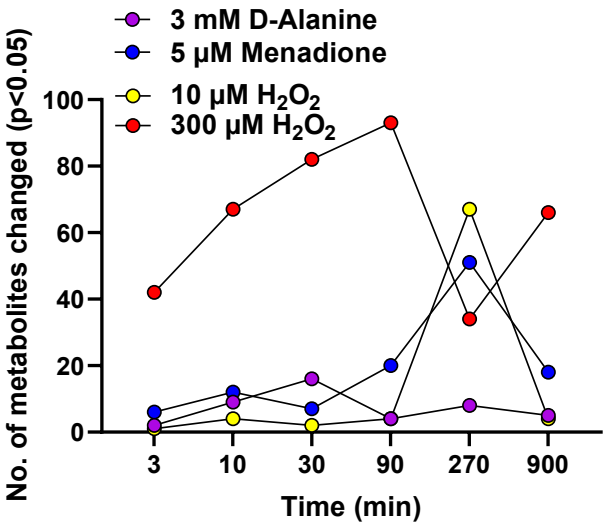

Figure 15. Metabolic changes after exposure to different types and concentrations of ROS
Number of intracellular metabolites significantly (p<0.05) changed over the course of time after exposure to different types and concentrations of ROS. n=3. Figure published in Müller *et al.* (2022) [177].

The glutathione metabolism is important for antioxidant defense. Therefore, we analyzed how this pathway was affected by the different oxidants. High H_2O_2 had the strongest effect on glutathione metabolism leading to a significant increase in oxidized glutathione species such as cysteine-glutathione disulfide. Furthermore, reduced

glutathione transiently decreased after exposure to 300 µM H_2O_2 but recovered within 30 min. Unexpectedly, these effects were not observable for DAO-derived H_2O_2 or exposure to menadione (**Fig. 16A**).

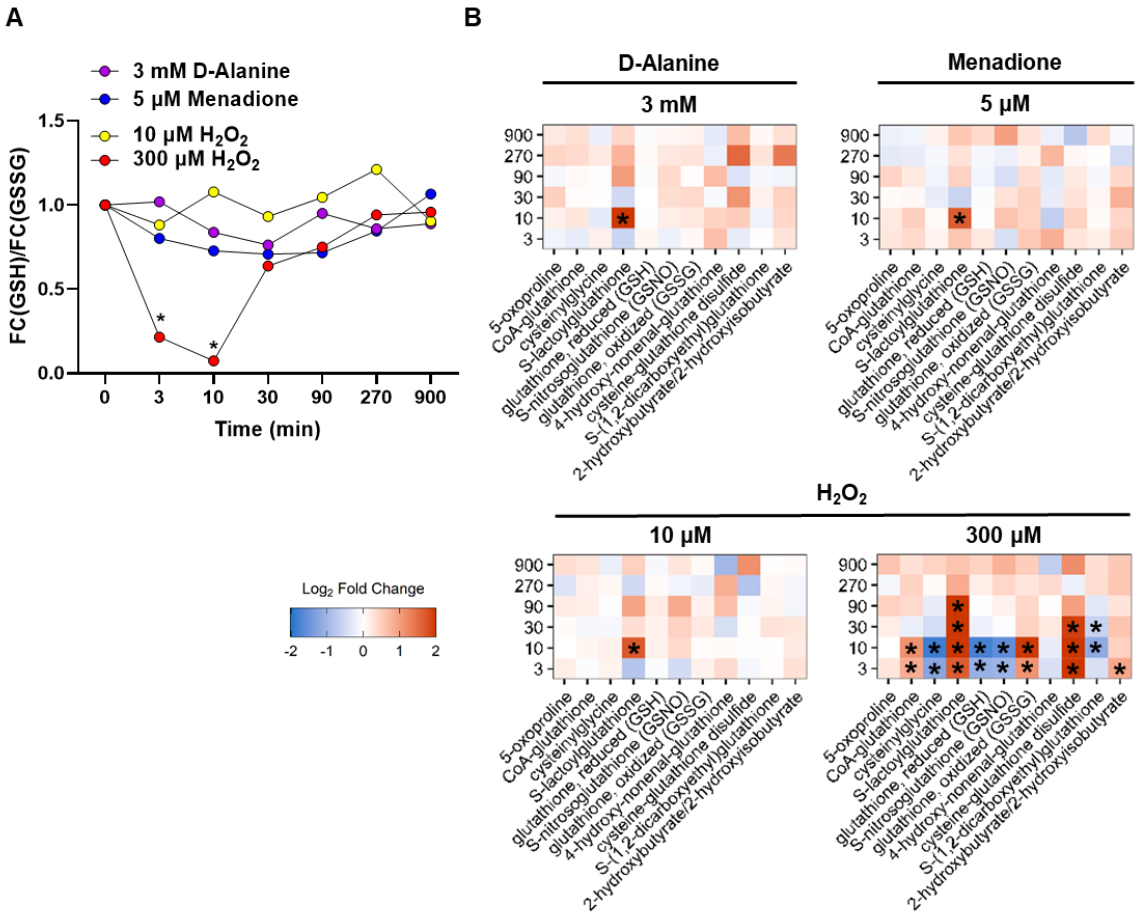

Figure 16. Changes in glutathione metabolism upon exposure to different types of ROS
(**A**) Fold changes (FC) in the GSH/GSSG ratio after exposure to different types and concentration of ROS over the course of time. (**B**) Time course metabolic log_2 fold changes in glutathione metabolism. (**A**/**B**) * indicates significantly changed metabolite ($p<0.05$) calculated by the two-sample t-test with Welch's correction. n=3. Figure published in Müller *et al.* (2022) [177].

Nevertheless, all types of ROS significantly increased S-lactoylglutathione at 10 min (**Fig. 16B**).This metabolite is an intermediate in methylglyoxal detoxification pathway, which is generated as a side product of upper glycolysis. Methylglyoxal is detoxified by the glyoxalase system, a composition of two enzymes, in which the first enzyme (glyoxalase I) converts the hemithioacetal that forms spontaneously between methylglyoxal and GSH to S-D-lactoylglutathione. The second enzyme (glyoxalase II) converts S-D-lactoylglutathione to GSH and D-lactate. An increase in methyglyoxal

can occur under stress situations such as elevated ROS formation [182]. Methylglyoxal itself is highly reactive and can therefore not be detected with the analytic methods used here. A close inspection of glycolysis revealed a general increase in metabolites of the upper glycolysis pathway (e.g. dihydroxyacetone phosphate, DHAP) and a decrease in metabolites of the lower glycolysis pathway (e.g. phosphoenolpyruvate, PEP) in response to exposure with H_2O_2 (300 µM). This effect was however not observed after exposure to DAO-derived H_2O_2 or to menadione. Recent studies have demonstrated that a short-term antioxidant response can be mediated by redox-sensitive enzymes in the lower glycolysis pathway. High H_2O_2 inhibits glyceraldehyde 3-phosphate dehydrogenase (GAPDH) by promoting the formation of an intermolecular disulfide bond [183,184]. Therefore, an accumulation of DHAP is noticeable after exposure to high H_2O_2. The increase in DHAP is consistent with the accumulation of S-lactoylglutathione as methyglyoxal is formed during the non-enzymatic phosphate elimination of DHAP (**Fig. 17**).

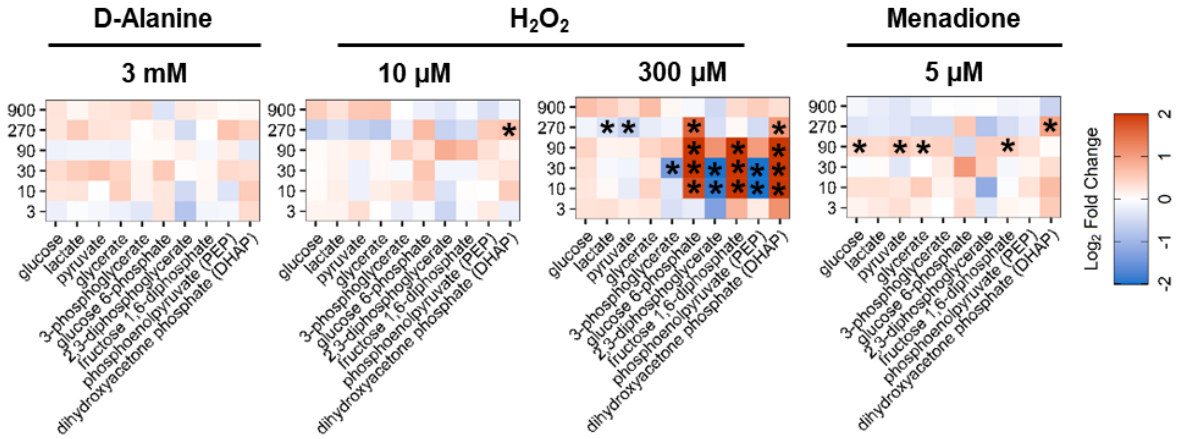

Figure 17. Changes in glycolysis of HUVECs upon exposure to different types of ROS
Time course metabolic log_2 fold changes in glucose metabolism. * indicates significantly changed metabolite ($p<0.05$) calculated by the two-sample t-test with Welch's correction. n=3. Figure published in Müller *et al.* (2022) [177].

In order to identify whether the type, the concentration of ROS and the site of ROS (intra- *vs.* extracellular) exposure elicit a differential gene expression, MACE sequencing was performed. Exposure to 300 µM H_2O_2 induced most transcriptomic changes (3540 DEGs, differentially expressed genes) in comparison to DAO-derived H_2O_2 elicited by 3 mM D-alanine (1575 DEGs) and menadione (1236 DEGs). 10 µM

H_2O_2 led to no significant differences in expression as compared to untreated HUVECs. Thus, we further focused our analysis on 300 µM H_2O_2, 3 mM D-alanine and 5 µM menadione.

To gain a comprehensive picture of the molecular pathways affected by the different ROS, a pathway enrichment analysis using the Kyoto Encyclopedia of Genes and Genome (KEGG) database considering the significantly (p_{adj} < 0.05) changed genes for all time points was performed. High H_2O_2 concentration (300 µM) significantly induced genes of the p53 signaling pathway and cell cycle-related genes. Stress-responsive genes such as the cell cycle regulator GADD45A (Growth Arrest and DNA Damage Inducible Alpha) and PHLDA3 (Pleckstrin Homology Like Domain Family A Member 3) were increased after exposure to high concentration of H_2O_2. Moreover, induction of CDKN1A/p21 (Cyclin Dependent Kinase Inhibitor 1A) suggests that H_2O_2 promoted a senescent phenotype in ECs. This suggestion is in line with the known effect of H_2O_2 for stress-induced cell cycle arrest [18]. Interestingly, this effect did not occur with exposure to menadione or to D-alanine. Nevertheless, all oxidants significantly changed ribosome-associated RNAs (rRNA). Indeed, rRNAs can be chemically modified by ROS which we assume leads to an upregulation of the rRNA transcripts necessary to maintain ribosomal functionality (**Fig. 18**).

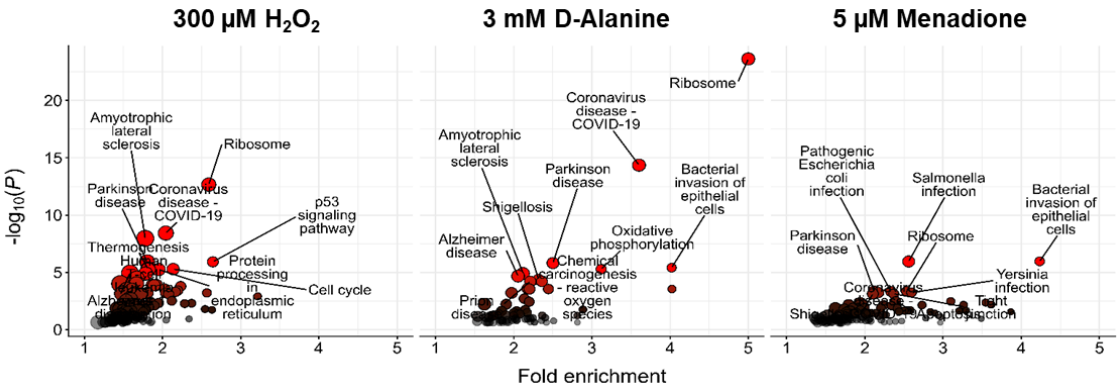

Figure 18. rRNAs are commonly changed upon exposure to different types of ROS
Pathway enrichment analysis using the Kyoto Encyclopaedia of Genes and Genome (KEGG) database considering significantly changed genes (p_{adj}<0.05) after exposure to different types and concentrations of ROS. n=3. Figure published in Müller *et al.* (2022) [177].

To summarize, intracellular DAO-derived H_2O_2 and exposure to menadione leads to Prx-dimerization and minor metabolic and transcriptomic changes. In contrast, exogenous H_2O_2 (300µM) induced the largest metabolic and genetic changes. Furthermore, exposure to high H_2O_2 led to Prx-hyperoxidation. Therefore, we assume that the site and the concentration of ROS are necessary to elicit metabolic and transcriptomic changes. On the other hand, DAO-derived H_2O_2 is generated intracellularly and readily scavenged by the antioxidant system.

4.2.3 Metabolic response of HUVECs upon exposure to 300 µM H_2O_2

As DAO-derived H_2O_2 only led to subtle metabolic changes, we focused on the response to high (300 µM) concentrations of H_2O_2. A principal-component analysis (PCA) of the metabolome and transcriptome was performed (**Fig. 19A**) to asses both the dynamics and the timing of the metabolic response to H_2O_2. The greatest differences were observed already after 3 min and reverted after 270 min. Next, a pathway enrichment analysis (**Fig. 19B**) for the significantly changed metabolites ($p < 0.05$) for each time point was performed. It showed a strong enrichment for specific metabolic pathways such as glutamate, cysteine and methionine metabolism.

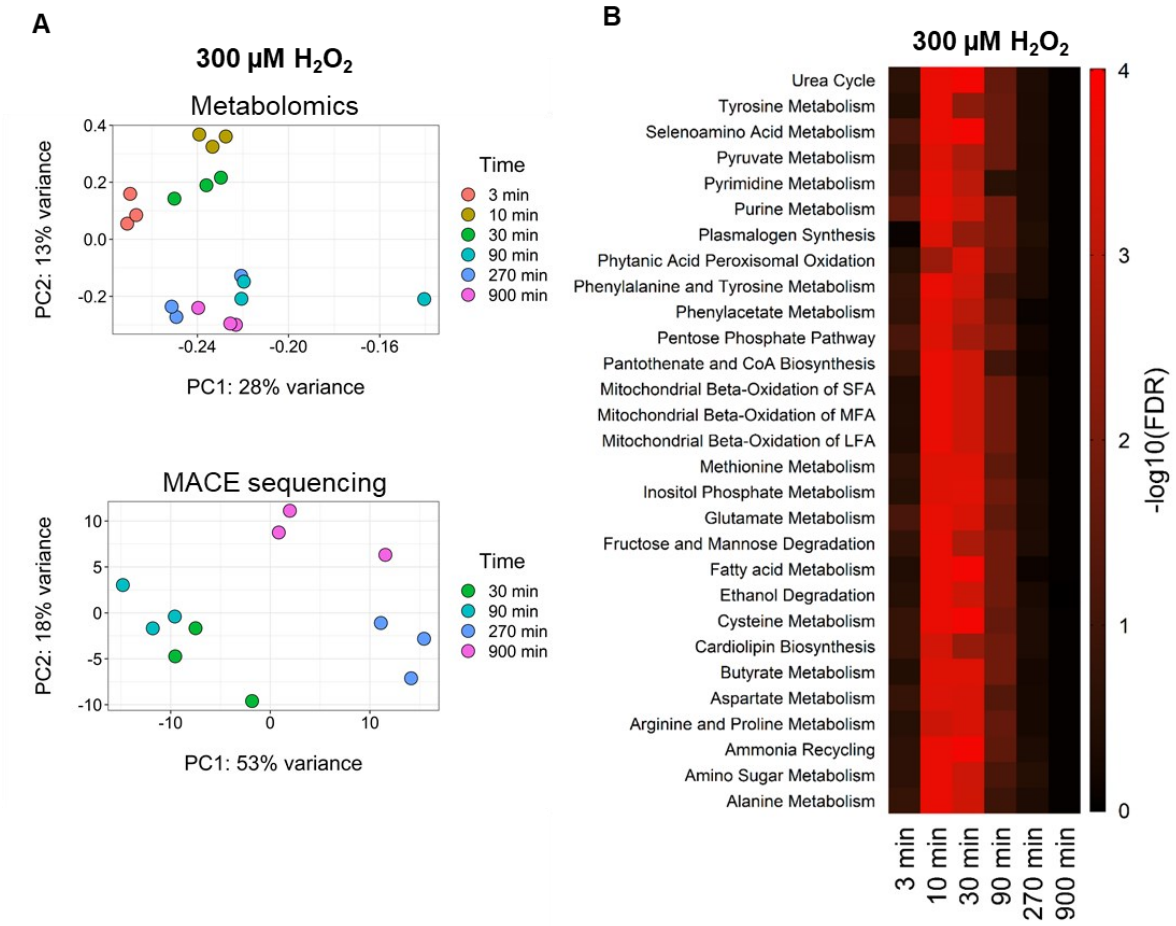

Figure 19. Metabolic response by HUVECs upon exposure to H_2O_2
(**A**) Principial-component analysis (PCA) of intracellular metabolites and changes in gene expression of H_2O_2-exposed HUVECs. (**B**) Metabolic pathway enrichment analysis. n=3.

4.2.4 300 µM H_2O_2 transiently increases α-ketoglutaramate levels in HUVECs

To identify novel redox-sensitive pathways in HUVECs, we examined the individual metabolites changed in the TCA cycle and glutamine metabolism. Menadione (5 µM), to generate intracellular superoxide anions, led to a significant decrease in relative isocitrate levels (**Fig. 20A**). Importantly, the downstream metabolites, especially α-ketoglutarate, were not affected by menadione exposure (**Fig. 20B**). This finding is consistent with the known inhibition of aconitase by superoxide anions [185].

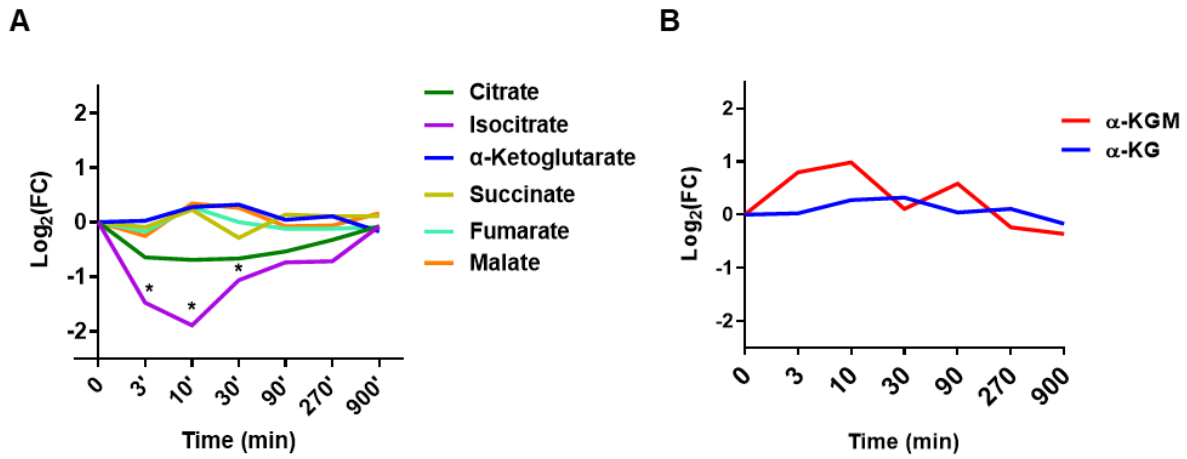

Figure 20. Exposure to menadione reduces relative isocitrate levels in HUVECs
(**A**) Relative log_2 fold changes (FC) in TCA cycle metabolites after exposure to 5 µM menadione. (**B**) Relative log_2 fold (FC) changes in α-ketoglutarate and α-ketoglutaramate levels after exposure to 5 µM menadione. * indicates significantly changed metabolite ($p<0.05$) calculated by the two-sample t-test with Welch's correction. 5 µM menadione *vs.* CTL. α-KGM, α-ketoglutaramate; α-KG, α-ketoglutarate. n=3.

H_2O_2 (300 µM) elicited a different result and affected several TCA cycle metabolites. Isocitrate and its downstream metabolites such as α-ketoglutarate were significantly reduced (**Fig. 21A/B**). As 70% of the TCA cycle carbons in HUVECs are derived from L-glutamine [91,92], the results may indicate that H_2O_2 directly affects the glutamine metabolism of HUVECs. Interestingly with exposure to high H_2O_2, the corresponding α-keto acid of glutamine, namely α-ketoglutaramate (KGM), was significantly increased which was accompanied by a decrease in α-ketoglutarate. KGM is the key metabolite of the glutaminase II pathway and is hydrolyzed to α-ketoglutarate by the ω-amidase/NIT2 [111].

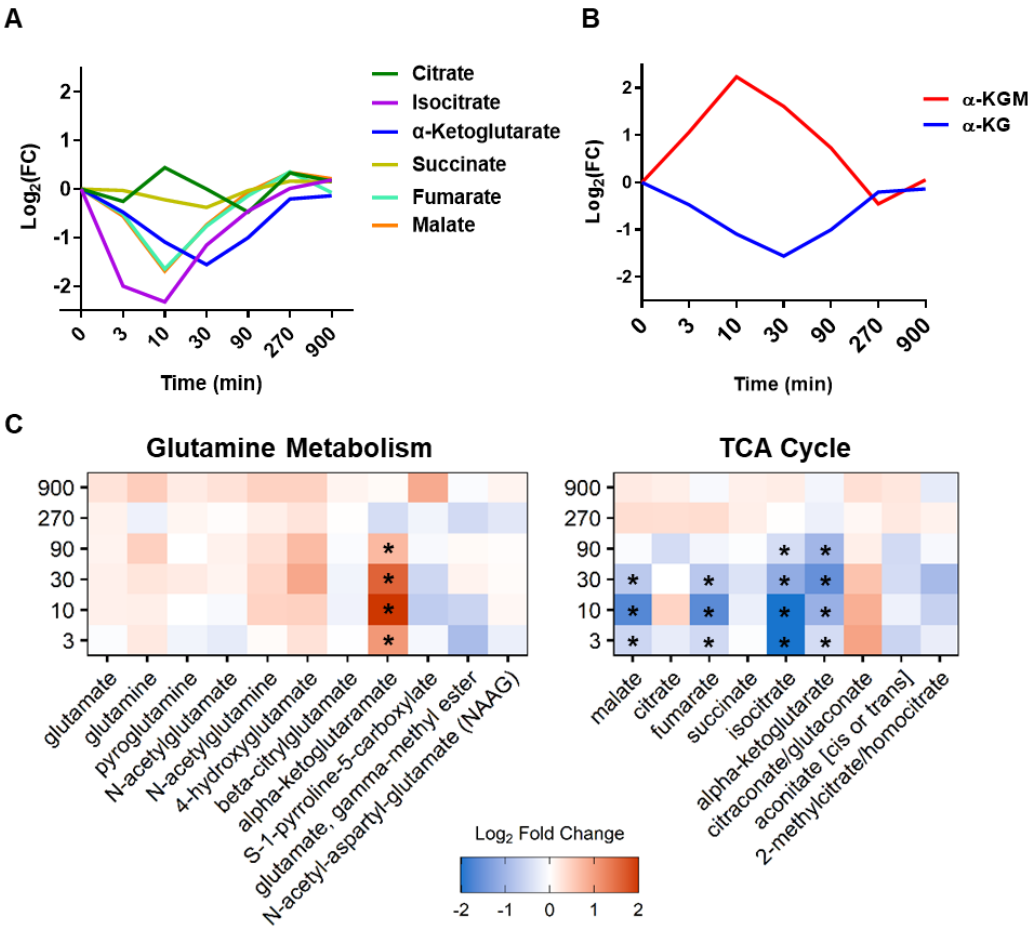

Figure 21. High H_2O_2 affects glutamine metabolism of HUVECs
(**A**) Changes in TCA cycle metabolites after exposure to 300 µM H_2O_2. (**B**) Changes in α-ketoglutarate and α-ketoglutaramate levels after exposure to 300 µM H_2O_2. (**C**) Heat maps of glutamine metabolism (left) and TCA cycle (right) metabolites after exposure to 300 µM H_2O_2. * indicates significantly changed metabolite ($p<0.05$) calculated by the two-sample t-test with Welch's correction. 300 µM H_2O_2 *vs*. CTL. n=3. α-KGM, α-ketoglutaramate; α-KG, α-ketoglutarate.

The increase in KGM with a concomitant drop in α-ketoglutarate may suggest that an enzyme positioned in the metabolism between the two metabolites is inhibited by H_2O_2. Interestingly, such an enzyme does indeed exist: the ω-amidase/NIT2 catalyzes the conversion of KGM to α-ketoglutarate. Thus, extracellular H_2O_2 at a concentration of 300 µM potentially (temporarily) inactivates the enzyme leading to an accumulation of KGM. Our hypothesis is shown in **Fig. 22**.

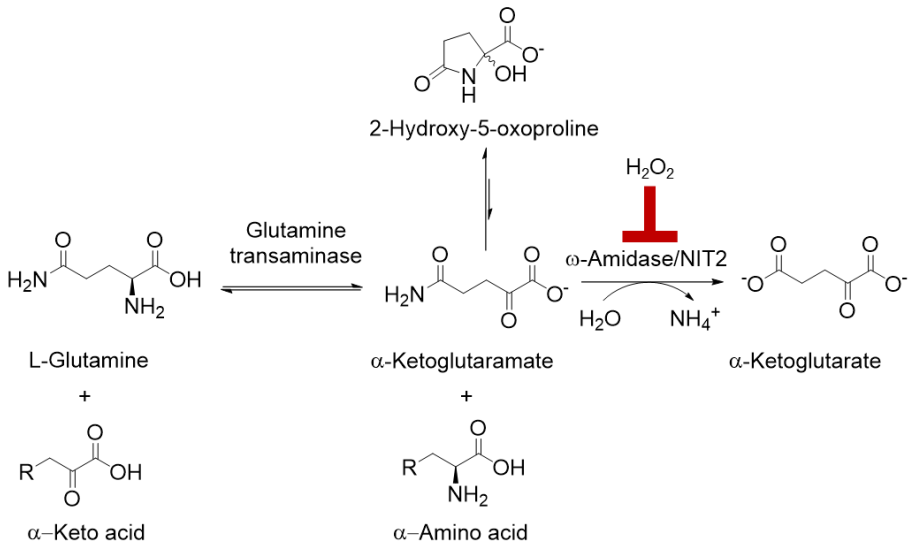

Figure 22. The ω-amidase/NIT2 is potentially inhibited by 300 µM H_2O_2
The glutaminase II pathway: L-glutamine is transaminated to α-ketoglutaramate (KGM). KGM is hydrolyzed to α-ketoglutarate and ammonia by the ω-amidase/NIT2. Our data indicate that NIT2 is susceptible to temporary inhibition by oxidation

4.3 Redox-sensitivity of ω-amidase/NIT2

4.3.1 BIAM switch assay shows redox-sensitivity of ω-amidase/NIT2

As H_2O_2 results in transient accumulation of the substrate of NIT2, reversible oxidation of a cysteine residue should be considered as a likely mechanism of transient inactivation. Human NIT2 contains 276 amino acids including seven cysteines with one of them located in the active center. In order to verify our hypothesis that NIT2 is redox-sensitive an affinity pulldown for oxidized proteins was performed as previously described [162]. Briefly, HUVECs were exposed to 300 µM H_2O_2 or basal medium for 15 min, subsequently free thiols were blocked with NEM, then reversibly oxidized thiols were reduced with DTT and nascent free thiols were labeled with EZ-Link iodoactely-PEG2-Biotin (BIAM). BIAM labeled proteins were precipitated with streptavidin coupled beads. A scheme of the BIAM-switch assay is shown in **Fig. 23A**.

Significantly more oxidized NIT2 was pulled down in comparison to HUVECs treated with basal medium (**Fig. 23B**). This finding suggests that NIT2 can be reversibly oxidized by 300 µM H_2O_2. In order to address whether this effect also occurs under pathophysiological conditions, HUVECs were co-cultured with human leukocytes, which were then stimulated with opsonized zymosan to increase their ROS formation. Subsequently, the leukocytes were removed and endothelial NIT2 oxidation was

determined. Similar to the finding noted for H_2O_2 exposure, this resulted in cysteine oxidation of NIT2 (**Fig. 23C&D**).

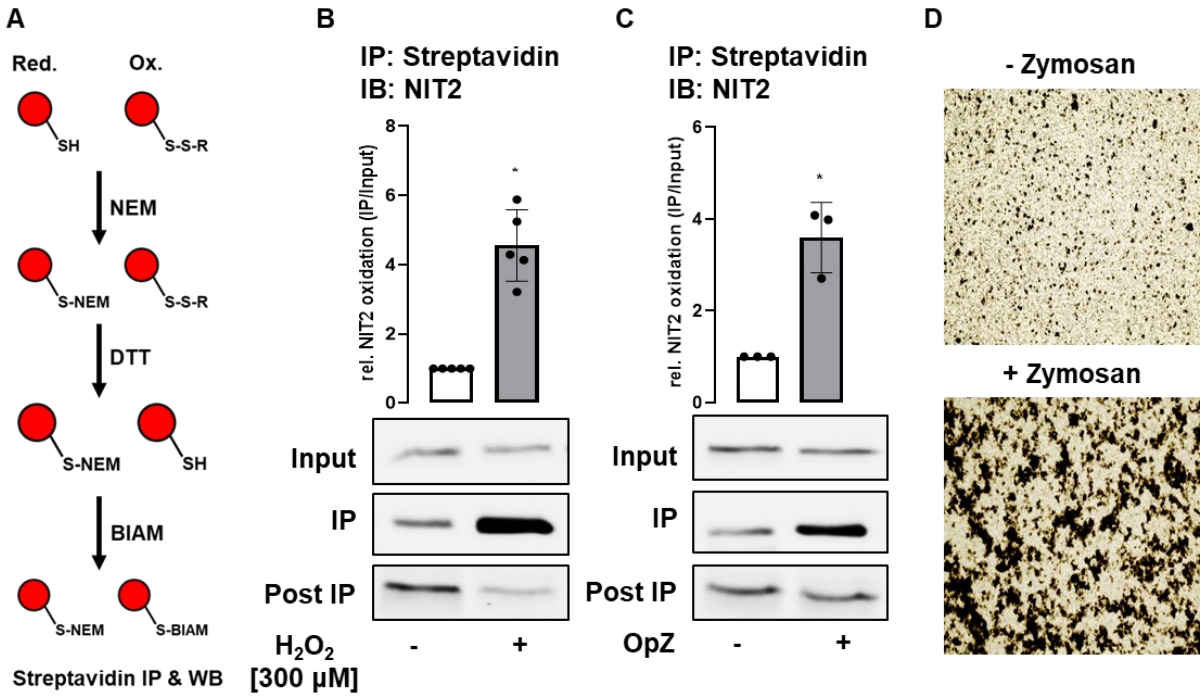

Figure 23. BIAM switch assay shows redox-sensitivity of NIT2
(**A**) Workflow of the BIAM switch assay. (**B**) Western blot of NIT2 after streptavidin IP following the BIAM protocol for HUVECs exposed to H_2O_2 or basal medium. * indicates $p<0.05$; n=5. (**C**) Western blot of NIT2 after streptavidin IP following the BIAM protocol. HUVECs were exposed to freshly isolated neutrophil granulocytes that were either activated with opsonized zymosan (OpZ) or left unstimulated. * indicates $p<0.05$; n=3. (**D**) Image of freshly isolated neutrophil granulocytes covering HUVECs.

Based on these findings, we were interested in determining the resistance of NIT2 towards the exposure to H_2O_2. Therefore, we performed the BIAM switch assay with an H_2O_2 gradient. Interestingly, it requires at least 300 µM H_2O_2 to oxidize the protein. At this concentration, hyperxidation of peroxiredoxins (Prx-SO_3) occurs indicating that high concentrations of ROS are necessary to oxidize the protein (**Fig. 24**).

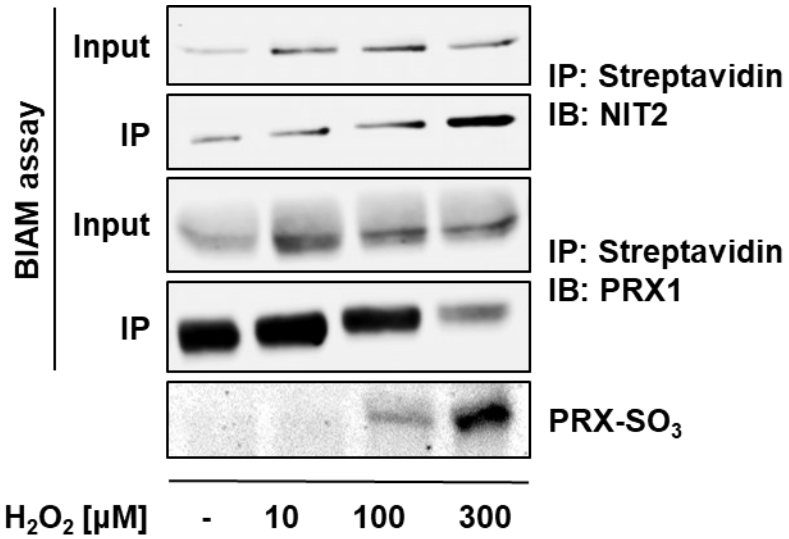

Figure 24. High concentrations of H_2O_2 are necessary to oxidize NIT2
Western blot after BIAM-switch assay and western blot under non-reducing (-DTT) conditions of HUVECs exposed to different concentrations of H_2O_2 (as indicated).

4.3.2 Cys146 and Cys153 in NIT2 are susceptible to oxidation by H_2O_2

As the BIAM switch assay clearly showed the redox-sensitivity of NIT2, the next step was to identify the cysteines in NIT2 that are potentially oxidized by H_2O_2 using redox-proteomics. Therefore, a pMCV6 NIT2-10X His Tag construct was overexpressed in HEK293 cells. This is necessary, because analysis of the immunoprecipitation of endogenous NIT2 yields low sequence coverage in the mass spectrometry (MS). HEK293 cells were exposed to 300 µM H_2O_2 (in basal medium) or to media for 15 min. Subsequently, free thiols were blocked with NEM, the protein was purified by HisTrap columns and loaded onto a non-reducing SDS page gel. The gel bands were analyzed by MS. For analysis, spectral counting for oxidized cysteine residues (carbamidomethylation, di- and trioxidation) and NEM-labeled cysteines was performed. The workflow is shown in **Fig. 25A**.

Among the seven cysteine residues of NIT2, five (Cys76, Cys97, Cys146, Cys153 and Cys170) showed an increase in oxidation (oxidized cysteine vs. NEM-labelled cysteine) after exposure to 300 µM H_2O_2. Unexpectedly, all cysteines showed noticeable high basal oxidation. Furthermore, the results of a recently published machine learning algorithm, that predicts redox-sensitive cysteine residues, pinpointed Cys146 in human NIT2 (Cys186 in mouse NIT2 (mNIT2)) as a potential target for oxidation (**Table 22**). The algorithm investigates the influence of different structural and

sequence features on the modifiability of a cysteine residue and ranks them according to the possibility to be potentially oxidized [175]. Therefore, further analysis focused on Cys146 and Cys153 of NIT2 (**Fig. 25B**). Cys153 is part of the active center and necessary for proper functioning of the enzyme making it a reasonable target for inhibition by oxidation. In comparison, Cys146 is part of a hydrophobic pocket without any further contact sites and not nearby the active center (**Fig. 25C**).

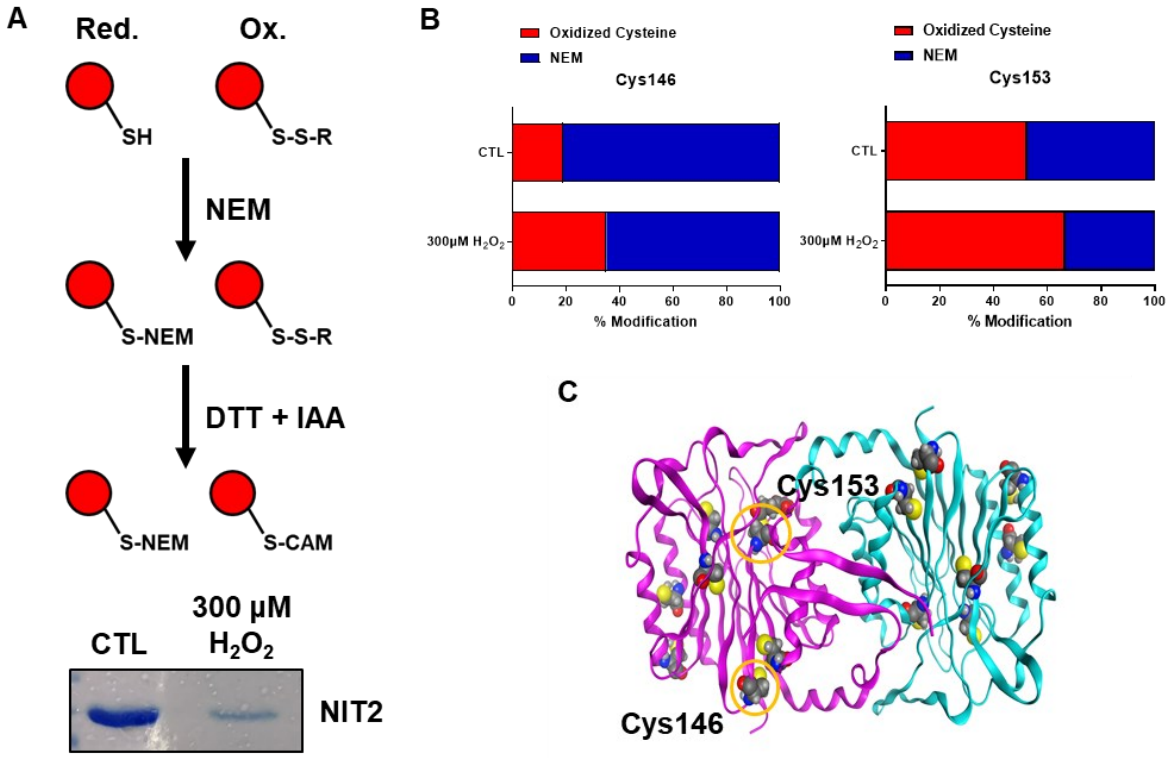

Figure 25. Redox-proteomics reveals Cys146 and Cys153 as potentially oxidized in NIT2
(**A**) Workflow to identify redox-sensitive cysteine residues in NIT2 by MS. (**B**) Identified oxidized cysteines in human NIT2 obtained from MS. (**C**) Structural model of the human NIT2 dimer protein highlighting the location of Cys146 and Cys153. Figure **25C** was provided by Prof. Dr. Eugen Proschak, Pharmaceutical Institute, Goethe-University Frankfurt/Main, Germany.

Table 22. Machine learning approach to predict potentially oxidized cysteine residues in mNIT2
Protein name, cysteine position and prediction score (from 0 – 1) of a list of cysteine residues in mNIT2. Higher scoring cysteine residues are more likely to be redox-sensitive according to [175].

Protein Name	Cysteine Position	Prediction
Omega-amidase NIT2	63 (44 hNIT2)	0.276767
Omega-amidase NIT2	82 (76 hNIT2)	0.2952
Omega-amidase NIT2	135 (97 hNIT2)	0.245933
Omega-amidase NIT2	184 (146 hNIT2)	0.392433
Omega-amidase NIT2	191 (153 hNIT2)	0.202767
Omega-amidase NIT2	208 (170 hNIT2)	0.3057

4.3.3 Characterization of NIT2 cysteine mutants

For further characterization, Cys146 and Cys153 were mutated to different amino acids in an overexpression plasmid and expressed in HEK293 cells (**Fig. 26A**). Cys153 was replaced with a serine while three different mutation strategies for Cys146 were applied: C146A, C146D and C146S. The aspartate and serine mutant were unstable and could not be purified by His-Tag affinity purification. Both amino acids were thought to introduce either a negative charge (aspartate) or an increased electronegativity (serine) into the hydrophobic pocket of Cys146. Aspartate is intended to act as a "cysteine sulfonic acid mimic", increasing the magnitude of the negative charge of the oxidized cysteine residue. Purity of the protein preparation is shown in **Fig. 26B**.

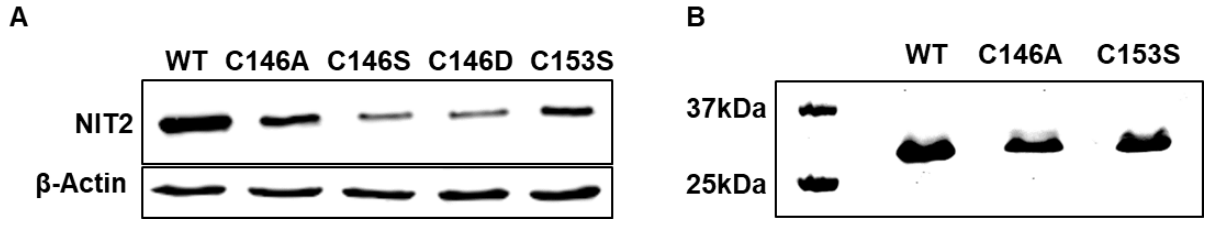

Figure 26. Mutation of Cys146 affects protein stability
(**A**) Western blot of different NIT2 mutants overexpressed in HEK293 cells. (**B**) Scanned Coomassie gel of purified human NIT2 protein after His-Tag affinity purification.

To test the activity of the NIT2 mutants, a photometric activity assay was established as previously described [159]. The assay uses succinamate rather than KGM for the hydroxaminolysis reaction. The underlying ping-pong mechanism of the reaction is shown in **Fig. 27**. Succinyl hydroxamate yields a stable brown color in the presence of acidic ferric chloride which can be quantitated spectrophotometrically at 535 nm.

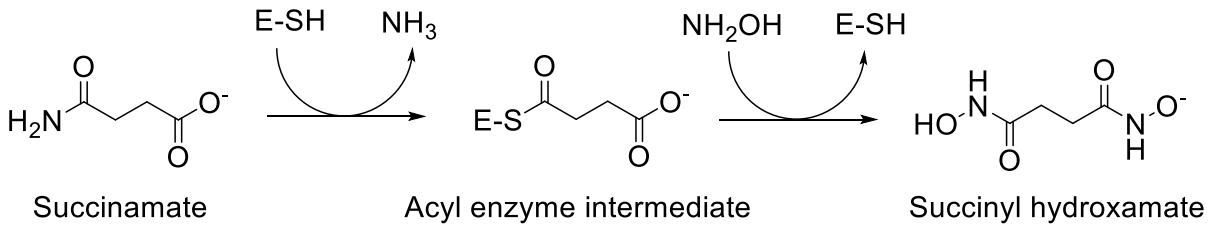

Figure 27. Ping-pong mechanism for the hydroxaminolysis of succinamate
In the first step, the succinamate reacts covalently with the active site cysteine to generate an acyl-enzyme intermediate (thioester) and ammonia. In the second step, a nucleophilic attack of hydroxylamine generates succinyl hydroxamate and the active site cysteine is regenerated. Figure adapted from Krasnikov *et al.* (2009) [159].

First, it was investigated whether H_2O_2 impacts on NIT2 activity by using the established activity assay. Pre-incubation of purified NIT2 with two different concentrations (100 µM and 300 µM) of H_2O_2 significantly reduced the relative activity of the protein indicating that H_2O_2 affects NIT2 functionality. As expected, the active center mutant (C153S) showed no activity (**Fig. 28A**). Next, we were interested whether the mutation of Cys146, which was identified to be differentially oxidized by H_2O_2, affects NIT2 activity. A significantly reduced relative activity of NIT2 C146A was noted in comparison to the WT protein (**Fig. 28B**). As protein activity is linked to stability, a thermal shift assay was performed to determine the melting points of NIT2 and NIT2 C146A. The NIT2 C146A mutant had a reduced melting point (~2°C) indicating that the C146A mutant was less stable than the WT protein (**Fig. 28C/D**).

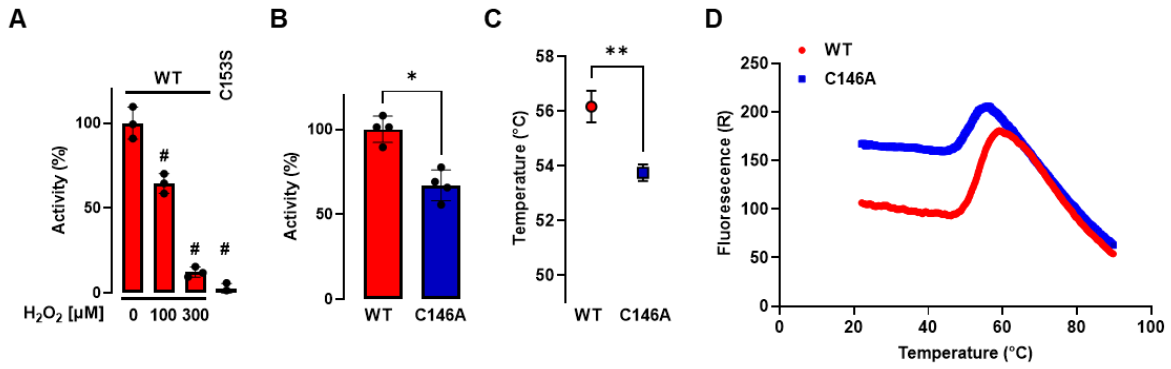

Figure 28. Mutation of Cys146 affects activity and stability of NIT2
(**A**) Activity assay of purified NIT2 protein (12.5 µg) including pre-incubation for 15 min at 37°C with different H_2O_2 concentrations as indicated. n=3; # indicating $p<0.05$ compared to 0 µM H_2O_2. (**B**) Activity assay of purified NIT2 and NIT2 C146A protein (12.5 µg) in the absence of H_2O_2. n=4; * indicating $p<0.05$ (**C**) Melting points of NIT2 and NIT2 C146A as determined by thermal shift assay. n=3; ** indicating $p<0.01$. (**D**) Melting curve (median) of purified NIT2 and NIT2 C146A protein. The thermal shift assay was performed together with Dr. Steffen Brunst, Pharmaceutical Institute, Goethe-University Frankfurt/Main.

4.4 Deletion of ω-amidase/NIT2 affects endothelial function

4.4.1 CRISPR/Cas9 knockout of glutaminase II pathway enzymes in HUVECs

To study the metabolic and physiological importance of the glutaminase II pathway in HUVECs, stable knockout cells were established by a lentiviral CRISPR/Cas9 approach. After delivering the bacterial Cas9 nuclease complexed with a synthetic guide RNA (gRNA) into a cell, the host cell´s genome is cut by the Cas9 at a desired location. The gRNAs were designed in a way that they will introduce a double strand break into an exon of the target gene. This can cause a frameshift mutation in the coding sequence of the target protein [154].

Knockouts of NIT2 and both glutamine transaminases (GTK/KYAT1 and GTL/KYAT3) were generated. Additionally, a GLS1 as well as GLS1/NIT2 knockout cell line were developed. This allows differentiation between the glutaminase I (glutamine → glutamate → α-ketoglutarate) and the glutaminase II (glutamine → α-ketoglutaramate → α-ketoglutarate) pathway in HUVECs. The knockout efficiency was shown by western blot analysis. A guide RNA that contains no genomic target sequence (non target control, NTC1) served as a control for all experiments (**Fig. 29**).

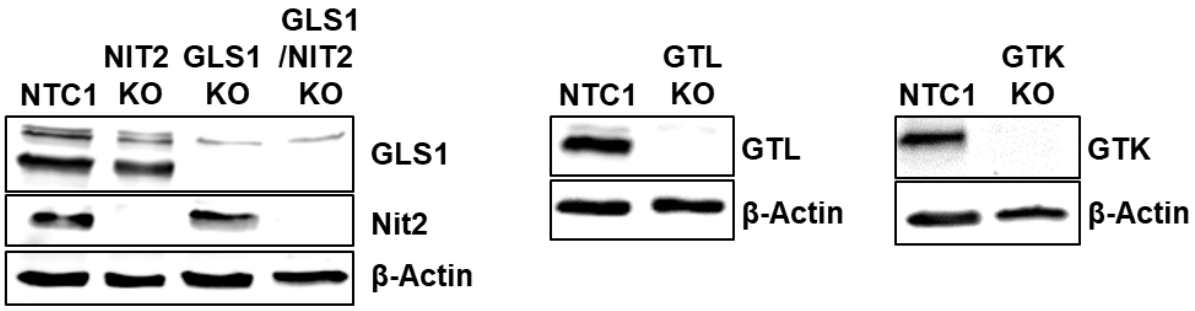

Figure 29. CRISPR/Cas9 mediated knockout of key enzymes of glutamine metabolism in HUVECs
Immunoblotting for NIT2, GLS1, GTK/KYAT1, GTL/KYAT3 and β-actin.

4.4.2 NIT2 knockout affects proliferation but not migration of HUVECs

Interfering with glutamine metabolism has been shown to affect endothelial function as glutamine feeds the TCA cycle with anaplerotic carbons required for synthesis of biomass [91,92].

Inhibition of GLS1 has been shown to decrease proliferation of HUVECs. Therefore it was investigated whether a knockout of NIT2 affects cell proliferation. In line with previous reports [92], pharmacological inhibition of GLS1 significantly reduced proliferation. Furthermore, HUVECs that lack NIT2 proliferated significantly slower than control cells. This effect was further enhanced with pharmacological inhibition of GLS1 using the selective, allosteric GLS1 inhibitor Bis-2-(5-phenylacetamido-1,3,4-thiadiazol-2-yl)ethyl sulfide (BPTES, 3 µM) [186] (**Fig. 30A**). Different results were obtained in the scratch-wound assay. There, a knockout of NIT2 did not affect migration of HUVECs (**Fig. 30B**). This finding is in line with the previously shown glutamine independency of endothelial cell migration [92].

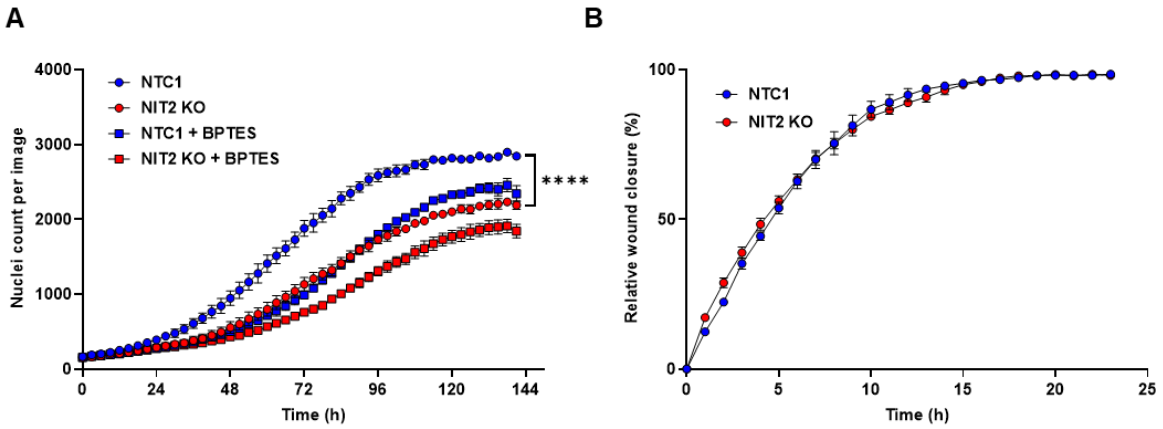

Figure 30. Knockout of NIT2 affects proliferation but not migration of HUVECs
(**A**) Growth curve of NTC1 or NIT2 KO HUVECs treated with or without 3 µM of the selective GLS1 inhibitor BPTES. n=3; **** indicates p<0.0001. (**B**) Migration of NTC1 or NIT2 KO HUVECs by the scratch wound assay. n=3.

4.4.3 Deletion of NIT2 reduces angiogenic sprouting of ECs

Deletion of GLS1 reduces angiogenic sprouting *in vivo* and *in vitro* [91,92]. Therefore, the *in vitro* effect of a loss of NIT2 on endothelial cell behavior was analyzed by the spheroid outgrowth assay. Deletion of NIT2 significantly reduces the number of sprouts (**Fig. 31A**) and the accumulative sprout length (**Fig. 31B**) in comparison to the control cells. The same effect was observed after stimulation with the pro-angiogenic signal protein VEGF. Interestingly, loss of NIT2 impaired endothelial cell sprouting in a similar way as does the genetic deletion of GLS1. In contrast, a double knockout of NIT2 and GLS1 did not further enhance this effect. A representative picture of the spheroids is shown in **Fig. 31C**.

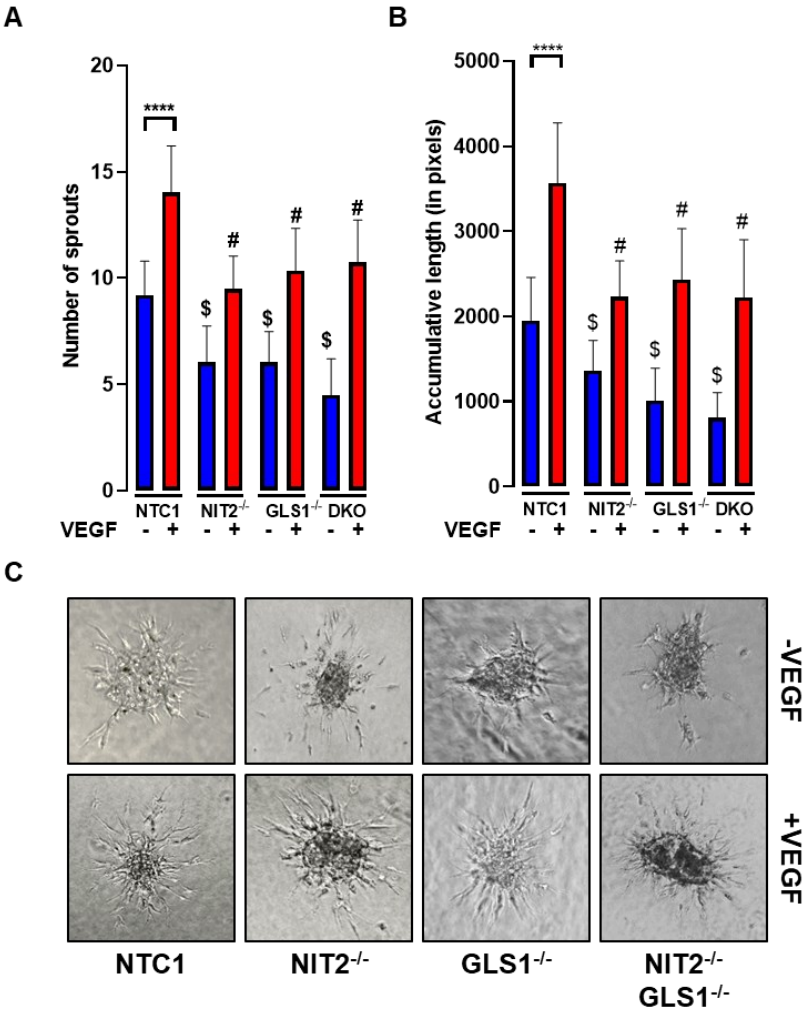

Figure 31. Knockout of NIT2 impairs angiogenic sprouting
Spheroid outgrowth assay (**A**) quantification of sprout number (**B**) quantification of accumulative sprout length and (**C**) images. $ *vs.* NTC1 (-VEGF) $p<0.05$; #: *vs.* NTC1 (+VEGF) $p<0.05$. One-Way-ANOVA. **** indicates $p<0.0001$. DKO=NIT2/GLS1 double knockout.

4.5 Metabolic importance of the glutaminase II pathway in HUVECs

4.5.1 Detection of KGM by targeted metabolomics

α-Ketoglutaramate (KGM), the main intermediate of the glutaminase II pathway, is commercially not available and prior to 2020 could only be synthesized by incubating L-glutamine with L-amino acid oxidase in the presence of catalase [142]. Travis T. Denton, PhD and colleagues (Washington State University, WA, USA) successfully synthesized the compound in 2020 using a non-enzymatic procedure [118]. The linear open chain form of KGM cyclizes to a stable lactam form (2-hydroxy-5-oxoproline, 145.11 g/mole). At neutral pH the equilibrium favors lactam (99.7%) over the open chain form (substrate of NIT2, 0.3%) [112]. We used the compound provided by the Denton laboratory to generate an internal standard for targeted analysis by mass spectrometry. The spectrum shows a peak at 144 Da (negative mode) and three major peaks at 126.0 Da (M-1-H_2O; -18 Da), 82.0 Da (M-1-CO_2-H_2O; -62 Da) and 42.0 Da (a CNO^- fragment), respectively (**Fig. 32A**). A similar fragmentation of KGM was shown in isobutane chemical ionization [187]. The spectrum clearly shows the lactam form of KGM. After establishing the internal KGM standard, we detected KGM in HUVECs. Interestingly, we could only detect the lactam form of KGM in NIT2 KO cells where the compound accumulates (**Fig. 32B**). It seems likely that under cell culture conditions the compound is directly and very efficiently hydrolyzed to α-ketoglutarate.

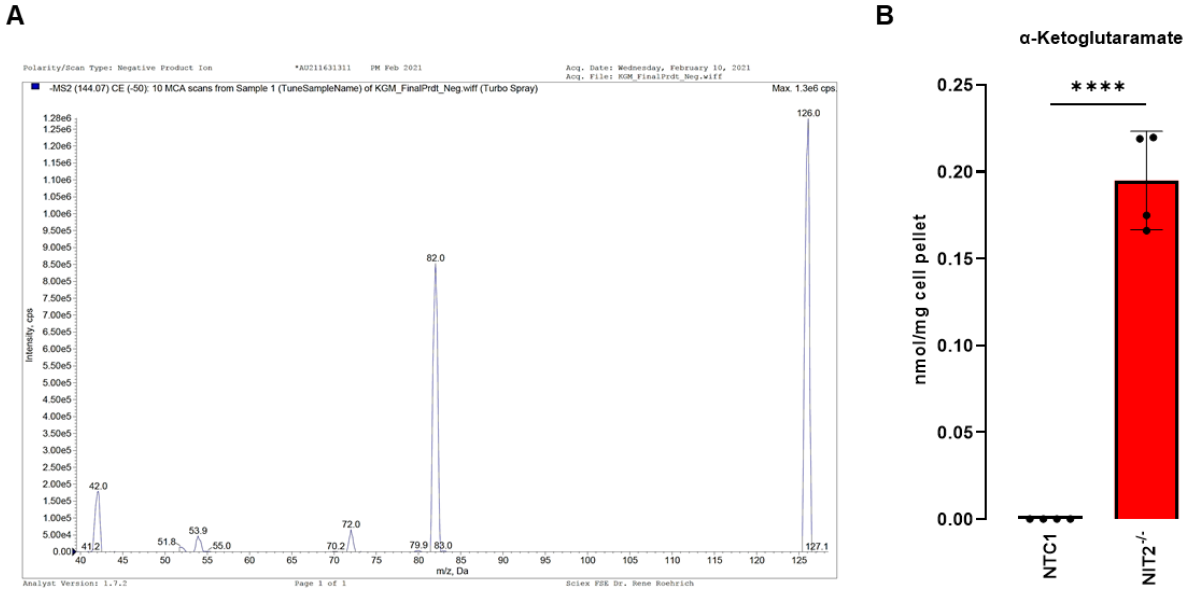

Figure 32. α-Ketoglutaramate is only detectable in NIT2 knockout cells
(**A**) The MS spectrum of KGM in negative ionization mode (**B**) Detection of KGM in HUVECs by targeted LC/MS. **** indicates p<0.0001; Paired t-test; n=4. The KGM was provided by Prof. Dr. Travis T. Denton, Washington State University, Spokane, USA

4.5.2 HUVECs lacking NIT2 have reduced α-ketoglutarate levels

After establishing a targeted approach to detect KGM in HUVECs, we quantitatively measured glutamine, glutamate and α-ketoglutarate levels by LC/MS. Loss of GLS1 is accompanied by a 3-fold increase in glutamine. Double knockout of GLS1 and NIT2 significantly reduced glutamine levels. As expected, glutamate and α-ketoglutarate levels were significantly reduced in the GLS1 knockout. Importantly, α-ketoglutarate levels were significantly decreased in the NIT2 knockout indicating the biochemical relevance of the glutaminase II pathway for intracellular α-ketoglutarate levels (**Fig. 33**).

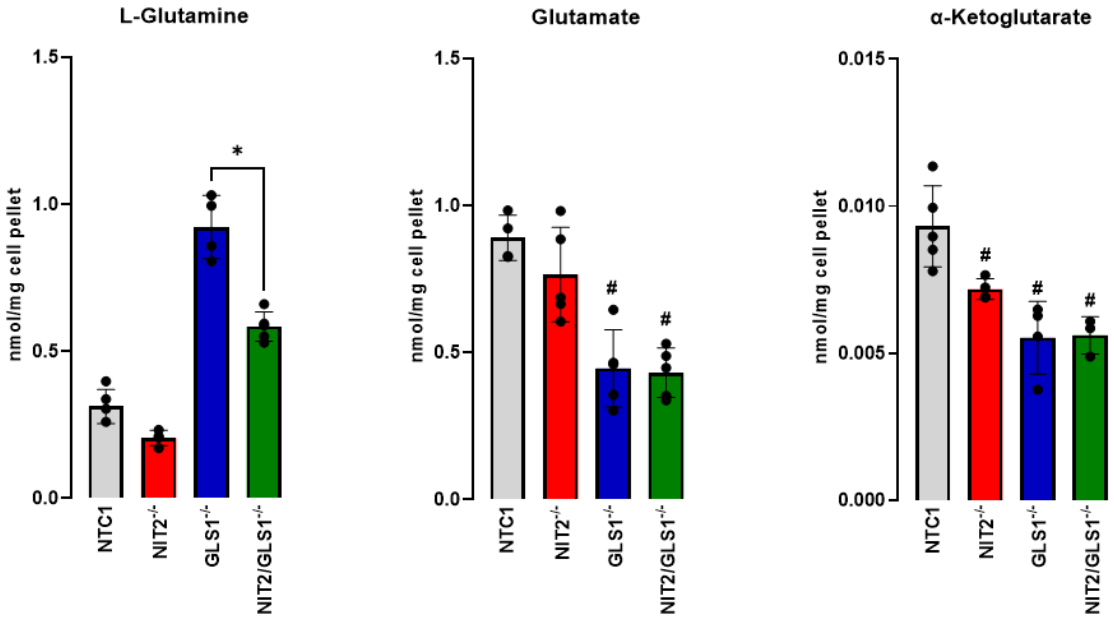

Figure 33. Deletion of NIT2 reduces α-ketoglutarate levels in HUVECs
Quantitative analysis of intracellular glutamine, glutamate and α-ketoglutarate levels by targeted LC/MS. n=3-5; * indicates $p<0.05$; # *vs.* NTC1 $p<0.05$; Paired t-test.

There is evidence that the glutaminase II pathway is linked to the methionine salvage pathway [103]. In the last step, the pathway is closed by transamination of α-keto-γ-methylthiobutyrate (synonym: 2-oxo-4-methylthiobutyric acid, KMBA) to methionine with a suitable amino acid. Therefore, it was investigated whether knockout of the glutamine transaminases has an effect on methionine levels. Essentially, a double-knockout of both glutamine transaminases significantly reduced methionine levels. With this, the corresponding α-keto acid of methionine, KMBA, became detectable (**Fig. 34**).

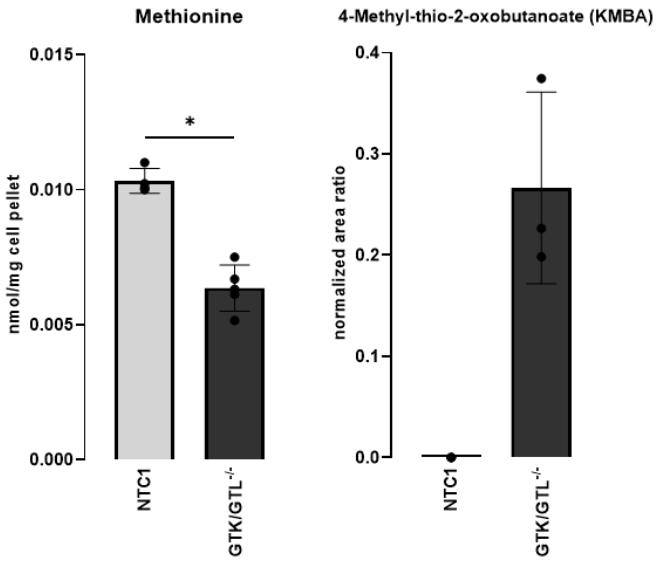

Figure 34. Knockout of the glutamine transaminases reduces methionine levels in HUVECs and increases its α-keto acid analogue (KMBA)
Quantitative analysis of intracellular methionine and KMBA levels by targeted LC/MS. * indicates $p<0.05$. n=3-5.

4.4.3 α-Ketoglutaramate is detectable in human plasma and serum samples

Having established a reliable method to detect KGM by targeted metabolomics, we investigated how stable the compound is in plasma and serum samples of healthy volunteers. Furthermore, it was analyzed whether KGM levels are changed after food intake. Seven healthy co-workers of our institute participated. Blood was taken from the volunteers in the morning on empty stomach. Subsequently, everyone had breakfast from the same buffet. Again, blood was taken after food intake for the times indicated and analyzed by targeted LC/MS.

KGM appears to be very stable in both EDTA plasma and serum, even if the sample was left at room temperature for 6 h (**Fig. 35A**). Therefore, KGM levels can be reliably determined in the samples that were not directly processed (e.g. directly coming from the clinics). Interestingly, the KGM levels in blood serum are higher in comparison to the EDTA plasma. Furthermore, food intake increased KGM levels in both plasma and serum samples already one hour after eating (**Fig. 35B**). The findings are consistent with previous publications showing the presence of KGM in rat blood [142], human cerebrospinal fluid (CSF) [188] and human blood [189].

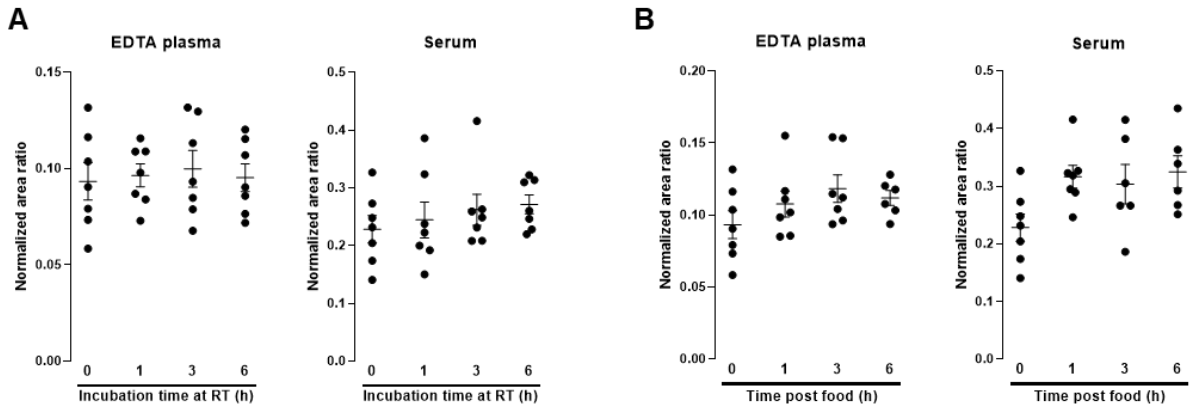

Figure 35. KGM levels of healthy volunteers
(**A**) KGM levels of EDTA plasma and serum samples of healthy volunteers. Samples were incubated at room temperature (RT) for the time indicated. (**B**) KGM levels of EDTA plasma and serum samples of healthy volunteers before and after food intake.

4.4.4 NIT2 knockout mouse

To evaluate the importance of NIT2 in an *in vivo* model, it was decided to generate a inducible NIT2 knockout mouse. Currently there is no NIT2 knockout mouse line available. To address this, two loxP sites flanking exon 2 of NIT2 were inserted into a mouse genome by the means of CRISPR/Cas9. This allows deletion of exon 2 after recombination using a Cre-recombinase. Thereby, a cell-type specific recombination can be achieved (e.g. crossing with Cdh5Cre mice). In the course of the genotyping of the mouse it was realized that some animals carried a complete loss of exon 2 of NIT2 (global knockout), rather than the insertion of the loxP site. To test the knockout efficacy, the expression of the enzyme in aortic ECs, aortic smooth muscle cells (SMC), liver, lung and kidney tissue was analyzed by western blot. The enzyme is well expressed in liver and kidney while the lung showed much lower expression. The NIT2 global knockout mice showed no expression of NIT2 (**Fig. 36**).

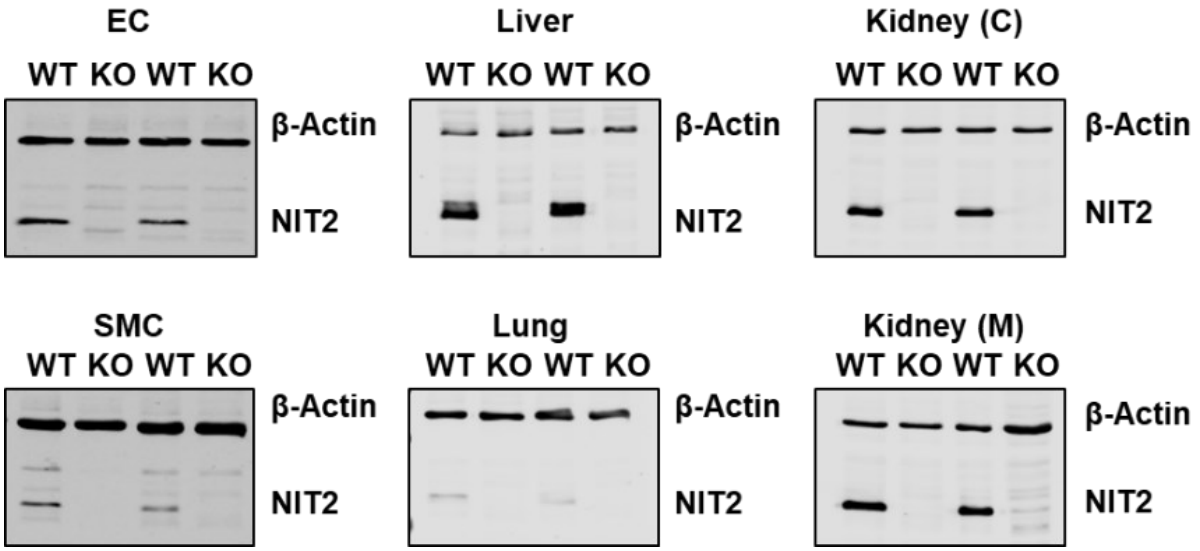

Figure 36. Successful knockout of NIT2 in mice
Western blot for NIT2 and β-actin of cells or tissue as indicated (30 µg of protein). n = 2; C = cortex; M = medulla. EC, aortic endothelial cells; SMC, aortic smooth muscle cells.

4.5 NIT2 interacts with key enzymes of glutamine metabolism

4.5.1 BioID2 approach to identify NIT2 interaction partners

The ω-amidase/NIT2 has not been studied extensively and its interaction partners are completely unknown. Therefore, the BioID approach was used to identify potential interaction partners and their subcellular localization. The method uses a biotin ligase, namely BioID2 (improved version of the original BioID), fused to the protein of interest [190]. After addition of biotin, proximate proteins are biotinylated at lysine residues and can be precipitated after cell lysis using streptavidin-coupled beads. Interaction partners can be identified by mass spectrometry (**Fig. 37**).

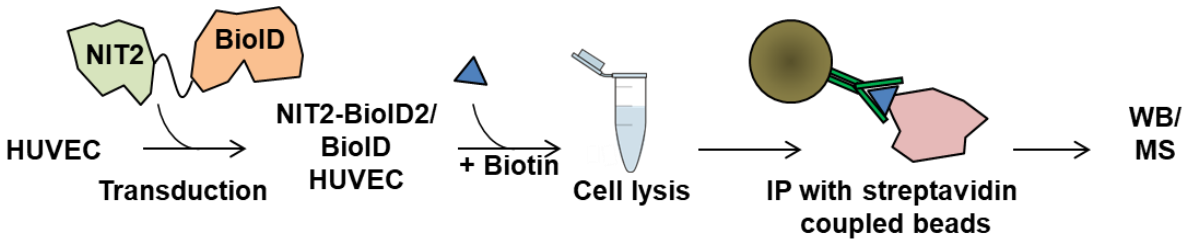

Figure 37. Workflow of the BioID2 approach to identify interaction partners
The protein of interest (e.g. NIT2) is fused to the biotin ligase (BioID2). The construct is overexpressed in HUVECs and after addition of biotin, biotinylated interaction partners can be identified by MS.

Two lentiviral overexpression plasmids under the control of the human EF1α promoter with puromycin selection were generated. HUVECs were infected with lentivirus to stably overexpress the BioID2 itself or the BioID2 fused to NIT2 (NIT2-BioID2). Overexpression of both constructs in HUVECs is shown by western blot analysis (**Fig. 38A**). Next, the functionality of the BioID2 as in a fusion protein was tested. For this, HUVECs were exposed to 50 µM biotin for 4 h. Subsequently, the cells were lysed and biotinylated proteins were precipitated by addition of streptavidin beads. Immunoblotting for streptavidin shows various proteins that were pulled-down by the specific ligase activity of the BioID2 (**Fig. 38B**).

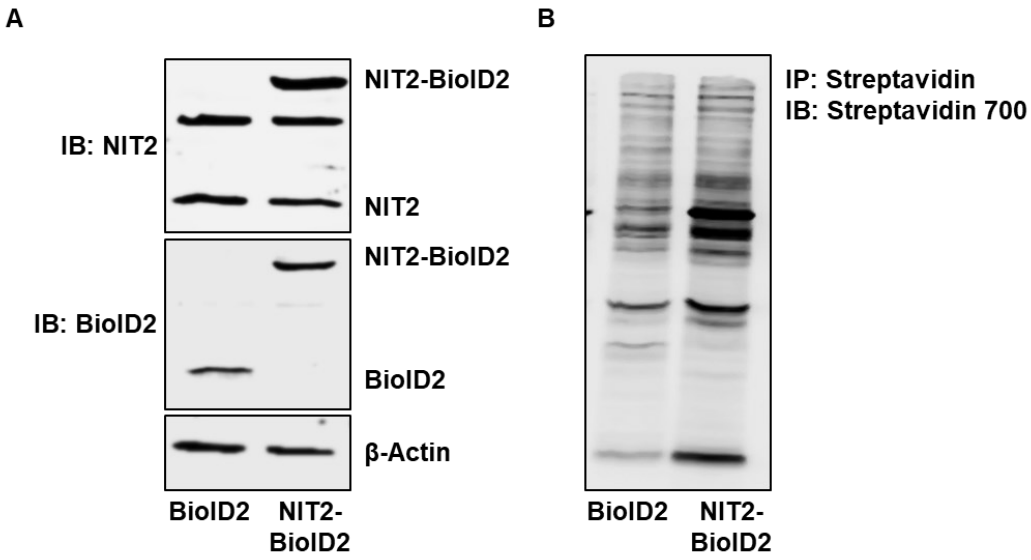

Figure 38. BioID2 as a tool to identify interaction partners of NIT2 in HUVECs
(**A**) Western blot for NIT2, BioID and β-actin. 30 µg of protein per lane (**B**) Immunoblot probed for streptavidin of streptavidin precipitation.

4.5.2 NIT2 interacts with HSPE1, GLUD1 and DLST

After establishing the BioID2 method, HUVECs were incubated with 50 µM biotin in full growth media for 4 h with subsequent cell lysis and streptavidin IP. The pull-downs were analyzed by targeted mass spectrometry.

40 significantly enriched proteins in NIT2-BioID2 over BioID2 were identified (**Table 24, Supplements**). The top three candidates (**Fig. 39**) were heat shock protein 10 (HSPE1), glutamate dehydrogenase (GLUD1) and the dihydrolipoyllysine succinyltransferase (DLST) component of the α-ketoglutarate dehydrogenase complex (αKGDHC). HSPE1 is a co-chaperonin and responsible for mitochondrial import of proteins together with HSP60 [191,192]. GLUD1 reversibly converts glutamate to α-ketoglutarate while DLST is part of the αKGDHC, which converts α-ketoglutarate into succinyl-CoA. Both proteins are located in the mitochondria [193,194].

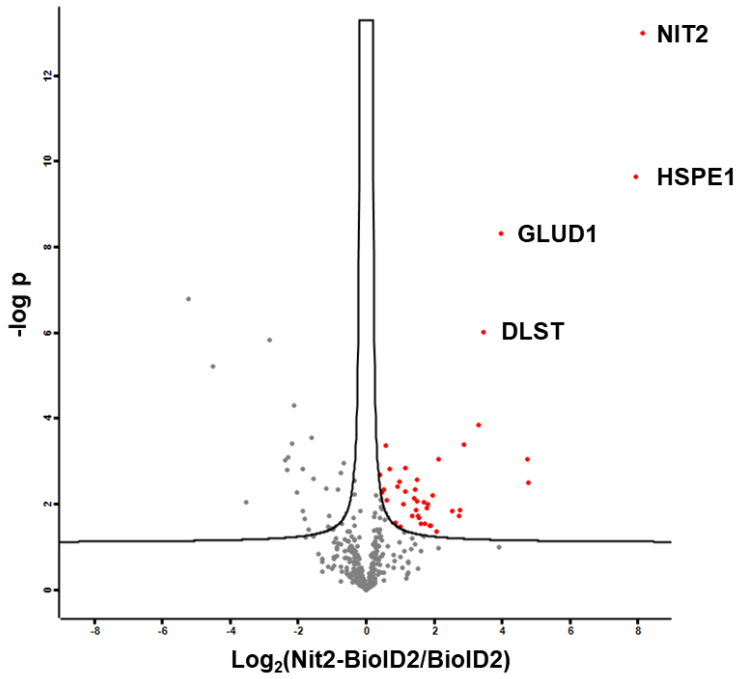

Figure 39. NIT2 interacts with key enzymes of mitochondrial glutamine metabolism
Volcano plot of mean fold change of biotinylated proteins (NIT2-BioID2 *vs.* BioID2). Positive ratio (red) indicates enrichment in NIT2-BioID2 sample. *P* value was calculated via the Student t-test. n=6.

4.5.3 Validation of NIT2 interaction partners

The interaction partners of NIT2 were validated by two different methods. First, a streptavidin precipitation followed by western blot analysis was performed. All three main interaction partners, HSPE1, GLUD1 and DLST, were enriched in the NIT2-BioID2 streptavidin IP as shown in **Fig. 40A**.

As the BioID2 method uses an overexpression system, the endogenous interaction of NIT2 and its partners was validated using the Duolink® assay. With this antibody-based method, a fluorescence probe visualizes two nearby proteins by an amplified signal that can be detected by laser scanning microscopy. Using proximity ligation assays, an interaction of endogenous NIT2 with HSPE1, GLUD1 and DLST was observed in HUVECs (**Fig. 40B**).

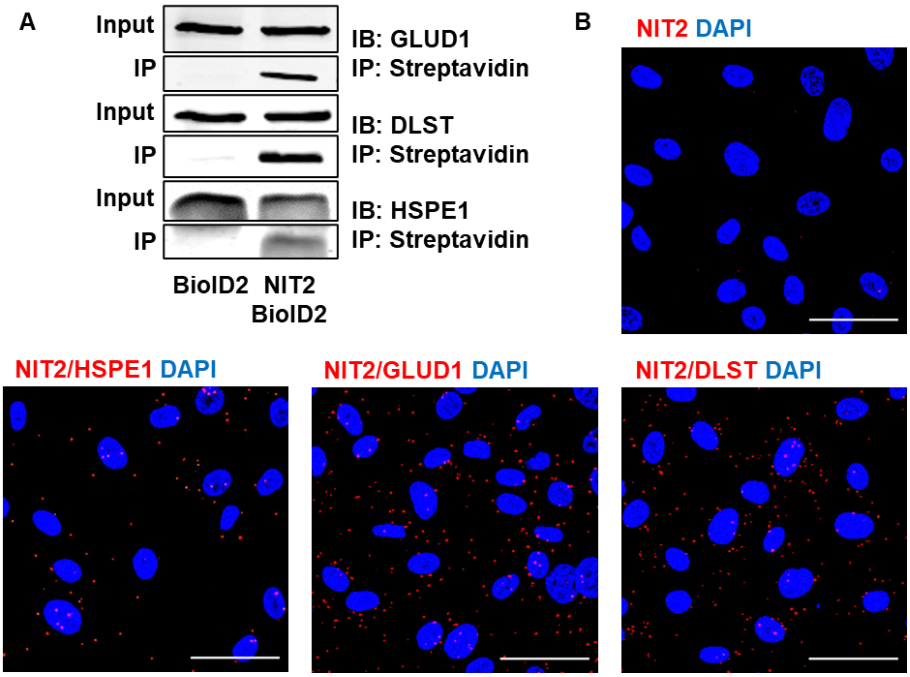

Figure 40. GLUD1, DLST and HSPE1 are specific interaction partners of NIT2
(**A**) HUVECs, either BioID2 or NIT2-BioID were grown with 50 µM biotin for 4 h. Whole-cell lysates were prepared and examined by immunoblotting for the indicated antibodies. (**B**) Proximity-ligation assay (PLA) for HSPE1, GLUD1 and DLST. NIT2 alone served as a negative control. Red dots indicate polymerase-amplified interaction signals. Scale bar indicates 20 µm.

4.5.4 NIT2 localizes in the cytoplasm and in the mitochondria

Interestingly, the main interaction partners of NIT2 are mitochondrial proteins. NIT2 was shown to be present in both the cytoplasm and mitochondria but how the enzyme is imported into mitochondria is unknown [103]. Immunofluorescence (IF) together with pre-staining of the mitochondria (mitoTracker) was used to identify the subcellular localization of NIT2 in HUVECs. IF shows co-staining between NIT2 and mitoTracker as well as staining in the nucleus and cytoplasm (**Fig. 41A**). The NIT2 KO HUVECs served as a control and showed only some unspecific staining in the nucleus. Furthermore, fractionation of HUVECs into cytoplasm and mitochondria shows abundance of NIT2 in both fractions (**Fig. 41B**). For further validation a previously published machine learning algorithm was applied to predict a potential mitochondrial targeting sequence (MTS) in NIT2 by comparing the protein sequence to proteins with experimentally verified targeting sequences [151]. The algorithm predicts a possible MTS (score: 17.33%) located at the N-terminus of NIT2 (**Fig. 41C**). This potential MTS could explain how NIT2 is imported into the mitochondria potentially delivering α-ketoglutarate directly to the TCA cycle. Nevertheless, expression of NIT2 in cytosol and mitochondria is consistent with the fact that expression of the glutamine transaminases occurs in both compartments.

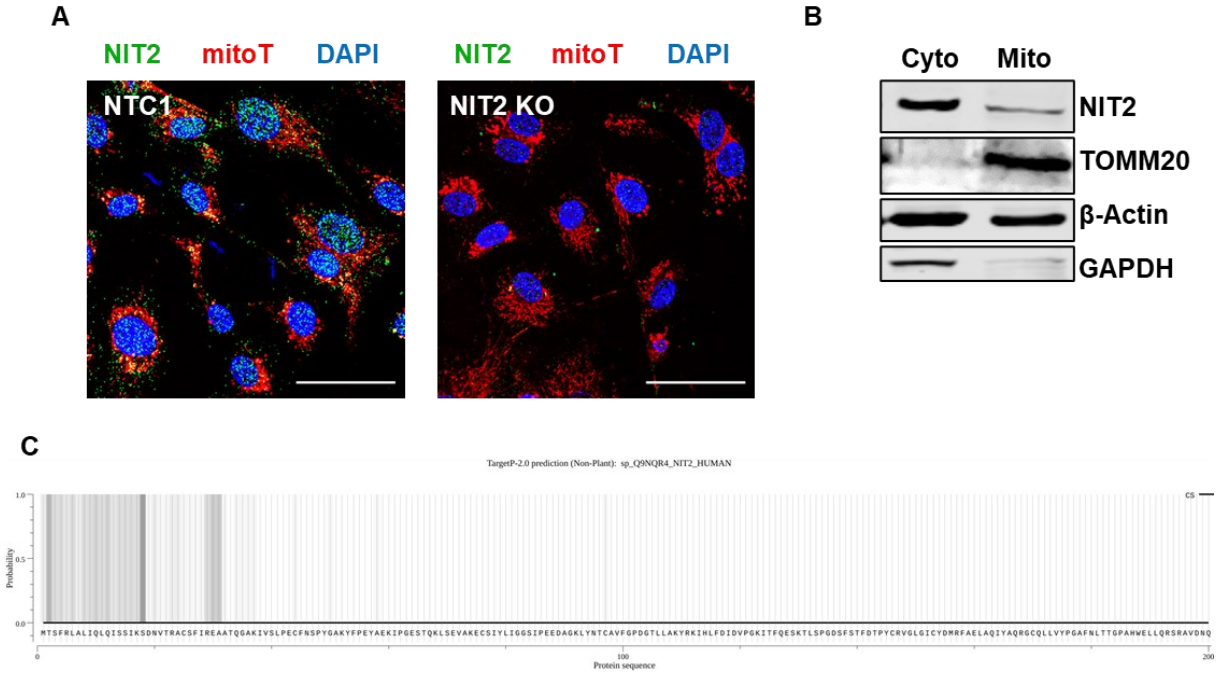

Figure 41. NIT2 localizes in both cytoplasm and mitochondria
(**A**) Immunofluorescence of HUVECs for NIT2. Mitochondria were stained using mitoTracker. Scale bar indicates 20 µm. (**B**) Immunoblot of cytosolic (cyto) and mitochondrial (mito) fractions of HUVECs lysate for the indicated antibodies. (**C**) Prediction of a mitochondrial target sequence (MTS) in NIT2 using a machine learning approach as previously published [151].

5. Discussion

5.1 Summary and significance of this work

Oxidative stress is thought to be a driver for several diseases. However, many data to support this concept were obtained by the addition of extracellular H_2O_2 to cells. This does not reflect the dynamics of intracellular redox modifications. Cells actively control their redox-state, and increased formation of ROS is a response to cellular stress situations such as chronic inflammation.

In this study, it was shown that different types of ROS lead to different metabolic and transcriptomic responses of HUVECs. While 300 µM extracellular H_2O_2 led to substantial metabolic and transcriptomic changes, the effects of DAO-derived H_2O_2 and menadione were low to moderate, indicating that the source and the concentration of ROS are important in eliciting changes in metabolism and gene expression.

Specifically, it was identified that acute increases in ROS transiently inactivate the enzyme ω-amidase/NIT2 of the glutaminase II pathway, which supplies cells with anaplerotic α-ketoglutarate. The pathway has not been studied systematically because, as noted above, the major intermediate, KGM, is not commercially available. In the present study, an internal standard for targeted detection of KGM in cells and blood plasma/serum was used. Deletion of NIT2 by CRISPR/Cas9 significantly reduced α-ketoglutarate levels in HUVECs and elevated KGM levels. It appears that in cell culture conditions, hydrolysis of KGM to α-ketoglutarate is very efficient. Knockout of the glutamine transaminases significantly reduced methionine, suggesting that the glutaminase II pathway is an important source of amino acid replenishment.

Similar to genetic silencing of GLS1 [91,92], HUVECs lacking NIT2 showed reduced proliferation and angiogenic sprouting. Furthermore, our results indicate that, at least in HUVECs, the enzyme also locates in the mitochondria where it interacts with key enzymes of glutamine/glutamate/α-ketoglutarate metabolism.

The data of the present work indicate that the glutaminase II pathway is an underappreciated, redox-sensitive pathway for glutamine utilization in HUVECs. Genetic deletion of NIT2 has considerable physiological effects highlighting the importance of glutamine for ECs.

5.2 DAO as a tool to study redox signaling

Currently the field of redox biology lacks tools for precise manipulation of the intracellular redox state. To overcome this problem and to generate intracellular H_2O_2, a chemogenetic approach with DAO was used. DAO contains a peroxisomal targeting sequence (PTS) but immunofluorescence showed that the enzyme, in an overexpression system, is distributed throughout the whole cell. Therefore, we did not genetically manipulate its subcellular localization. Interestingly, the DAO approach was used in an endothelial cell line (EA.hy926) to study how the enzyme targeted to different subcellular compartments modulates endothelial cell phosphorylation pathways. DAO-derived H_2O_2 mediates eNOS phosphorylation via AMPK activation when the enzyme is directed to the nucleus by an importing sequence. Cytosolic or caveolae-targeted DAO had no impact on eNOS phosphorylation [195]. In another study, this method was applied to induce severe cardiac dysfunction in the heart when overexpressed by adenovirus in mice [196].

The DAO approach has not yet been studied in an untargeted metabolomics and transcriptomics approach. In fact, there are only a few studies that describe the short-term and long-term metabolic effects of exposure to H_2O_2. In yeast and many human cell types, it was shown that inhibition of glycolytic enzymes by H_2O_2 leads to an accumulation of glycolytic intermediates that consequently induce an increased flux into the pentose phosphate pathway (PPP), through both the oxidative and non-oxidative branches [197–200]. This matches our findings and is compatible with the previously shown oxidative inhibition of GAPDH. Kuehne *et al.* [183] showed an upregulation of the PPP in human skin fibroblasts as a first line response after exposure to 500 µM H_2O_2. By using ultra-short ^{13}C labeling experiments, the authors provided evidence for multiple cycling of carbon backbones in the oxidative PPP, potentially maximizing NADPH reduction. Hence, NADPH is required as a reducing equivalent which maintains the active form of catalase and is a cofactor of TRX and GSH reductase [183,201]. Additionally, it has been shown that quiescent ECs, in a manner different from that of proliferating ECs, protect themselves against oxidative stress by increasing fatty acid oxidation up to three fold to generate NADPH via isocitrate dehydrogenase and malic enzyme [202]. It was quite surprising to observe that only H_2O_2 at high concentration induced most metabolic changes in HUVECs. Already 3 min after the addition of H_2O_2 significant changes in the antioxidant system

became apparent. A profound reduction in the GSH/GSSG ratio was observed after 10 min and this ratio was back to the basal situation after 270 min, pointing to a transient effect. H_2O_2 also reduced the relative concentration of isocitrate and other TCA cycle metabolites. The latter effect was also observed in menadione treated HUVECs and is known to be linked to an inhibition of aconitase via oxidation of an Fe−S cluster [185].

The changes in gene expression observed in HUVECs occurred in response to 300 µM H_2O_2 that activated, among others, the p53 pathway. It is accepted that low to moderate levels of ROS activate p53-related genes that increase the time needed for cell repair (e.g. cell cycle arrest and autophagy). With higher levels of ROS, p53 facilitates cellular stress and induced apoptosis to prevent aberrant cell proliferation [203]. All oxidative stimuli had a significant impact on ribosome-associated RNA. Both ribosomal RNA and ribosomal proteins can be chemically modified by ROS leading to a loss of their function. Ribosomal RNA (rRNA) is the structural and functional core of the ribosome and ROS can chemically modify the base and sugar moieties, generating a basic site and strand breaks. Among proteins of the translational machinery, the impact of oxidative stress on the ribosome, remains the least studied [204,205]. Due to its high cellular abundance, RNA is more frequently the target for oxidative damage in comparison to DNA [204].

Indeed, the data of the present study suggest that HUVECs upregulate ribosomal genes as a response to different redox stimuli. This implies that rRNA is a primary target for oxidative stress in ECs and this phenomenon has not been extensively studied in ECs and can be the subject to future research.

H_2O_2 had a stronger impact on gene expression and metabolism compared to menadione and DAO-derived H_2O_2. Thus, we analyzed the oxidation status of Prx enzymes. Only H_2O_2 at high concentrations induced an hyperoxidation of Prx (Prx-SO_3). Blocking thioredoxin reductases with auranofin did not induce the formation of Prx-SO_3 in D-alanine treated cells. This findings points to a high intracellular reducing capacity of ECs and the relevance of compartmentalized ROS production for signaling.

As shown herein, there is a substantial difference in the metabolic and transcriptomic response by ECs to extracellular H_2O_2 *vs.* intracellular H_2O_2. This is consistent with

increasing recognition of subcellular compartmentalization of redox processes. Except for the endoplasmic reticulum (ER), intracellular redox potentials are largely more reducing in comparison to the extracellular space. In particular, the extracellular milieu contains distinct amounts or types of reactive intermediates and available protein targets. Thiol-redox regulation of the extracellular space is associated with cellular signaling cascades. Indeed, the pathways that respond to ROS are essentially the extracellular signal-regulated kinases (ERK1/2), c-Jun NH2-terminal kinases (JNKs), and p38 kinase. The ERK family can be activated by growth factors as a response to oxidative stress. Vascular smooth muscle cells (VSMC) secrete cyclophilin A, a member of the immunophilin family, in response to oxidative stress which mediates ERK1/2 activation. The JNKs and p38 kinases are primarily involved in the cellular stress condition and are activated by extracellular H_2O_2 in smooth muscle cells [206,207].

In summary, only high concentrations (300 µM) of extracellular H_2O_2 induced significant changes in metabolic pathways of redox homeostasis, energy production and nucleotide synthesis. Likewise, high concentrations of H_2O_2 caused the major changes in gene expression and oxidation of peroxiredoxin enzymes. Collectively, these findings suggest that the source and the concentration of ROS are important to elicit changes in metabolism and gene expression. Our data indicate that ECs have sufficient intracellular reducing capacity to scavenge intracellularly produced H_2O_2. This is a possible explanation for the different effects of intracellular DAO-derived H_2O_2 and menadione-derived superoxide in comparison to high exogenous concentrations of H_2O_2.

Nevertheless, we anticipate that our chemogenetic approach will pave the way for a better understanding of the role of H_2O_2 in endothelial cell physiology. The knock-in DAO mouse line, which was developed during our studies, will allow precise and cell-specific generation of intracellular H_2O_2 *in vivo* and enhance our understanding of redox-signaling.

5.3 Redox-sensitivity of ω-amidase/NIT2

Exposure of HUVECs to menadione significantly decreased isocitrate levels. This is consistent with previously known inhibition of aconitase, an enzyme which converts citrate to isocitrate. The enzyme contains an iron sulfur cluster that is highly sensitive to superoxide [185]. Remarkably, the downstream metabolites, especially α-ketoglutarate, were not affected by menadione treatment. This can be explained by the fact that 70% of the TCA cycle carbons in HUVECs are derived from glutamine [92]. Superoxide anions at that concentration temporarily turn off the enzyme aconitase but the conversion of glutamine to α-ketoglutarate is not affected. Therefore, a collapse of the TCA cycle is not observable.

However, exposing HUVECs to 300 µM of extracellular H_2O_2 not only decreases isocitrate levels but also α-ketoglutarate and its downstream metabolites. Therefore, endothelial cell glutamine metabolism is directly affected. Glutamate dehydrogenase (GLUD1), that converts glutamate to α-ketoglutarate, is crucial for redox-homeostasis controlling intracellular α-ketoglutarate levels. The enzyme contains two reversibly oxidizable cysteines, which when oxidized, inhibit the enzyme to temporarily turn-off α-ketoglutarate production as a first-line response to oxidative stress [208,209]. Furthermore, α-ketoglutarate is susceptible to oxidative decarboxylation by H_2O_2 which yields succinate [210]. This is a possible explanation for unchanged relative succinate levels. Nevertheless, the decrease in α-ketoglutarate levels were also accompanied by an increase in KGM. This indicates that the ω-amidase/NIT2, which converts KGM to α-ketoglutarate, is susceptible to ROS-induced temporary inactivation and contributes to a depletion of α-ketoglutarate levels.

Given that H_2O_2 results in transient accumulation of the substrate of NIT2, reversible cysteine oxidation should be considered as the most likely mechanism of transient inactivation. Human NIT2 contains seven cysteines with one cysteine (Cys153) in the active center. As described above, several metabolic enzymes are susceptible to oxidation controlling the activity of the enzyme. Therefore, we first addressed the question of whether we can detect a potential oxidation of the enzyme using the BIAM-switch assay. The reducing step of the assay ensures that only proteins with reversibly oxidized cysteines are enriched in the streptavidin pulldown. Our data indicate reversible oxidation of endogenous NIT2 occurs in HUVECs after exposure to 300 µM

H_2O_2. At this concentration of H_2O_2, peroxiredoxins are hyperoxidized (-SO_3) and other proteins may become susceptible to oxidative modification. As peroxiredoxins are essential to maintain a reduced redox environment in cells, high ROS concentrations are essential for temporary oxidation of NIT2. To enhance the physiological relevance, we investigated whether NIT2 can be oxidized under pathophysiological conditions. For this, HUVECs were exposed to freshly isolated neutrophil granulocytes. Neutrophils generate various types of ROS including superoxide and peroxynitrite in response to soluble agonists (e.g. opsonized zymosan). This process is termed “oxidative burst” and is a key mechanism in immunological defense by helping to degrade bacteria or other pathogens [211]. Our results show that NIT2 is oxidized after incubation with granulocytes that were activated with opsonized zymosan. Therefore, NIT2 is potentially inhibited in disease conditions. Interestingly, one study showed a three- to tenfold increase in KGM, the substrate of NIT2, in the cerebrospinal fluid of humans with hepatic coma [188]. Furthermore, a remarkable increase in KGM has been reported in patients with primary hyperammonemia due to defects of the urea cycle [189,212]. It is now apparent that there is a neuroinflammatory response in hepatic encephalopathy [213]. This suggests an inhibition of NIT2 in the pathogenesis of a disease state and implications to KGM as a new biomarker. This is subject of future research as it is now possible to measure KGM by targeted LC/MS.

Using a targeted redox-proteomics approach, we identified reversibly oxidized cysteines in NIT2. In our experience, such an approach only works after overexpression of the target protein as the low protein yield after immunoprecipitation of the endogenous protein leads to insufficient sequence coverage. Therefore, a NIT2-10X His Tag construct was overexpressed in HEK293 cells with and without exposure to 300 µM H_2O_2 and subsequent N-ethylmaleimide alkylation to stabilize the redox-state of the protein. The protein was purified by affinity chromatography and cysteine modifications were analyzed by mass spectrometry. Overall oxidation of NIT2 by 300 µM H_2O_2 was only increased by 20%. On the other hand, the BIAM assay in HUVECs showed a 5-fold increase in oxidized endogenous NIT2 after exposure to 300 µM H_2O_2. HEK293 cells likely have a higher redox-capacity than do HUVECs and an overexpression is necessary to gain sufficient protein coverage. Therefore, differences in cysteine oxidation may occur limiting the comparability of both assays. Alternatively, purification of NIT2 in the presence of a reductant (DTT) and subsequent differential

oxidation of the purified protein by H_2O_2 should be considered. Whereas the first approach may help to identify the dynamics of endogenous thiol oxidation, the second approach has a superior sensitivity and is better suited to control background oxidation.

Our data suggest that five cysteines in human NIT2 are differentially oxidized by H_2O_2 (Cys44, Cys76, Cys97, Cys146 and Cys153). This was not expected as usually specific cysteine residues in a protein are susceptible to oxidation [214,215]. Therefore, we applied a machine-learning algorithm that considers the influence of different structural and sequence features regarding the modifiability of cysteines. This tool determines possible redox-sensitive cysteines based on the crystal structure of mouse NIT2 [175]. The results of this algorithm pointed to Cys146 as a possible redox-sensitive cysteine in human NIT2. To verify this, a model of the human NIT2 dimer based on the published mouse NIT2 crystal structure in the presence of the substrate was deduced. It is noticeable that Cys146 is part of a hydrophobic pocket without any further contact sites and not near to the active center. Interestingly, mutation of Cys146 to a negatively charged aspartate or a polar serine completely destabilized the protein. Purification at this point was not possible. Therefore, we replaced Cys146 with a non-polar amino acid (alanine). NIT2 C146A showed significantly reduced activity in comparison to the WT protein. Activity of NIT2 C146A was decreased to a similar extent as that noted for pre-incubation of NIT2-WT with 100 µM H_2O_2. As activity of an enzyme is linked to its stability, we also performed a thermal shift assay to determine the melting temperatures. NIT2 C146A exhibited a significantly lower melting temperature of ~2°C indicating that the protein is destabilized by the amino acid change. Our findings are in line with the concept that surface cysteines undergo oxidation to protect a cysteine in the active center from oxidation [216]. Unfortunately, it was not possible to purify NIT2 C146A after exposure to 300 µM (the protein is not stable) to investigate whether the active center cysteine becomes the primary target of oxidation in this particular mutation.

Secondly, our data also indicate that the active center cysteine (Cys153) is a potential target of reversible oxidation. Replacing this cysteine with a serine led to complete inactivation of NIT2. Therefore, Cys153 should be considered as a potential redox-sensitive cysteine. As previously mentioned these findings have to be validated with another experimental approach such as differential oxidation of the purified protein.

5.4 Physiological relevance of the glutaminase II pathway

Endothelial cells highly rely on glutamine as the majority of the TCA cycle carbons are derived from imported glutamine. Blocking of glutamine consumption, either pharmacologically or genetically, causes a collapse of the TCA cycle. Furthermore, glutamine is indispensable for endothelial cell proliferation and vessel function *in vivo* and *in vitro* [91,92]. Nevertheless, previous research highlighted only one side of glutamine metabolism in ECs, namely the glutaminase I pathway (i.e. Gln → Glu → αKG). Our data present another side.

We could demonstrate that the glutaminase II (i.e. Gln → KGM → αKG) pathway enzymes, the ω-amidase/NIT2 as well as both glutamine transaminases (KYAT1/GTK and KYAT3/GTL), are highly expressed in HUVECs. These findings indicate that the glutaminase II pathway may be highly active in HUVECs. To further evaluate the importance of the glutaminase II pathway, stable knockout HUVECs were generated by using the lentiviral CRISPR/Cas9 approach. In comparison to knock-downs (e.g. by siRNA transfection), this method allows a long-term knockout of the target protein with 100% efficiency.

Similar to knockdown of GLS1, knockout of NIT2 significantly decreases proliferation of HUVECs. This effect was further enhanced by simultaneous pharmacological inhibition of GLS1 by BPTES. On the other hand, ECs migration is not affected by the loss of NIT2. Together our findings demonstrate that the metabolic demands of proliferation and migration in ECs differ substantially. This is in line with the previously shown importance of glutamine for ECs proliferation while migration is completely dependent on glucose [91,92]. A possible explanation is that ECs generate ATP, which is essential for migration, via glycolysis while glutamine is required for biosynthetic processes. Essentially, during migration glycolytic enzymes occur in multi-enzyme complexes associated to actin that are located largely in sites with high ATP demand in proximity to lamellipodia and filopodia which drive the phenotype of migration [83,109,217].

A decrease in proliferation is consistent with the finding that HUVECs lacking NIT2, in a manner similar to the knockout of GLS1, showed reduced α-ketoglutarate levels. Additionally, the knockout of NIT2 led to an accumulation of KGM indicating that hydrolysis of KGM to α-ketoglutarate in cell culture is very efficient. Interestingly, the

simultaneous knockout of both, GLS1 and NIT2, did not further decrease α-ketoglutarate levels. This indicates that HUVECs potentially may contain compensatory mechanisms, e.g. by increasing glucose oxidation, to maintain α-ketoglutarate levels. The exact contribution of each glutamine pathway (i.e. glutaminase I *vs.* glutaminase II) can only be determined by tracer studies using labeled ^{13}C-L-glutamine which will be carried out in the future.

HUVECs spheroid assays revealed that NIT2 deficiency reduces angiogenic sprouting in a manner similar to the knockout of GLS1. Glutamine metabolism is essential for vessel sprouting *in vivo* as shown by an inducible ECs specific GLS1 knockout mouse [91,92]. It has been speculated that this is due to the role of GLS1 in ECs migration, because high motility is essential for ECs to reach the tip position in the vascular sprout [218,219]. Nevertheless, the exact mechanisms of how glutamine metabolism affects ECs motility and thereby angiogenic sprouting are not clear. Recent results are contradictory. On the one hand, glutamine metabolism is essential for migration of non-endothelial cells types [220] and promotes cancer cell migration [221]. Furthermore, glutamine is essential for redox homeostasis and thereby it might affect cell migration during angiogenic sprouting [222]. On the other hand, as mentioned before, glutamine has been shown to be dispensable for endothelial cell migration in a cell culture model [92]. Therefore, the exact mechanisms as to how glutamine metabolism affects vessel sprouting must await future research.

5.5 NIT2 is associated with key enzymes of glutamine metabolism

ω-Amidase/NIT2 activity is present in all rat tissues investigated, exhibiting highest specific activity in kidney and liver [111,114,117]. The NIT2 mRNA is also present in all human tissues investigated with highest levels in liver and kidney [146]. As previously mentioned, considerable activity was detected in both cytoplasm and mitochondria. How the protein is imported into the mitochondria remains unknown as the enzyme contains no known specific mitochondrial importing sequence [111].

The data of this study revealed that the heat shock protein 10 (HSPE1), a subunit of the mitochondrial HSP10/HSP60 chaperone complex, is the most abundantly detected interaction partner of NIT2. This complex assists in the folding of proteins within the mitochondrial matrix and reveals a possible explanation to the question of how the enzyme is imported into the mitochondria. HSP60 was not identified to interact with NIT2, which might be due to positioning of the biotin ligase at the C-terminus of NIT2. Nevertheless, a proximity between NIT2 and HSP60 appears likely and could be validated by proximity ligation assays. Western blot analysis and immunofluorescence actually showed expression of NIT2 in both compartments of HUVECs. Whether the enzyme is only active in the mitochondria could not be answered by this study. Possibly, it exhibits considerable activity in the cytoplasm of ECs but its cytosolic interaction partners are not sufficiently close to become specifically biotinylated.

Next in abundance to HSPE1, the BioID2 approach revealed GLUD1 and DLST as interaction partners of NIT2. GLUD1 converts glutamate into α-ketoglutarate and vice versa. The enzyme appears to be involved in both synthesis and catabolism of glutamate. Whether the interaction of NIT2 and GLUD1 is of physiological relevance remains an open question. Thermodynamically the reductive amination of α-ketoglutarate is favored *in vitro*. However, α-ketoglutarate formation is favored *in vivo*, because α-ketoglutarate is rapidly utilized by other enzymes. Nevertheless, a direct flow from NIT2-derived α-ketoglutarate to GLUD1 appears possible [223]. On the other hand, GLUD1 and NIT2 could simply be in close proximity to each other due to their role in glutamine metabolism. This is different to the interaction with DLST, in which the enzyme can directly utilize the NIT2-derived α-ketoglutarate within the TCA cycle. The direct association with a component of the αKGDHC highlights the potential importance of NIT2 in (endothelial) glutamine metabolism.

5.6 Glutamine metabolism revised

The present thesis expands the understanding of glutamine metabolism by introducing the glutaminase II pathway as a source of α-ketoglutarate and amino acid replenishment in endothelial cells, which stand apart from the classical understanding of glutaminolysis (glutaminase I pathway: Gln → Glu → αKG) (**Fig. 42**).

A question that arises is why mammals have evolved two pathways to metabolize glutamine? As mentioned above, the glutamine transaminases have broad α-keto acid specificity. Interestingly, many transaminase reactions are freely reversible and can be unspecific. For example, both the cytosolic and mitochondrial forms of aspartate aminotransferase (ASAT) show activity towards the aromatic amino acids [103,224,225]. Therefore, the glutaminase II pathway possibly salvages α-keto acids to replenish amino acids that might otherwise be “lost” by non-specific transamination, and at the same time providing another source of α-ketoglutarate. Importantly, transamination of glutamine is largely irreversible due to KGM cyclizing to its stable lactam form (99.7% at equilibrium) [103,112]. The data of the present work show that in cell culture conditions, the hydrolysis of the linear form of KGM appears to be very efficient.

In this context, ECs have a high capacity to shuttle α-keto acids on a cellular but also on a subcellular level. Proton-coupled monocarboxylate transporters transport a variety of carboxylates such as α-ketoglutarate, L-lactate, KMBA, α-ketobutyrate and ketone bodies across the cell membrane [226–229]. Therefore, α-keto acid substrates of the glutamine transaminases can be exchanged between intracellular and extracellular space. Several mitochondrial carriers that belong to the solute carrier superfamily 25 (SLC25) transport α-keto acids and amino across the mitochondrial membrane [228,230]. This fits into the picture of both, KYAT3/GTL and NIT2, operating in the mitochondria and a knockout of the glutamine transaminases reduces methionine levels. Which other amino acids are being replenished by transamination of glutamine has not been studied systematically and will be subject of future research. Additionally, generation of α-ketoglutarate via the glutaminase II pathway may be advantageous to the cell as the production of α-ketoglutarate does not involve a net oxidation. Thus, the glutaminase II pathway can operate in hypoxic regions – this would be especially advantageous for cancers [103]. Interestingly in ECs, the contribution of

glutamine to α-ketoglutarate production and TCA cycle intermediates remains constant, in both normoxia and hypoxia [91,92]. Still, there is no differentiation between glutaminase I and glutaminase II pathway-derived α-ketoglutarate. Further experiments (e.g. by metabolic tracing) are essential to understand the exact contribution of both glutaminase pathways to α-ketoglutarate synthesis in hypoxic and normoxic conditions.

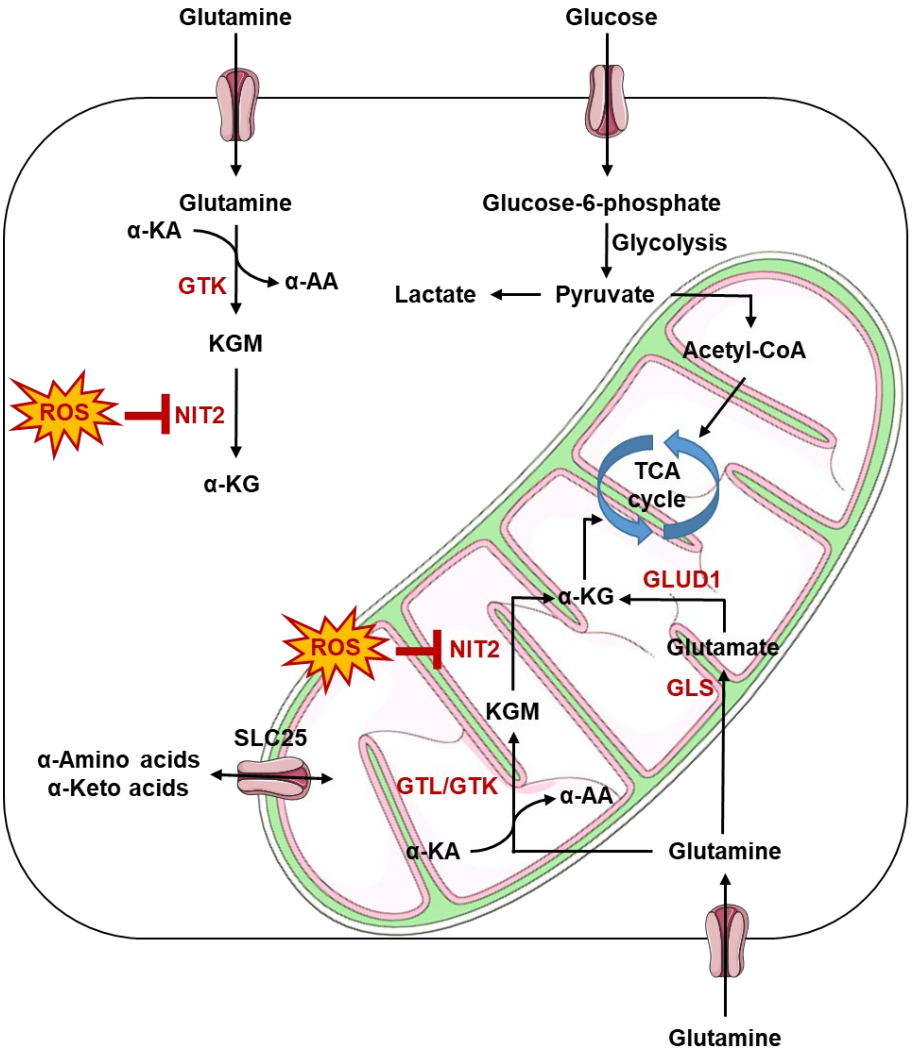

Figure 42. Glutamine metabolism revised
Glutamine enters the cell via amino acid transporters. In the cell glutamine can be hydrolyzed to glutamate which is then de-aminated/transaminated to α-ketoglutarate (glutaminase I pathway). Alternatively, glutamine is transaminated to α-ketoglutaramate to replenish amino acids such as methionine. KGM is hydrolyzed to α-ketoglutarate by the redox-sensitive ω-amidase/NIT2 which occurs in both the cytosol and the mitochondria (glutaminase II pathway). α-KG, α-ketoglutarate; KGM, α-ketoglutaramate; α-KA, α-keto acid; α-AA, α-amino acid.

6. Outlook

Glutamine is an essential energy source for proliferating cells. In the literature glutamine metabolism of ECs has invariably been shown as the conversion of glutamine to glutamate followed by de-amination or transamination of glutamate to α-ketoglutarate. However, the present work shows that enzymes of an alternative pathway for glutamine conversion to α-ketoglutarate are also well represented in ECs. In this pathway (glutaminase II pathway) glutamine is transaminated to KGM with a suitable α-keto acid acceptor leading to the formation of the corresponding α-amino acid. KGM is then hydrolyzed by ω-amidase/NIT2 to α-ketoglutarate and ammonia.

Herein we show that the enzyme ω-amidase/NIT2 is inhibited by high concentrations of H_2O_2. Thereby, our work provides the first systematic analysis of the importance of this alternative pathway for glutamine utilization in endothelial cells. We show that NIT2 significantly contributes to intracellular α-ketoglutarate levels and deletion of the enzyme has considerable effects on cell proliferation and angiogenic sprouting. For validation, further research is necessary to emphasize the importance of the glutaminase II pathway in an *in vivo* model. The importance of both ω-amidase/NIT2 and the glutamine transaminases should be highlighted in any further studies of glutamine metabolism in ECs.

Apart from endothelial cell metabolism, clinical studies are ongoing to test the efficacy of GLS1 inhibitors in cancer therapy. The line of thought behind these studies is that inhibition of GLS1 should decrease α-ketoglutarate carbons that can enter the TCA cycle. As the glutaminase II pathway provides an alternative source of α-ketoglutarate, it can be suggested that an inhibitor of the ω-amidase/NIT2 may provide an effective anti-cancer strategy in combination with a GLS1 inhibitor.

Collectively, our observations suggest that we have identified a novel redox-switch in metabolism, as well as brought to light a previously unknown endothelial glutamine metabolic pathway (the glutaminase II pathway). This study will stimulate further research into the glutaminase II pathway and especially the role of the underappreciated enzyme ω-amidase/NIT2 in general glutamine metabolism.

7. Deutsche Zusammenfassung

Der Begriff reaktive Sauerstoffspezies umfasst freie Radikale wie Superoxidanionen ($O_2^{\bullet -}$), Hydroxylradikale ($HO^{\bullet}$) und stabile molekulare Oxidantien wie Wasserstoffperoxid (H_2O_2). Sie entstehen im Rahmen normaler Stoffwechselvorgänge in den verschiedenen Zellkompartimenten wie dem Zytoplasma, den Mitochondrien oder an der Zellmembran.

Superoxidanionen werden als Nebenprodukt der Zellatmung (Komplexe I und III) sowie durch Lipoxygenasen oder Xanthinoxidasen generiert. Aufgrund ihrer negativen Ladung können sie die Plasmamembran nicht passieren und reagieren langsam und wenig selektiv. Innerhalb der Zelle wird Superoxid durch das Enzym Superoxid-Dismutase zu H_2O_2 abgebaut. Die physiologische intrazelluläre H_2O_2 Konzentration liegt zwischen 1 und 10 nM. Im Vergleich zu Superoxid- und Hydroxylradikalen hat H_2O_2 innerhalb der Zelle eine relativ lange Lebensdauer (~10 s).

Jahrzehntelang wurden reaktive Sauerstoffspezies als schädliche Nebenprodukte des zellulären aeroben Stoffwechsels eingestuft, da sie in der Lage sind, die DNS, Lipide oder Proteine zu oxidieren. Hiermit assoziiert ist das Konzept des oxidativen Stresses, der eine Stoffwechsellage bezeichnet, in der die Zelle durch reaktive Sauerstoffspezies geschädigt wird. Er gilt als zentrales Merkmal verschiedener Krankheiten wie Krebs oder Atherosklerose. Diese Vorstellung änderte sich mit der Beobachtung, dass exogenes H_2O_2 die Aktivität von Wachstumsfaktoren imitieren kann. Heutzutage wird angenommen, dass reaktive Sauerstoffspezies in geringen Konzentrationen eine wichtige Signalfunktion haben, wohingegen hohe Konzentrationen als krankheitsfördernd eingestuft werden.

Den Zellen stehen verschiedene Schutzmechanismen zur Verfügung, um die negativen Auswirkungen akuten oxidativen Stresses zu reduzieren. Einerseits existiert ein antioxidatives Schutzsystem, das aus enzymatischen und nicht-enzymatischen Radikalfängern besteht, andererseits existieren Reparaturmechanismen zum Schutz der DNS sowie die Möglichkeit zum gezielten Abbau von geschädigten Proteinen.

Die vorliegende Arbeit beschäftigt sich primär mit dem Einfluss von reaktiven Sauerstoffspezies auf den Metabolismus von Endothelzellen, die die innerste Zellschicht der Blutgefäße bilden. Von besonderer wissenschaftlicher Bedeutung ist hier, dass die metabolische und transkriptionelle Antwort von Endothelzellen auf verschiedene Arten und Konzentrationen von reaktiven Sauerstoffspezies noch nicht vollständig erforscht ist. Bisher fehlten geeignete Ansätze, um die Effekte der intrazellulären Produktion von reaktiven Sauerstoffspezies besser zu verstehen. Dieses Verständnis ist aber essentiell, da viele Schlussfolgerungen über die biologische Rolle von H_2O_2 im Zusammenhang mit der Signaltransduktion durch die Zugabe von extrazellulärem H_2O_2 getroffen wurden. Dies spiegelt jedoch nicht die Dynamik des intrazellulären H_2O_2-Flusses bei der Regulierung der Signaltransduktion wider.

Um die metabolischen und transkriptionellen Auswirkungen von intrazellulär produziertem H_2O_2 mit anderen Arten von reaktiven Sauerstoffspezies zu vergleichen, wurde ein enzymatischer Ansatz zur Produktion von intrazellulärem H_2O_2 gewählt. Dieser Ansatz basiert auf der Überexpression des Enzymes D-Aminosäure-Oxidase (DAO) in Endothelzellen. Das Enzym wird hauptsächlich im Gehirn exprimiert und oxidiert D-Aminosäuren zu ihren entsprechenden Iminosäuren und H_2O_2. Das Imin wird dann nicht-enzymatisch zu seiner entsprechenden α-Ketosäure hydrolysiert. DAO ist stereospezifisch für D-Aminosäuren (z. B. D-Alanin). Daher ermöglicht die Zugabe von D-Aminosäuren zu Zellen, die DAO exprimieren, die kontrollierte Produktion von intrazellulärem H_2O_2.

Im Rahmen dieser Arbeit wurde zunächst die lentivirale Überexpression der DAO in Nabelschnurendothelzellen etabliert. Dieser Ansatz wurde anschließend molekularbiologisch charakterisiert: Es konnte gezeigt werden, dass die Zugabe von D-Alanin intrazelluläres H_2O_2 generiert, welches spezifische Redox-Proteine (bspw. Peroxiredoxine) oxidiert.

Im Anschluss wurde dieses Modell genutzt, um die zeitabhängige metabolische und transkriptionelle Antwort von Nabelschnurendothelzellen auf intrazellulär-generiertes H_2O_2 (durch die Stimulation mit 3 mM D-Alanin) im Vergleich zu extrazellulär hinzugefügtem H_2O_2 (10 µM und 300 µM) und intrazellulär-generiertem Superoxid (durch die Zugabe von Menadion) zu untersuchen. In diesem Rahmen wurde das

metabolische Profil der Zellen mithilfe moderner (ungerichteter) Massenspektrometrie zu verschiedenen Stimulationszeitpunkten analysiert. Weiterhin wurde die RNS der Proben sequenziert, um die zeitabhängigen transkriptionellen Veränderungen zu detektieren.

Die Ergebnisse dieser Arbeit zeigen, dass unterschiedliche reaktive Sauerstoffspezies in Abhängigkeit von ihrem Entstehungsort und ihrer Konzentration unterschiedliche Effekte auf die Genexpression und den Stoffwechsel von Endothelzellen haben. Während 300 µM extrazelluläres H_2O_2 zu einer starken metabolischen und transkriptionellen Antwort führte, sind die Auswirkungen von intrazellulär-produziertem H_2O_2 und Superoxidanionen vor allem auf Genexpressionsebene detektierbar. Die unterschiedlichen reaktiven Sauerstoffspezies beeinflussten vor allem die Expression ribosomaler RNS. Die Ergebnisse deuten darauf hin, dass einerseits die Lokalisation als auch die Konzentration von reaktiven Sauerstoffspezies von erheblicher Bedeutung für ihre biologischen Effekte sind.

Insbesondere wurde im Rahmen dieser Arbeit festgestellt, dass die Stimulation von Nabelschnurendothelzellen mit 300 µM extrazellulärem H_2O_2 das Enzym ω-Amidase/NIT2 vorübergehend inaktiviert und dadurch das Edukt von NIT2, α-Ketoglutaramat (KGM), in den Zellen temporär akkumuliert. Gleichzeitig kommt es zu einer relativen Konzentrationsreduktion von α-Ketoglutarat (dem Produkt von NIT2) und den nachgelagerten Metaboliten des Citratzyklus. Die temporäre Inaktivierung des Enzyms Aconitase durch Menadion-generierte Superoxidanionen führt zu einer Reduktion der relativen Isocitrat-Konzentration, eine Reduktion der α-Ketoglutarat-Konzentration sowie ein Zusammenbruch des Citratzyklus ist allerdings nicht zu beobachten.

In Endothelzellen ist α-Ketoglutarat essentiell für die Aufrechterhaltung des Citratzyklus und wird vor allem aus L-Glutamin synthetisiert. In verschiedenen Publikationen wurde gezeigt, dass über 70% der Kohlenstoffatome aus dem Citratzyklus der Endothelzellen von Glutamin stammen. Die vorliegenden Daten deuten daher darauf hin, dass eine Stimulation mit 300 µM extrazellulärem H_2O_2 direkt den Glutamin-Stoffwechsel der Endothelzelle beeinflusst.

Das Enzym ω-Amidase/NIT2 ist das Schlüsselenzym des Glutaminase II Stoffwechselweges. Im Rahmen dieses Stoffwechselweges wird Glutamin mit einer passenden α-Ketosäure zu α-Ketoglutaramat transaminiert. Aus der α-Ketosäure entsteht die entsprechende α-Aminosäure. Dieser Stoffwechselweg wurde bisher nicht systematisch erforscht, da das Schlüsselmetabolit, α-Ketoglutaramat, nicht als konventioneller Standard für eine gezielte massenspektrometrische Analyse erhältlich ist. 2020 wurde erstmalig eine organische Synthesestrategie publiziert. Im Rahmen einer Kollaboration mit der Arbeitsgruppe um Prof. Dr. Travis T. Denton (Washington State University, Spokane, USA) wurde ein interner Standard für den gezielten Nachweis von α-Ketoglutaramat in Zellen sowie Plasma- und Serumproben etabliert.

Diese Arbeit untersucht erstmalig die physiologische Relevanz des Glutaminase II Stoffwechselweges in Endhotelzellen. Es konnte gezeigt werden, dass Nabelschnurendothelzellen, die kein NIT2 exprimieren, langsamer proliferieren und eine verminderte angiogene Kapazität aufweisen. Außerdem zeigen die hier erhobenen Daten, dass das Enzym in den Mitochondrien und im Cytoplasma lokalisiert ist. Mithilfe der Proximity-labeling Technik, BioID, wurden die Interaktionspartner von NIT2 bestimmt. Bei dieser Methode wurde ein NIT2-BioID Fusionsprotein in Endothelzellen exprimiert. Die proximalen Proteine wurden nach Zugabe von Biotin durch eine Streptavidin-Präzipitation isoliert und massenspektrometrisch analysiert. Die Daten zeigen, dass NIT2 wahrscheinlich über ein Chaperon (HSPE1) in die Mitochondrien importiert wird. Dort interagiert NIT2 mit der Glutamatdehydrogenase und dem α-Ketoglutaratdehydrogenase-Komplex. Beide sind Schlüsselenzyme des Glutamin/Glutamat/α-Ketoglutarat-Stoffwechsels.

Weiterhin wurde mithilfe gezielter Massenspektrometrie gezeigt, dass ein Knockout von NIT2 durch das CRISPR/Cas9-System die α-Ketoglutarat-Konzentration in Endothelzellen reduziert. Parallel akkumuliert α-Ketoglutaramat innerhalb der Zelle. α-Ketoglutaramat konnte, unter basalen Bedingungen, in Endothellzellen nicht detektiert werden. Dies deutet darauf, dass die Hydrolyse von α-Ketoglutaramat zu α-Ketoglutarat unter Zellkulturbedingungen sehr effizient ist. Der Knockout der Glutamin-Transaminasen führt außerdem zu einer Verringerung der Methionin-Konzentration und einem Anstieg der korrespondierenden α-Ketosäure (α-Keto-γ-(methylthio)-Buttersäure).

Der Glutaminase-II-Stoffwechselweg stellt somit einen unterschätzten und redox-sensitiven Stoffwechselweg in Endothelzellen dar. Die genetische Deletion von NIT2 hat beträchtliche physiologische Auswirkungen, was die Bedeutung von Glutamin für Endothelzellen unterstreicht.

Der Glutamin-Stoffwechsel wird in der wissenschaftlichen Literatur zumeist nur mit der Umwandlung von Glutamin zu Glutamat und der anschließenden Desaminierung/ Transaminierung von Glutamat zu α-Ketoglutarat beschrieben. Unsere Ergebnisse zeigen, dass ein zweiter Stoffwechselweg zur Synthese von α-Ketoglutarat in Endothelzellen von Relevanz ist.

Zur Validierung ist weitere experimentelle Forschung notwendig, um die Bedeutung des Glutaminase II Wegs in einem *in-vivo*-Modell zu untersuchen. Die Bedeutung sowohl von NIT2 als auch von den Glutamin-Transaminasen sollte in allen weiteren Studien zum Glutamin-Stoffwechsel hervorgehoben werden.

Weiterhin werden derzeit klinische Studien durchgeführt, um die Wirksamkeit von Glutaminase-Inhibitoren in der Krebstherapie zu testen. Der Gedanke hinter dieser Strategie ist es, die durch α-Ketoglutarat in den Citratzyklus eingespeisten Kohlenstoffe zu verringern. Da der Glutaminase-II-Stoffwechselweg eine alternative Quelle für α-Ketoglutarat darstellt, liegt die Vermutung nahe, dass ein Inhibitor der ω-Amidase/NIT2 in Kombination mit einem Glutaminase-Inhibitor eine wirksame Strategie zur Krebsbekämpfung darstellen könnte.

Insgesamt deuten die Ergebnisse dieser Arbeit daraufhin, dass ein neuer Redox-Schalter im Zusammenhang mit einem bisher unbekannten Glutamin-Stoffwechselweg in Endothelzellen identifiziert wurde. Diese Studie bildet die Grundlage für weitere Forschungen zum Glutaminase-II-Stoffwechselweg und insbesondere zur Rolle des unterschätzten Enzyms ω-Amidase/NIT2 im allgemeinen Glutamin-Stoffwechsel.

8. Bibliography

[1] D.G. Allen, G.D. Lamb, H. Westerblad, Skeletal muscle fatigue: cellular mechanisms, Physiol. Rev. 88 (2008) 287–332. https://doi.org/10.1152/physrev.00015.2007.

[2] K. Brieger, S. Schiavone, F.J. Miller, K.-H. Krause, Reactive oxygen species: from health to disease, Swiss Med. Wkly. 142 (2012) w13659. https://doi.org/10.4414/smw.2012.13659.

[3] J.P.T. Ward, From Physiological Redox Signalling to Oxidant Stress, in: Y.-X. Wang (Ed.), Pulmonary Vasculature Redox Signaling in Health and Disease, Springer International Publishing, Cham, 2017, pp. 335–342.

[4] S.J. Forrester, D.S. Kikuchi, M.S. Hernandes, Q. Xu, K.K. Griendling, Reactive Oxygen Species in Metabolic and Inflammatory Signaling, Circulation Research 122 (2018) 877–902. https://doi.org/10.1161/CIRCRESAHA.117.311401.

[5] X. Li, P. Fang, J. Mai, E.T. Choi, H. Wang, X. Yang, Targeting mitochondrial reactive oxygen species as novel therapy for inflammatory diseases and cancers, J Hematol Oncol 6 (2013) 19. https://doi.org/10.1186/1756-8722-6-19.

[6] R.P. Brandes, N. Weissmann, K. Schröder, Nox family NADPH oxidases: Molecular mechanisms of activation, Free Radic. Biol. Med. 76 (2014) 208–226. https://doi.org/10.1016/j.freeradbiomed.2014.07.046.

[7] K. Schröder, N. Weissmann, R.P. Brandes, Organizers and activators: Cytosolic Nox proteins impacting on vascular function, Free Radic. Biol. Med. 109 (2017) 22–32. https://doi.org/10.1016/j.freeradbiomed.2017.03.017.

[8] C.A.K. Lundgren, D. Sjöstrand, O. Biner, M. Bennett, A. Rudling, A.-L. Johansson, P. Brzezinski, J. Carlsson, C. von Ballmoos, M. Högbom, Scavenging of superoxide by a membrane-bound superoxide oxidase, Nat. Chem. Biol. 14 (2018) 788–793. https://doi.org/10.1038/s41589-018-0072-x.

[9] A. Donkó, Z. Péterfi, A. Sum, T. Leto, M. Geiszt, Dual oxidases, Phil. Trans. R. Soc. B 360 (2005) 2301–2308. https://doi.org/10.1098/rstb.2005.1767.

[10] D.D. Thomas, X. Liu, S.P. Kantrow, J.R. Lancaster, The biological lifetime of nitric oxide: implications for the perivascular dynamics of NO and O2, Proc. Natl. Acad. Sci. U. S. A. 98 (2001) 355–360. https://doi.org/10.1073/pnas.011379598.

[11] B. D'Autréaux, M.B. Toledano, ROS as signalling molecules: mechanisms that generate specificity in ROS homeostasis, Nature Reviews Molecular Cell Biology 8 (2007) 813–824. https://doi.org/10.1038/nrm2256.

[12] H. Sies, Hydrogen peroxide as a central redox signaling molecule in physiological oxidative stress: Oxidative eustress, Redox Biol. 11 (2017) 613–619. https://doi.org/10.1016/j.redox.2016.12.035.

[13] M. Gutscher, M.C. Sobotta, G.H. Wabnitz, S. Ballikaya, A.J. Meyer, Y. Samstag, T.P. Dick, Proximity-based protein thiol oxidation by H2O2-scavenging peroxidases, J. Biol. Chem. 284 (2009) 31532–31540. https://doi.org/10.1074/jbc.M109.059246.

[14] J.C. Lim, J.M. Gruschus, G. Kim, B.S. Berlett, N. Tjandra, R.L. Levine, A low pKa cysteine at the active site of mouse methionine sulfoxide reductase A, J. Biol. Chem. 287 (2012) 25596–25601. https://doi.org/10.1074/jbc.M112.369116.

[15] R.P. Brandes, N. Weissmann, K. Schröder, Redox-mediated signal transduction by cardiovascular Nox NADPH oxidases, J. Mol. Cell. Cardiol. 73 (2014) 70–79. https://doi.org/10.1016/j.yjmcc.2014.02.006.

[16] M. Rinnerthaler, J. Bischof, M.K. Streubel, A. Trost, K. Richter, Oxidative stress in aging human skin, Biomolecules 5 (2015) 545–589. https://doi.org/10.3390/biom5020545.

[17] R.V. Lloyd, P.M. Hanna, R.P. Mason, The Origin of the Hydroxyl Radical Oxygen in the Fenton Reaction, Free Radical Biology and Medicine 22 (1997) 885–888. https://doi.org/10.1016/S0891-5849(96)00432-7.

[18] P.D. Ray, B.-W. Huang, Y. Tsuji, Reactive oxygen species (ROS) homeostasis and redox regulation in cellular signaling, Cell. Signal. 24 (2012) 981–990. https://doi.org/10.1016/j.cellsig.2012.01.008.

[19] E. Birben, U.M. Sahiner, C. Sackesen, S. Erzurum, O. Kalayci, Oxidative stress and antioxidant defense, World Allergy Organization Journal 5 (2012) 9–19. https://doi.org/10.1097/WOX.0b013e3182439613.

[20] H. Sies, Glutathione and its role in cellular functions, Free Radical Biology and Medicine 27 (1999) 916–921. https://doi.org/10.1016/S0891-5849(99)00177-X.

[21] S. Curello, C. Ceconi, C. Bigoli, R. Ferrari, A. Albertini, C. Guarnieri, Changes in the cardiac glutathione status after ischemia and reperfusion, Experientia 41 (1985) 42–43. https://doi.org/10.1007/BF02005863.

[22] D.A. Dickinson, H.J. Forman, Glutathione in defense and signaling: lessons from a small thiol, Annals of the New York Academy of Sciences 973 (2002) 488–504. https://doi.org/10.1111/j.1749-6632.2002.tb04690.x.

[23] H.N. Kirkman, M. Rolfo, A.M. Ferraris, G.F. Gaetani, Mechanisms of protection of catalase by NADPH. Kinetics and stoichiometry, Journal of Biological Chemistry 274 (1999) 13908–13914. https://doi.org/10.1074/jbc.274.20.13908.

[24] C. Lennicke, H.M. Cochemé, Redox metabolism: ROS as specific molecular regulators of cell signaling and function, Mol. Cell 81 (2021) 3691–3707. https://doi.org/10.1016/j.molcel.2021.08.018.

[25] A. Meister, Metabolism and functions of glutathione, Trends in Biochemical Sciences 6 (1981) 231–234. https://doi.org/10.1016/0968-0004(81)90084-0.

[26] P.F. Surai, I.I. Kochish, V.I. Fisinin, Glutathione peroxidases in poultry biology: Part 1. Classification and mechanisms of action, World's Poultry Science Journal 74 (2018) 185–198. https://doi.org/10.1017/S0043933918000284.

[27] J.D. Lambeth, NOX enzymes and the biology of reactive oxygen, Nat. Rev. Immunol. 4 (2004) 181–189. https://doi.org/10.1038/nri1312.

[28] H. Sies, Oxidative stress: a concept in redox biology and medicine, Redox Biol. 4 (2015) 180–183. https://doi.org/10.1016/j.redox.2015.01.002.

[29] R.J. Reiter, D. Melchiorri, E. Sewerynek, B. Poeggeler, L. Barlow-Walden, J. Chuang, G.G. Ortiz, D. AcuñaCastroviejo, A review of the evidence supporting melatonin's role as an antioxidant, J Pineal Res 18 (1995) 1–11. https://doi.org/10.1111/j.1600-079X.1995.tb00133.x.

[30] M. Schieber, N.S. Chandel, ROS function in redox signaling and oxidative stress, Curr. Biol. 24 (2014) R453-62. https://doi.org/10.1016/j.cub.2014.03.034.

[31] G.S.A.T. van Rossum, G.P.C. Drummen, A.J. Verkleij, J.A. Post, J. Boonstra, Activation of cytosolic phospholipase A2 in Her14 fibroblasts by hydrogen peroxide: a p42/44(MAPK)-dependent and phosphorylation-independent mechanism, Biochim. Biophys. Acta 1636 (2004) 183–195. https://doi.org/10.1016/j.bbalip.2003.12.008.

[32] H.J. Forman, F. Ursini, M. Maiorino, An overview of mechanisms of redox signaling, J. Mol. Cell. Cardiol. 73 (2014) 2–9. https://doi.org/10.1016/j.yjmcc.2014.01.018.

[33] S. García-Santamarina, S. Boronat, E. Hidalgo, Reversible cysteine oxidation in hydrogen peroxide sensing and signal transduction, Biochemistry 53 (2014) 2560–2580. https://doi.org/10.1021/bi401700f.

[34] M.A. Wilson, The role of cysteine oxidation in DJ-1 function and dysfunction, Antioxidants & Redox Signaling 15 (2011) 111–122. https://doi.org/10.1089/ars.2010.3481.

[35] E. Jortzik, L. Wang, K. Becker, Thiol-based posttranslational modifications in parasites, Antioxidants & Redox Signaling 17 (2012) 657–673. https://doi.org/10.1089/ars.2011.4266.

[36] J.B. Behring, S. van der Post, A.D. Mooradian, M.J. Egan, M.I. Zimmerman, J.L. Clements, G.R. Bowman, J.M. Held, Spatial and temporal alterations in protein structure by EGF regulate cryptic cysteine oxidation, Sci. Signal. 13 (2020) eaay7315. https://doi.org/10.1126/scisignal.aay7315.

[37] J.R. Stone, An assessment of proposed mechanisms for sensing hydrogen peroxide in mammalian systems, Arch. Biochem. Biophys. 422 (2004) 119–124. https://doi.org/10.1016/j.abb.2003.12.029.

[38] R. Brigelius-Flohé, L. Flohé, Basic principles and emerging concepts in the redox control of transcription factors, Antioxidants & Redox Signaling 15 (2011) 2335–2381. https://doi.org/10.1089/ars.2010.3534.

[39] S. Stöcker, M. Maurer, T. Ruppert, T.P. Dick, A role for 2-Cys peroxiredoxins in facilitating cytosolic protein thiol oxidation, Nat. Chem. Biol. 14 (2018) 148–155. https://doi.org/10.1038/nchembio.2536.

[40] A. Perkins, K.J. Nelson, D. Parsonage, L.B. Poole, P.A. Karplus, Peroxiredoxins: guardians against oxidative stress and modulators of peroxide signaling, Trends in Biochemical Sciences 40 (2015) 435–445. https://doi.org/10.1016/j.tibs.2015.05.001.

[41] E.A. Veal, Z.E. Underwood, L.E. Tomalin, B.A. Morgan, C.S. Pillay, Hyperoxidation of Peroxiredoxins: Gain or Loss of Function?, Antioxidants & Redox Signaling 28 (2018) 574–590. https://doi.org/10.1089/ars.2017.7214.

[42] G. Detienne, W. de Haes, L. Mergan, S.L. Edwards, L. Temmerman, S. van Bael, Beyond ROS clearance: Peroxiredoxins in stress signaling and aging, Ageing Research Reviews 44 (2018) 33–48. https://doi.org/10.1016/j.arr.2018.03.005.

[43] R.D.M. Travasso, F. Sampaio Dos Aidos, A. Bayani, P. Abranches, A. Salvador, Localized redox relays as a privileged mode of cytoplasmic hydrogen peroxide signaling, Redox Biol. 12 (2017) 233–245. https://doi.org/10.1016/j.redox.2017.01.003.

[44] L. Flohé, The impact of thiol peroxidases on redox regulation, Free radical research 50 (2016) 126–142. https://doi.org/10.3109/10715762.2015.1046858.

[45] A.G. Barata, T.P. Dick, A role for peroxiredoxins in H2O2- and MEKK-dependent activation of the p38 signaling pathway, Redox Biol. 28 (2020) 101340. https://doi.org/10.1016/j.redox.2019.101340.

[46] M.C. Sobotta, W. Liou, S. Stöcker, D. Talwar, M. Oehler, T. Ruppert, A.N.D. Scharf, T.P. Dick, Peroxiredoxin-2 and STAT3 form a redox relay for H2O2 signaling, Nat. Chem. Biol. 11 (2015) 64–70. https://doi.org/10.1038/nchembio.1695.

[47] L.E.S. Netto, F. Antunes, The Roles of Peroxiredoxin and Thioredoxin in Hydrogen Peroxide Sensing and in Signal Transduction, Molecules and Cells 39 (2016) 65–71. https://doi.org/10.14348/molcells.2016.2349.

[48] R.M. Jarvis, S.M. Hughes, E.C. Ledgerwood, Peroxiredoxin 1 functions as a signal peroxidase to receive, transduce, and transmit peroxide signals in mammalian cells, Free Radic. Biol. Med. 53 (2012) 1522–1530. https://doi.org/10.1016/j.freeradbiomed.2012.08.001.

[49] S.B. Wall, J.-Y. Oh, A.R. Diers, A. Landar, Oxidative modification of proteins: an emerging mechanism of cell signaling, Frontiers in Physiology 3 (2012) 369. https://doi.org/10.3389/fphys.2012.00369.

[50] D. Shao, S.-I. Oka, T. Liu, P. Zhai, T. Ago, S. Sciarretta, H. Li, J. Sadoshima, A redox-dependent mechanism for regulation of AMPK activation by Thioredoxin1 during energy starvation, Cell Metab. 19 (2014) 232–245. https://doi.org/10.1016/j.cmet.2013.12.013.

[51] J.W. Zmijewski, S. Banerjee, H. Bae, A. Friggeri, E.R. Lazarowski, E. Abraham, Exposure to hydrogen peroxide induces oxidation and activation of AMP-activated protein kinase, J. Biol. Chem. 285 (2010) 33154–33164. https://doi.org/10.1074/jbc.M110.143685.

[52] M.-H. Zou, X.-Y. Hou, C.-M. Shi, S. Kirkpatick, F. Liu, M.H. Goldman, R.A. Cohen, Activation of 5'-AMP-activated kinase is mediated through c-Src and

phosphoinositide 3-kinase activity during hypoxia-reoxygenation of bovine aortic endothelial cells. Role of peroxynitrite, Journal of Biological Chemistry 278 (2003) 34003–34010. https://doi.org/10.1074/jbc.M300215200.

[53] C. Nicholls, H. Li, J.-P. Liu, GAPDH: a common enzyme with uncommon functions, Clinical and Experimental Pharmacology and Physiology 39 (2012) 674–679. https://doi.org/10.1111/j.1440-1681.2011.05599.x.

[54] M.R. Hara, M.B. Cascio, A. Sawa, GAPDH as a sensor of NO stress, Biochim. Biophys. Acta 1762 (2006) 502–509. https://doi.org/10.1016/j.bbadis.2006.01.012.

[55] M. Ham, J.-W. Lee, A.H. Choi, H. Jang, G. Choi, J. Park, C. Kozuka, D.D. Sears, H. Masuzaki, J.B. Kim, Macrophage glucose-6-phosphate dehydrogenase stimulates proinflammatory responses with oxidative stress, Molecular and Cellular Biology 33 (2013) 2425–2435. https://doi.org/10.1128/MCB.01260-12.

[56] L. Kussmaul, J. Hirst, The mechanism of superoxide production by NADH:ubiquinone oxidoreductase (complex I) from bovine heart mitochondria, Proc. Natl. Acad. Sci. U.S.A. 103 (2006) 7607–7612. https://doi.org/10.1073/pnas.0510977103.

[57] T.R. Hurd, Y. Collins, I. Abakumova, E.T. Chouchani, B. Baranowski, I.M. Fearnley, T.A. Prime, M.P. Murphy, A.M. James, Inactivation of pyruvate dehydrogenase kinase 2 by mitochondrial reactive oxygen species, J. Biol. Chem. 287 (2012) 35153–35160. https://doi.org/10.1074/jbc.M112.400002.

[58] L. Tretter, V. Adam-Vizi, Inhibition of Krebs Cycle Enzymes by Hydrogen Peroxide: A Key Role of α-Ketoglutarate Dehydrogenase in Limiting NADH Production under Oxidative Stress, The Journal of neuroscience the official journal of the Society for Neuroscience 20 (2000) 8972–8979. https://doi.org/10.1523/JNEUROSCI.20-24-08972.2000.

[59] L. Tretter, V. Adam-Vizi, Alpha-ketoglutarate dehydrogenase: a target and generator of oxidative stress, Phil. Trans. R. Soc. B 360 (2005) 2335–2345. https://doi.org/10.1098/rstb.2005.1764.

[60] M.A.B. Applegate, K.M. Humphries, L.I. Szweda, Reversible inhibition of alpha-ketoglutarate dehydrogenase by hydrogen peroxide: glutathionylation and protection of lipoic acid, Biochemistry 47 (2008) 473–478. https://doi.org/10.1021/bi7017464.

[61] X. Liu, L. Fan, C. Lu, S. Yin, H. Hu, Functional Role of p53 in the Regulation of Chemical-Induced Oxidative Stress, Oxid. Med. Cell. Longev. 2020 (2020) 6039769. https://doi.org/10.1155/2020/6039769.

[62] Y. Huang, W. Li, Z. Su, A.-N.T. Kong, The complexity of the Nrf2 pathway: beyond the antioxidant response, J. Nutr. Biochem. 26 (2015) 1401–1413. https://doi.org/10.1016/j.jnutbio.2015.08.001.

[63] K. Itoh, T. Chiba, S. Takahashi, T. Ishii, K. Igarashi, Y. Katoh, T. Oyake, N. Hayashi, K. Satoh, I. Hatayama, M. Yamamoto, Y. Nabeshima, An Nrf2/small Maf heterodimer mediates the induction of phase II detoxifying enzyme genes through antioxidant response elements, Biochem. Biophys. Res. Commun. 236 (1997) 313–322. https://doi.org/10.1006/bbrc.1997.6943.

[64] E.L. Mills, D.G. Ryan, H.A. Prag, D. Dikovskaya, D. Menon, Z. Zaslona, M.P. Jedrychowski, A.S.H. Costa, M. Higgins, E. Hams, J. Szpyt, M.C. Runtsch, M.S. King, J.F. McGouran, R. Fischer, B.M. Kessler, A.F. McGettrick, M.M. Hughes, R.G. Carroll, L.M. Booty, E.V. Knatko, P.J. Meakin, M.L.J. Ashford, L.K. Modis, G. Brunori, D.C. Sévin, P.G. Fallon, S.T. Caldwell, E.R.S. Kunji, E.T. Chouchani, C. Frezza, A.T. Dinkova-Kostova, R.C. Hartley, M.P. Murphy, L.A. O'Neill, Itaconate is an anti-inflammatory metabolite that activates Nrf2 via alkylation of KEAP1, Nature 556 (2018) 113–117. https://doi.org/10.1038/nature25986.

[65] I. Bellezza, I. Giambanco, A. Minelli, R. Donato, Nrf2-Keap1 signaling in oxidative and reductive stress, Biochimica et Biophysica Acta (BBA) - Molecular Cell Research 1865 (2018) 721–733. https://doi.org/10.1016/j.bbamcr.2018.02.010.

[66] U. Siebenlist, G. Franzoso, K. Brown, Structure, regulation and function of NF-kappa B, Annu. Rev. Cell. Biol. 10 (1994) 405–455. https://doi.org/10.1146/annurev.cb.10.110194.002201.

[67] R. Schreck, P. Rieber, P.A. Baeuerle, Reactive oxygen intermediates as apparently widely used messengers in the activation of the NF-kappa B transcription factor and HIV-1, EMBO J 10 (1991) 2247–2258. https://doi.org/10.1002/j.1460-2075.1991.tb07761.x.

[68] J.R. Matthews, N. Wakasugi, J.L. Virelizier, J. Yodoi, R.T. Hay, Thioredoxin regulates the DNA binding activity of NF-kappa B by reduction of a disulphide

bond involving cysteine 62, Nucleic Acids Research 20 (1992) 3821–3830. https://doi.org/10.1093/nar/20.15.3821.

[69] J.R. Matthews, W. Kaszubska, G. Turcatti, T.N. Wells, R.T. Hay, Role of cysteine62 in DNA recognition by the P50 subunit of NF-kappa B, Nucleic Acids Research 21 (1993) 1727–1734. https://doi.org/10.1093/nar/21.8.1727.

[70] P.J. Halvey, J.M. Hansen, J.M. Johnson, Y.-M. Go, A. Samali, D.P. Jones, Selective oxidative stress in cell nuclei by nuclear-targeted D-amino acid oxidase, Antioxidants & Redox Signaling 9 (2007) 807–816. https://doi.org/10.1089/ars.2007.1526.

[71] L. Flohé, R. Brigelius-Flohé, C. Saliou, M.G. Traber, L. Packer, Redox Regulation of NF-kappa B Activation, Free Radical Biology and Medicine 22 (1997) 1115–1126. https://doi.org/10.1016/S0891-5849(96)00501-1.

[72] N.V. Iyer, L.E. Kotch, F. Agani, S.W. Leung, E. Laughner, R.H. Wenger, M. Gassmann, J.D. Gearhart, A.M. Lawler, A.Y. Yu, G.L. Semenza, Cellular and developmental control of O2 homeostasis by hypoxia-inducible factor 1 alpha, Genes & Development 12 (1998) 149–162. https://doi.org/10.1101/gad.12.2.149.

[73] P. Carmeliet, Y. Dor, J.M. Herbert, D. Fukumura, K. Brusselmans, M. Dewerchin, M. Neeman, F. Bono, R. Abramovitch, P. Maxwell, C.J. Koch, P. Ratcliffe, L. Moons, R.K. Jain, D. Collen, E. Keshert, E. Keshet, Role of HIF-1alpha in hypoxia-mediated apoptosis, cell proliferation and tumour angiogenesis, Nature 394 (1998) 485–490. https://doi.org/10.1038/28867.

[74] G.Y. Lee, Y.-S. Chun, H.-W. Shin, J.-W. Park, Potential role of the N-MYC downstream-regulated gene family in reprogramming cancer metabolism under hypoxia, Oncotarget 7 (2016) 57442–57451. https://doi.org/10.18632/oncotarget.10684.

[75] M. Putker, T. Madl, H.R. Vos, H. de Ruiter, M. Visscher, M.C.W. van den Berg, M. Kaplan, H.C. Korswagen, R. Boelens, M. Vermeulen, B.M.T. Burgering, T.B. Dansen, Redox-dependent control of FOXO/DAF-16 by transportin-1, Mol. Cell 49 (2013) 730–742. https://doi.org/10.1016/j.molcel.2012.12.014.

[76] Y. Chen, K. Liu, Y. Shi, C. Shao, The tango of ROS and p53 in tissue stem cells, Cell Death Differ. 25 (2018) 639–641. https://doi.org/10.1038/s41418-018-0062-2.

[77] A. Rufini, P. Tucci, I. Celardo, G. Melino, Senescence and aging: the critical roles of p53, Oncogene 32 (2013) 5129–5143. https://doi.org/10.1038/onc.2012.640.

[78] S. Macip, M. Igarashi, P. Berggren, J. Yu, S.W. Lee, S.A. Aaronson, Influence of induced reactive oxygen species in p53-mediated cell fate decisions, Molecular and Cellular Biology 23 (2003) 8576–8585. https://doi.org/10.1128/MCB.23.23.8576-8585.2003.

[79] K. de Bock, M. Georgiadou, P. Carmeliet, Role of endothelial cell metabolism in vessel sprouting, Cell Metab. 18 (2013) 634–647. https://doi.org/10.1016/j.cmet.2013.08.001.

[80] G. Eelen, P. de Zeeuw, M. Simons, P. Carmeliet, Endothelial cell metabolism in normal and diseased vasculature, Circulation Research 116 (2015) 1231–1244. https://doi.org/10.1161/CIRCRESAHA.116.302855.

[81] G. Eelen, P. de Zeeuw, L. Treps, U. Harjes, B.W. Wong, P. Carmeliet, Endothelial Cell Metabolism, Physiol. Rev. 98 (2018) 3–58. https://doi.org/10.1152/physrev.00001.2017.

[82] K. Rohlenova, K. Veys, I. Miranda-Santos, K. de Bock, P. Carmeliet, Endothelial Cell Metabolism in Health and Disease, Trends Cell Biol. 28 (2018) 224–236. https://doi.org/10.1016/j.tcb.2017.10.010.

[83] K. de Bock, M. Georgiadou, S. Schoors, A. Kuchnio, B.W. Wong, A.R. Cantelmo, A. Quaegebeur, B. Ghesquière, S. Cauwenberghs, G. Eelen, L.-K. Phng, I. Betz, B. Tembuyser, K. Brepoels, J. Welti, I. Geudens, I. Segura, B. Cruys, F. Bifari, I. Decimo, R. Blanco, S. Wyns, J. Vangindertael, S. Rocha, R.T. Collins, S. Munck, D. Daelemans, H. Imamura, R. Devlieger, M. Rider, P.P. van Veldhoven, F. Schuit, R. Bartrons, J. Hofkens, P. Fraisl, S. Telang, R.J. DeBerardinis, L. Schoonjans, S. Vinckier, J. Chesney, H. Gerhardt, M. Dewerchin, P. Carmeliet, Role of PFKFB3-driven glycolysis in vessel sprouting, Cell 154 (2013) 651–663. https://doi.org/10.1016/j.cell.2013.06.037.

[84] E. Clementi, G.C. Brown, M. Feelisch, S. Moncada, Persistent inhibition of cell respiration by nitric oxide: crucial role of S-nitrosylation of mitochondrial complex I and protective action of glutathione, Proc. Natl. Acad. Sci. U. S. A. 95 (1998) 7631–7636. https://doi.org/10.1073/pnas.95.13.7631.

[85] M. Cleeter, J.M. Cooper, V.M. Darley-Usmar, S. Moncada, A. Schapira, Reversible inhibition of cytochrome c oxidase, the terminal enzyme of the

mitochondrial respiratory chain, by nitric oxide, FEBS Letters 345 (1994) 50–54. https://doi.org/10.1016/0014-5793(94)00424-2.

[86] A. Galkin, A. Higgs, S. Moncada, Nitric oxide and hypoxia, Essays in Biochemistry 43 (2007) 29–42. https://doi.org/10.1042/bse0430029.

[87] P. Carmeliet, Angiogenesis in life, disease and medicine, Nature 438 (2005) 932–936. https://doi.org/10.1038/nature04478.

[88] A. Wacker, H. Gerhardt, Endothelial development taking shape, Curr. Opin. Cell Biol. 23 (2011) 676–685. https://doi.org/10.1016/j.ceb.2011.10.002.

[89] S. Arima, K. Nishiyama, T. Ko, Y. Arima, Y. Hakozaki, K. Sugihara, H. Koseki, Y. Uchijima, Y. Kurihara, H. Kurihara, Angiogenic morphogenesis driven by dynamic and heterogeneous collective endothelial cell movement, Development 138 (2011) 4763–4776. https://doi.org/10.1242/dev.068023.

[90] S. Schoors, U. Bruning, R. Missiaen, K.C. Queiroz, G. Borgers, I. Elia, A. Zecchin, A.R. Cantelmo, S. Christen, J. Goveia, W. Heggermont, L. Goddé, S. Vinckier, P.P. van Veldhoven, G. Eelen, L. Schoonjans, H. Gerhardt, M. Dewerchin, M. Baes, K. de Bock, B. Ghesquière, S.Y. Lunt, S.-M. Fendt, P. Carmeliet, Fatty acid carbon is essential for dNTP synthesis in endothelial cells, Nature 520 (2015) 192–197. https://doi.org/10.1038/nature14362.

[91] H. Huang, S. Vandekeere, J. Kalucka, L. Bierhansl, A. Zecchin, U. Brüning, A. Visnagri, N. Yuldasheva, J. Goveia, B. Cruys, K. Brepoels, S. Wyns, S. Rayport, B. Ghesquière, S. Vinckier, L. Schoonjans, R. Cubbon, M. Dewerchin, G. Eelen, P. Carmeliet, Role of glutamine and interlinked asparagine metabolism in vessel formation, EMBO J. 36 (2017) 2334–2352. https://doi.org/10.15252/embj.201695518.

[92] B. Kim, J. Li, C. Jang, Z. Arany, Glutamine fuels proliferation but not migration of endothelial cells, EMBO J. 36 (2017) 2321–2333. https://doi.org/10.15252/embj.201796436.

[93] J. Andrade, M. Potente, New Q(ues) to keep blood vessels growing, EMBO J 36 (2017) 2315–2317. https://doi.org/10.15252/embj.201797764.

[94] J. Welti, S. Loges, S. Dimmeler, P. Carmeliet, Recent molecular discoveries in angiogenesis and antiangiogenic therapies in cancer, J. Clin. Invest. 123 (2013) 3190–3200. https://doi.org/10.1172/JCI70212.

[95] G.-X. Ruan, A. Kazlauskas, Lactate engages receptor tyrosine kinases Axl, Tie2, and vascular endothelial growth factor receptor 2 to activate phosphoinositide 3-kinase/Akt and promote angiogenesis, J. Biol. Chem. 288 (2013) 21161–21172. https://doi.org/10.1074/jbc.M113.474619.

[96] F. Végran, R. Boidot, C. Michiels, P. Sonveaux, O. Feron, Lactate influx through the endothelial cell monocarboxylate transporter MCT1 supports an NF-κB/IL-8 pathway that drives tumor angiogenesis, Cancer Research 71 (2011) 2550–2560. https://doi.org/10.1158/0008-5472.CAN-10-2828.

[97] P. Sonveaux, T. Copetti, C.J. de Saedeleer, F. Végran, J. Verrax, K.M. Kennedy, E.J. Moon, S. Dhup, P. Danhier, F. Frérart, B. Gallez, A. Ribeiro, C. Michiels, M.W. Dewhirst, O. Feron, Targeting the lactate transporter MCT1 in endothelial cells inhibits lactate-induced HIF-1 activation and tumor angiogenesis, PLoS ONE 7 (2012) e33418. https://doi.org/10.1371/journal.pone.0033418.

[98] S. Schoors, K. de Bock, A.R. Cantelmo, M. Georgiadou, B. Ghesquière, S. Cauwenberghs, A. Kuchnio, B.W. Wong, A. Quaegebeur, J. Goveia, F. Bifari, X. Wang, R. Blanco, B. Tembuyser, I. Cornelissen, A. Bouché, S. Vinckier, S. Diaz-Moralli, H. Gerhardt, S. Telang, M. Cascante, J. Chesney, M. Dewerchin, P. Carmeliet, Partial and transient reduction of glycolysis by PFKFB3 blockade reduces pathological angiogenesis, Cell Metab. 19 (2014) 37–48. https://doi.org/10.1016/j.cmet.2013.11.008.

[99] B. Cruys, B.W. Wong, A. Kuchnio, D. Verdegem, A.R. Cantelmo, L.-C. Conradi, S. Vandekeere, A. Bouché, I. Cornelissen, S. Vinckier, R.M.H. Merks, E. Dejana, H. Gerhardt, M. Dewerchin, K. Bentley, P. Carmeliet, Glycolytic regulation of cell rearrangement in angiogenesis, Nat. Commun. 7 (2016) 12240. https://doi.org/10.1038/ncomms12240.

[100] A. Doddaballapur, K.M. Michalik, Y. Manavski, T. Lucas, R.H. Houtkooper, X. You, W. Chen, A.M. Zeiher, M. Potente, S. Dimmeler, R.A. Boon, Laminar shear stress inhibits endothelial cell metabolism via KLF2-mediated repression of PFKFB3, Arteriosclerosis, Thrombosis, and Vascular Biology 35 (2015) 137–145. https://doi.org/10.1161/ATVBAHA.114.304277.

[101] E. Roth, Nonnutritive effects of glutamine, J. Nutr. 138 (2008) 2025S-2031S. https://doi.org/10.1093/jn/138.10.2025S.

[102] J.R. Mayers, M.G. Vander Heiden, Famine versus feast: understanding the metabolism of tumors in vivo, Trends in Biochemical Sciences 40 (2015) 130–140. https://doi.org/10.1016/j.tibs.2015.01.004.

[103] T. Dorai, J.T. Pinto, T.T. Denton, B.F. Krasnikov, A.J.L. Cooper, The Metabolic Importance of the Glutaminase II Pathway in Normal and Cancerous Cells, Anal. Biochem. (2020) 114083. https://doi.org/10.1016/j.ab.2020.114083.

[104] D. Häussinger, F. Schliess, Glutamine metabolism and signaling in the liver, Front. Biosci. 12 (2007) 371–391. https://doi.org/10.2741/2070.

[105] D.R. Wise, R.J. DeBerardinis, A. Mancuso, N. Sayed, X.-Y. Zhang, H.K. Pfeiffer, I. Nissim, E. Daikhin, M. Yudkoff, S.B. McMahon, C.B. Thompson, Myc regulates a transcriptional program that stimulates mitochondrial glutaminolysis and leads to glutamine addiction, Proceedings of the National Academy of Sciences 105 (2008) 18782–18787. https://doi.org/10.1073/pnas.0810199105.

[106] N. Hay, Reprogramming glucose metabolism in cancer: can it be exploited for cancer therapy?, Nature Reviews Cancer 16 (2016) 635–649. https://doi.org/10.1038/nrc.2016.77.

[107] G. Eelen, C. Dubois, A.R. Cantelmo, J. Goveia, U. Brüning, M. DeRan, G. Jarugumilli, J. van Rijssel, G. Saladino, F. Comitani, A. Zecchin, S. Rocha, R. Chen, H. Huang, S. Vandekeere, J. Kalucka, C. Lange, F. Morales-Rodriguez, B. Cruys, L. Treps, L. Ramer, S. Vinckier, K. Brepoels, S. Wyns, J. Souffreau, L. Schoonjans, W.H. Lamers, Y. Wu, J. Haustraete, J. Hofkens, S. Liekens, R. Cubbon, B. Ghesquière, M. Dewerchin, F.L. Gervasio, X. Li, J.D. van Buul, X. Wu, P. Carmeliet, Role of glutamine synthetase in angiogenesis beyond glutamine synthesis, Nature 561 (2018) 63–69. https://doi.org/10.1038/s41586-018-0466-7.

[108] B. Leighton, R. Curi, A. Hussein, E.A. Newsholme, Maximum activities of some key enzymes of glycolysis, glutaminolysis, Krebs cycle and fatty acid utilization in bovine pulmonary endothelial cells, FEBS Letters 225 (1987) 93–96. https://doi.org/10.1016/0014-5793(87)81137-7.

[109] X. Li, X. Sun, P. Carmeliet, Hallmarks of Endothelial Cell Metabolism in Health and Disease, Cell Metab. 30 (2019) 414–433. https://doi.org/10.1016/j.cmet.2019.08.011.

[110] A.J.L. Cooper, T. Kuhara, α-Ketoglutaramate: an overlooked metabolite of glutamine and a biomarker for hepatic encephalopathy and inborn errors of the urea cycle, Metab. Brain Dis. 29 (2014) 991–1006. https://doi.org/10.1007/s11011-013-9444-9.

[111] A.J.L. Cooper, Y.I. Shurubor, T. Dorai, J.T. Pinto, E.P. Isakova, Y.I. Deryabina, T.T. Denton, B.F. Krasnikov, ω-Amidase: an underappreciated, but important enzyme in L-glutamine and L-asparagine metabolism; relevance to sulfur and nitrogen metabolism, tumor biology and hyperammonemic diseases, Amino Acids 48 (2016) 1–20. https://doi.org/10.1007/s00726-015-2061-7.

[112] L.B. Hersh, Rat liver omega-amidase. Purification and properties, Biochemistry 10 (1971) 2884–2891. https://doi.org/10.1021/bi00791a014.

[113] A.J.L. Cooper, T. Dorai, B. Dorai, B.F. Krasnikov, J. Li, A. Hallen, J.T. Pinto, Role of Glutamine Transaminases in Nitrogen, Sulfur, Selenium, and 1-Carbon Metabolism, in: R. Rajendram, V.R. Preedy, V.B. Patel (Eds.), Glutamine in Clinical Nutrition, first. Aufl., Humana Press, s.l., 2014, pp. 37–54.

[114] T. Otani, A. Meister, omega-Amide and omega-amino acid derivatives of alpha-ketoglutaric and oxalacetic acids, J. Biol. Chem. 224 (1957) 137–148.

[115] A. Meister, Preparation of enzymatic reactions of the keto analogues of asparagine and glutamine, J. Biol. Chem. 200 (1953) 571–589.

[116] B.F. Krasnikov, C.-H. Chien, R. Nostramo, J.T. Pinto, E. Nieves, M. Callaway, J. Sun, K. Huebner, A.J.L. Cooper, Identification of the putative tumor suppressor Nit2 as omega-amidase, an enzyme metabolically linked to glutamine and asparagine transamination, Biochimie 91 (2009) 1072–1080. https://doi.org/10.1016/j.biochi.2009.07.003.

[117] A.J. Cooper, T.E. Duffy, A. Meister, [45] α-keto acid ω-amidase from rat liver, in: A. Meister (Ed.), Glutamate, glutamine, glutathione, and related compounds, Academic Press, Orlando, Fla., 1985, pp. 350–358.

[118] D. Shen, L. Kruger, T. Deatherage, T.T. Denton, Synthesis of α-Ketoglutaramic acid, Anal. Biochem. 607 (2020) 113862. https://doi.org/10.1016/j.ab.2020.113862.

[119] J.T. Pinto, B.F. Krasnikov, S. Alcutt, M.E. Jones, T. Dorai, M.T. Villar, A. Artigues, J. Li, A.J.L. Cooper, Kynurenine aminotransferase III and glutamine transaminase L are identical enzymes that have cysteine S-conjugate β-lyase

activity and can transaminate L-selenomethionine, J. Biol. Chem. 289 (2014) 30950–30961. https://doi.org/10.1074/jbc.M114.591461.

[120] N. Plant, I. Kitchen, P.S. Goldfarb, G.G. Gibson, Developmental modulation of cysteine conjugate beta-lyase/glutamine transaminase K/kynurenine aminotransferase mRNA in rat brain, Eur. J. Drug Metab. Pharmacokinet. 22 (1997) 335–339. https://doi.org/10.1007/BF03190967.

[121] C. Yang, L. Zhang, Q. Han, C. Liao, J. Lan, H. Ding, H. Zhou, X. Diao, J. Li, Kynurenine aminotransferase 3/glutamine transaminase L/cysteine conjugate beta-lyase 2 is a major glutamine transaminase in the mouse kidney, Biochem. Biophys. Rep. 8 (2016) 234–241. https://doi.org/10.1016/j.bbrep.2016.09.008.

[122] Q. Han, J. Li, J. Li, pH dependence, substrate specificity and inhibition of human kynurenine aminotransferase I, Eur J Biochem 271 (2004) 4804–4814. https://doi.org/10.1111/j.1432-1033.2004.04446.x.

[123] Q. Han, H. Robinson, T. Cai, D.A. Tagle, J. Li, Biochemical and structural properties of mouse kynurenine aminotransferase III, Molecular and Cellular Biology 29 (2009) 784–793. https://doi.org/10.1128/MCB.01272-08.

[124] M. Mosca, Tissue expression and translational control of rat kynurenine aminotransferase/glutamine transaminase K mRNAs, Biochimica et Biophysica Acta (BBA) - Gene Structure and Expression 1628 (2003) 1–10. https://doi.org/10.1016/s0167-4781(03)00071-x.

[125] M. Mosca, L. Cozzi, J. Breton, C. Speciale, E. Okuno, R. Schwarcz, L. Benatti, Molecular cloning of rat kynurenine aminotransferase: Identity with glutamine transaminase K, FEBS Letters 353 (1994) 21–24. https://doi.org/10.1016/0014-5793(94)01003-X.

[126] A. Nematollahi, G. Sun, G.S. Jayawickrama, W.B. Church, Kynurenine Aminotransferase Isozyme Inhibitors: A Review, IJMS 17 (2016) 946. https://doi.org/10.3390/ijms17060946.

[127] P. Gaudet, M.S. Livstone, S.E. Lewis, P.D. Thomas, Phylogenetic-based propagation of functional annotations within the Gene Ontology consortium, Briefings in Bioinformatics 12 (2011) 449–462. https://doi.org/10.1093/bib/bbr042.

[128] A.C. Smith, A.J. Robinson, MitoMiner v3.1, an update on the mitochondrial proteomics database, Nucleic Acids Research 44 (2016) D1258-61. https://doi.org/10.1093/nar/gkv1001.

[129] S. Jaisson, M. Veiga-da-Cunha, E. van Schaftingen, Molecular identification of omega-amidase, the enzyme that is functionally coupled with glutamine transaminases, as the putative tumor suppressor Nit2, Biochimie 91 (2009) 1066–1071. https://doi.org/10.1016/j.biochi.2009.07.002.

[130] A.J.L. Cooper, T. Dorai, J.T. Pinto, T.T. Denton, The metabolic importance of the overlooked asparaginase II pathway, Anal. Biochem. (2020) 114084. https://doi.org/10.1016/j.ab.2020.114084.

[131] C.S. Silva Teixeira, S.F. Sousa, N.M.F.S.A. Cerqueira, An Unsual Cys-Glu-Lys Catalytic Triad is Responsible for the Catalytic Mechanism of the Nitrilase Superfamily: A QM/MM Study on Nit2, ChemPhysChem 22 (2021) 796–804. https://doi.org/10.1002/cphc.202000751.

[132] K.T. Barglow, K.S. Saikatendu, M.H. Bracey, R. Huey, G.M. Morris, A.J. Olson, R.C. Stevens, B.F. Cravatt, Functional proteomic and structural insights into molecular recognition in the nitrilase family enzymes, Biochemistry 47 (2008) 13514–13523. https://doi.org/10.1021/bi801786y.

[133] B.W. Weber, S.W. Kimani, A. Varsani, D.A. Cowan, R. Hunter, G.A. Venter, J.C. Gumbart, B.T. Sewell, The mechanism of the amidases: mutating the glutamate adjacent to the catalytic triad inactivates the enzyme due to substrate mispositioning, J. Biol. Chem. 288 (2013) 28514–28523. https://doi.org/10.1074/jbc.M113.503284.

[134] C.-H. Chien, Q.-Z. Gao, A.J.L. Cooper, J.-H. Lyu, S.-Y. Sheu, Structural insights into the catalytic active site and activity of human Nit2/ω-amidase: kinetic assay and molecular dynamics simulation, J. Biol. Chem. 287 (2012) 25715–25726. https://doi.org/10.1074/jbc.M111.259119.

[135] M.A. Avila, E.R. García-Trevijano, S.C. Lu, F.J. Corrales, J.M. Mato, Methylthioadenosine, Int. J. Biochem. Cell Biol. 36 (2004) 2125–2130. https://doi.org/10.1016/j.biocel.2003.11.016.

[136] E. Albers, Metabolic characteristics and importance of the universal methionine salvage pathway recycling methionine from 5'-methylthioadenosine, IUBMB Life 61 (2009) 1132–1142. https://doi.org/10.1002/iub.278.

[137] M. Sauter, B. Moffatt, M.C. Saechao, R. Hell, M. Wirtz, Methionine salvage and S-adenosylmethionine: essential links between sulfur, ethylene and polyamine biosynthesis, Biochemical Journal 451 (2013) 145–154. https://doi.org/10.1042/BJ20121744.

[138] Y. Dai, T.C. Pochapsky, R.H. Abeles, Mechanistic studies of two dioxygenases in the methionine salvage pathway of Klebsiella pneumoniae, Biochemistry 40 (2001) 6379–6387. https://doi.org/10.1021/bi010110y.

[139] J.W. Wray, R.H. Abeles, The methionine salvage pathway in Klebsiella pneumoniae and rat liver. Identification and characterization of two novel dioxygenases, Journal of Biological Chemistry 270 (1995) 3147–3153. https://doi.org/10.1074/jbc.270.7.3147.

[140] J.I. Durham, P.W. Morgan, J.M. Prescott, C.M. Lyman✠, An aminotransferase specific for the d-enantiomorph of methionine, Phytochemistry 12 (1973) 2123–2126. https://doi.org/10.1016/0031-9422(73)85109-X.

[141] K.W. Ellens, L.G.L. Richardson, O. Frelin, J. Collins, C.L. Ribeiro, Y.-F. Hsieh, R.T. Mullen, A.D. Hanson, Evidence that glutamine transaminase and omega-amidase potentially act in tandem to close the methionine salvage cycle in bacteria and plants, Phytochemistry 113 (2015) 160–169. https://doi.org/10.1016/j.phytochem.2014.04.012.

[142] T.E. Duffy, A.J. Cooper, A. Meister, Identification of α-Ketoglutaramate in Rat Liver, Kidney, and Brain, Journal of Biological Chemistry 249 (1974) 7603–7606. https://doi.org/10.1016/S0021-9258(19)81280-2.

[143] S. Udupa, S. Nguyen, G. Hoang, T. Nguyen, A. Quinones, K. Pham, R. Asaka, K. Nguyen, C. Zhang, A. Elgogary, J.G. Jung, Q. Xu, J. Fu, A.G. Thomas, T. Tsukamoto, J. Hanes, B.S. Slusher, A.J.L. Cooper, A. Le, Upregulation of the Glutaminase II Pathway Contributes to Glutamate Production upon Glutaminase 1 Inhibition in Pancreatic Cancer, Proteomics 19 (2019) e1800451. https://doi.org/10.1002/pmic.201800451.

[144] T. Dorai, B. Dorai, J.T. Pinto, M. Grasso, A.J.L. Cooper, High Levels of Glutaminase II Pathway Enzymes in Normal and Cancerous Prostate Suggest a Role in 'Glutamine Addiction', Biomolecules 10 (2019). https://doi.org/10.3390/biom10010002.

[145] P.J. Thul, L. Åkesson, M. Wiking, D. Mahdessian, A. Geladaki, H. Ait Blal, T. Alm, A. Asplund, L. Björk, L.M. Breckels, A. Bäckström, F. Danielsson, L. Fagerberg, J. Fall, L. Gatto, C. Gnann, S. Hober, M. Hjelmare, F. Johansson, S. Lee, C. Lindskog, J. Mulder, C.M. Mulvey, P. Nilsson, P. Oksvold, J. Rockberg, R. Schutten, J.M. Schwenk, Å. Sivertsson, E. Sjöstedt, M. Skogs, C. Stadler, D.P. Sullivan, H. Tegel, C. Winsnes, C. Zhang, M. Zwahlen, A. Mardinoglu, F. Pontén, K. von Feilitzen, K.S. Lilley, M. Uhlén, E. Lundberg, A subcellular map of the human proteome, Science 356 (2017) eaal3321. https://doi.org/10.1126/science.aal3321.

[146] C.-H. Lin, M.-Y. Chung, W.-B. Chen, C.-H. Chien, Growth inhibitory effect of the human NIT2 gene and its allelic imbalance in cancers, FEBS Journal 274 (2007) 2946–2956. https://doi.org/10.1111/j.1742-4658.2007.05828.x.

[147] S. Chen, Z. Wang, C. Feng, NIT2 overexpression predicts poor prognosis in tongue squamous cell carcinoma patients, Mol Biol Rep 47 (2020) 1553–1561. https://doi.org/10.1007/s11033-019-05197-5.

[148] L. Pollegioni, L. Piubelli, S. Sacchi, M.S. Pilone, G. Molla, Physiological functions of D-amino acid oxidases: from yeast to humans, Cell. Mol. Life Sci. 64 (2007) 1373–1394. https://doi.org/10.1007/s00018-007-6558-4.

[149] M.J. Cline, R.I. Lehrer, D-amino acid oxidase in leukocytes: a possible D-amino-acid-linked antimicrobial system, Proc. Natl. Acad. Sci. U. S. A. 62 (1969) 756–763. https://doi.org/10.1073/pnas.62.3.756.

[150] L. Valon, A. Marín-Llauradó, T. Wyatt, G. Charras, X. Trepat, Optogenetic control of cellular forces and mechanotransduction, Nat. Commun. 8 (2017) 14396. https://doi.org/10.1038/ncomms14396.

[151] J.J. Almagro Armenteros, M. Salvatore, O. Emanuelsson, O. Winther, G. von Heijne, A. Elofsson, H. Nielsen, Detecting sequence signals in targeting peptides using deep learning, Life Sci. Alliance 2 (2019). https://doi.org/10.26508/lsa.201900429.

[152] X. Chen, M. Rinsma, J.M. Janssen, J. Liu, I. Maggio, M.A.F.V. Gonçalves, Probing the impact of chromatin conformation on genome editing tools, Nucleic Acids Research 44 (2016) 6482–6492. https://doi.org/10.1093/nar/gkw524.

[153] D.B. Kuhns, D.A.L. Priel, J. Chu, K.A. Zarember, Isolation and Functional Analysis of Human Neutrophils, Curr. Protoc. Immunol. 111 (2015) 7.23.1-7.23.16. https://doi.org/10.1002/0471142735.im0723s111.

[154] N.E. Sanjana, O. Shalem, F. Zhang, Improved vectors and genome-wide libraries for CRISPR screening, Nat. Methods 11 (2014) 783–784. https://doi.org/10.1038/nmeth.3047.

[155] B. Ma, K. Zhang, C. Hendrie, C. Liang, M. Li, A. Doherty-Kirby, G. Lajoie, PEAKS: powerful software for peptide de novo sequencing by tandem mass spectrometry, Rapid Commun. Mass Spectrom. 17 (2003) 2337–2342. https://doi.org/10.1002/rcm.1196.

[156] J. Rappsilber, M. Mann, Y. Ishihama, Protocol for micro-purification, enrichment, pre-fractionation and storage of peptides for proteomics using StageTips, Nat Protoc 2 (2007) 1896–1906. https://doi.org/10.1038/nprot.2007.261.

[157] J. Cox, M. Mann, MaxQuant enables high peptide identification rates, individualized p.p.b.-range mass accuracies and proteome-wide protein quantification, Nat. Biotechnol. 26 (2008) 1367–1372. https://doi.org/10.1038/nbt.1511.

[158] S. Tyanova, T. Temu, P. Sinitcyn, A. Carlson, M.Y. Hein, T. Geiger, M. Mann, J. Cox, The Perseus computational platform for comprehensive analysis of (prote)omics data, Nat. Methods 13 (2016) 731–740. https://doi.org/10.1038/nmeth.3901.

[159] B.F. Krasnikov, R. Nostramo, J.T. Pinto, A.J.L. Cooper, Assay and purification of omega-amidase/Nit2, a ubiquitously expressed putative tumor suppressor, that catalyzes the deamidation of the alpha-keto acid analogues of glutamine and asparagine, Anal. Biochem. 391 (2009) 144–150. https://doi.org/10.1016/j.ab.2009.05.025.

[160] F.H. Niesen, H. Berglund, M. Vedadi, The use of differential scanning fluorimetry to detect ligand interactions that promote protein stability, Nat. Protoc. 2 (2007) 2212–2221. https://doi.org/10.1038/nprot.2007.321.

[161] J.S. Kramer, S. Woltersdorf, T. Duflot, K. Hiesinger, F.F. Lillich, F. Knöll, S.K. Wittmann, F.-M. Klingler, S. Brunst, A. Chaikuad, C. Morisseau, B.D. Hammock, C. Buccellati, A. Sala, G.E. Rovati, M. Leuillier, S. Fraineau, J. Rondeaux, V.

Hernandez-Olmos, J. Heering, D. Merk, D. Pogoryelov, D. Steinhilber, S. Knapp, J. Bellien, E. Proschak, Discovery of the First in Vivo Active Inhibitors of the Soluble Epoxide Hydrolase Phosphatase Domain, J. Med. Chem. 62 (2019) 8443–8460. https://doi.org/10.1021/acs.jmedchem.9b00445.

[162] O. Löwe, F. Rezende, J. Heidler, I. Wittig, V. Helfinger, R.P. Brandes, K. Schröder, BIAM switch assay coupled to mass spectrometry identifies novel redox targets of NADPH oxidase 4, Redox Biol. 21 (2019) 101125. https://doi.org/10.1016/j.redox.2019.101125.

[163] F. Al-Khelaifi, I. Diboun, F. Donati, F. Botrè, M. Alsayrafi, C. Georgakopoulos, K. Suhre, N.A. Yousri, M.A. Elrayess, A pilot study comparing the metabolic profiles of elite-level athletes from different sporting disciplines, Sports Med. Open 4 (2018) 2. https://doi.org/10.1186/s40798-017-0114-z.

[164] A.M. Evans, C.D. DeHaven, T. Barrett, M. Mitchell, E. Milgram, Integrated, nontargeted ultrahigh performance liquid chromatography/electrospray ionization tandem mass spectrometry platform for the identification and relative quantification of the small-molecule complement of biological systems, Anal. Chem. 81 (2009) 6656–6667. https://doi.org/10.1021/ac901536h.

[165] B.R. Bridgewater, High Resolution Mass Spectrometry Improves Data Quantity and Quality as Compared to Unit Mass Resolution Mass Spectrometry in High-Throughput Profiling Metabolomics, Metabolomics 04 (2014). https://doi.org/10.4172/2153-0769.1000132.

[166] K.L. Howe, B. Contreras-Moreira, N. de Silva, G. Maslen, W. Akanni, J. Allen, J. Alvarez-Jarreta, M. Barba, D.M. Bolser, L. Cambell, M. Carbajo, M. Chakiachvili, M. Christensen, C. Cummins, A. Cuzick, P. Davis, S. Fexova, A. Gall, N. George, L. Gil, P. Gupta, K.E. Hammond-Kosack, E. Haskell, S.E. Hunt, P. Jaiswal, S.H. Janacek, P.J. Kersey, N. Langridge, U. Maheswari, T. Maurel, M.D. McDowall, B. Moore, M. Muffato, G. Naamati, S. Naithani, A. Olson, I. Papatheodorou, M. Patricio, M. Paulini, H. Pedro, E. Perry, J. Preece, M. Rosello, M. Russell, V. Sitnik, D.M. Staines, J. Stein, M.K. Tello-Ruiz, S.J. Trevanion, M. Urban, S. Wei, D. Ware, G. Williams, A.D. Yates, P. Flicek, Ensembl Genomes 2020-enabling non-vertebrate genomic research, Nucleic Acids Research 48 (2020) D689-D695. https://doi.org/10.1093/nar/gkz890.

[167] R. Patro, G. Duggal, M.I. Love, R.A. Irizarry, C. Kingsford, Salmon provides fast and bias-aware quantification of transcript expression, Nat Methods 14 (2017) 417–419. https://doi.org/10.1038/nmeth.4197.

[168] M.I. Love, W. Huber, S. Anders, Moderated estimation of fold change and dispersion for RNA-seq data with DESeq2, Genome Biol 15 (2014) 550. https://doi.org/10.1186/s13059-014-0550-8.

[169] T. Wu, E. Hu, S. Xu, M. Chen, P. Guo, Z. Dai, T. Feng, L. Zhou, W. Tang, L. Zhan, X. Fu, S. Liu, X. Bo, G. Yu, clusterProfiler 4.0: A universal enrichment tool for interpreting omics data, The Innovation 2 (2021) 100141. https://doi.org/10.1016/j.xinn.2021.100141.

[170] H. Wickham, ggplot2, WIREs Comp Stat 3 (2011) 180–185. https://doi.org/10.1002/wics.147.

[171] T. Korff, H.G. Augustin, Integration of endothelial cells in multicellular spheroids prevents apoptosis and induces differentiation, J. Cell Biol. 143 (1998) 1341–1352. https://doi.org/10.1083/jcb.143.5.1341.

[172] J. Browning, M. Rooney, E. Hams, S. Takahashi, S. Mizuno, F. Sugiyama, P.G. Fallon, V.P. Kelly, Highly efficient CRISPR-targeting of the murine Hipp11 intergenic region supports inducible human transgene expression, Mol Biol Rep 47 (2020) 1491–1498. https://doi.org/10.1007/s11033-019-05204-9.

[173] M.L. Fehrenbach, G. Cao, J.T. Williams, J.M. Finklestein, H.M. Delisser, Isolation of murine lung endothelial cells, Am. J. Physiol. Lung Cell. Mol. Physiol. 296 (2009) L1096-103. https://doi.org/10.1152/ajplung.90613.2008.

[174] K.T. Barglow, K.S. Saikatendu, R.C. Stevens, B.F. Cravatt, Crystal structure of mouse nitrilase-2 at 1.4A resolution, 2008.

[175] M. Keßler, I. Wittig, J. Ackermann, I. Koch, 2021. Prediction and analysis of redox-sensitive cysteines using machine learning and statistical methods. Biological Chemistry 0, 000010151520200321. https://doi.org/10.1515/hsz-2020-0321.

[176] L. Pollegioni, B. Langkau, W. Tischer, S. Ghisla, M.S. Pilone, Kinetic mechanism of D-amino acid oxidases from Rhodotorula gracilis and Trigonopsis variabilis, Journal of Biological Chemistry 268 (1993) 13850–13857. https://doi.org/10.1016/S0021-9258(19)85181-5.

[177] N. Müller, T. Warwick, K. Noack, P.F. Malacarne, A.J.L. Cooper, N. Weissmann, K. Schröder, R.P. Brandes, F. Rezende, Reactive Oxygen Species Differentially Modulate the Metabolic and Transcriptomic Response of Endothelial Cells, Antioxidants 11 (2022) 434. https://doi.org/10.3390/antiox11020434.

[178] S.G. Rhee, Overview on Peroxiredoxin, Molecules and Cells 39 (2016) 1–5. https://doi.org/10.14348/molcells.2016.2368.

[179] J.C. Lim, H.-I. Choi, Y.S. Park, H.W. Nam, H.A. Woo, K.-S. Kwon, Y.S. Kim, S.G. Rhee, K. Kim, H.Z. Chae, Irreversible oxidation of the active-site cysteine of peroxiredoxin to cysteine sulfonic acid for enhanced molecular chaperone activity, Journal of Biological Chemistry 283 (2008) 28873–28880. https://doi.org/10.1074/jbc.M804087200.

[180] G. Loor, J. Kondapalli, J.M. Schriewer, N.S. Chandel, T.L. Vanden Hoek, P.T. Schumacker, Menadione triggers cell death through ROS-dependent mechanisms involving PARP activation without requiring apoptosis, Free Radic. Biol. Med. 49 (2010) 1925–1936. https://doi.org/10.1016/j.freeradbiomed.2010.09.021.

[181] V.V. Pak, D. Ezeriņa, O.G. Lyublinskaya, B. Pedre, P.A. Tyurin-Kuzmin, N.M. Mishina, M. Thauvin, D. Young, K. Wahni, S.A. Martínez Gache, A.D. Demidovich, Y.G. Ermakova, Y.D. Maslova, A.G. Shokhina, E. Eroglu, D.S. Bilan, I. Bogeski, T. Michel, S. Vriz, J. Messens, V.V. Belousov, Ultrasensitive Genetically Encoded Indicator for Hydrogen Peroxide Identifies Roles for the Oxidant in Cell Migration and Mitochondrial Function, Cell Metab. 31 (2020) 642-653.e6. https://doi.org/10.1016/j.cmet.2020.02.003.

[182] J.D. Braun, D.O. Pastene, A. Breedijk, A. Rodriguez, B.B. Hofmann, C. Sticht, E. von Ochsenstein, H. Allgayer, J. van den Born, S. Bakker, S.J. Hauske, B.K. Krämer, B.A. Yard, T. Albrecht, Methylglyoxal down-regulates the expression of cell cycle associated genes and activates the p53 pathway in human umbilical vein endothelial cells, Sci Rep 9 (2019) 1152. https://doi.org/10.1038/s41598-018-37937-1.

[183] A. Kuehne, H. Emmert, J. Soehle, M. Winnefeld, F. Fischer, H. Wenck, S. Gallinat, L. Terstegen, R. Lucius, J. Hildebrand, N. Zamboni, Acute Activation of Oxidative Pentose Phosphate Pathway as First-Line Response to Oxidative

Stress in Human Skin Cells, Mol. Cell 59 (2015) 359–371. https://doi.org/10.1016/j.molcel.2015.06.017.

[184] K.V. Barinova, M.V. Serebryakova, V.I. Muronetz, E.V. Schmalhausen, S-glutathionylation of glyceraldehyde-3-phosphate dehydrogenase induces formation of C150-C154 intrasubunit disulfide bond in the active site of the enzyme, Biochimica et Biophysica Acta (BBA) - General Subjects 1861 (2017) 3167–3177. https://doi.org/10.1016/j.bbagen.2017.09.008.

[185] P.R. Gardner, Aconitase: Sensitive target and measure of superoxide, in: L. Packer (Ed.), Superoxide dismutase, Academic Press, San Diego, 2002, pp. 9–23.

[186] L.A. McDermott, P. Iyer, L. Vernetti, S. Rimer, J. Sun, M. Boby, T. Yang, M. Fioravanti, J. O'Neill, L. Wang, D. Drakes, W. Katt, Q. Huang, R. Cerione, Design and evaluation of novel glutaminase inhibitors, Bioorg. Med. Chem. 24 (2016) 1819–1839. https://doi.org/10.1016/j.bmc.2016.03.009.

[187] A.J. Cooper, M.T. Haber, A. Meister, On the chemistry and biochemistry of 3-mercaptopyruvic acid, the alpha-keto acid analog of cysteine, Journal of Biological Chemistry 257 (1982) 816–826. https://doi.org/10.1016/S0021-9258(19)68270-0.

[188] F. Vergara, F. Plum, T.E. Duffy, Alpha-ketoglutaramate: increased concentrations in the cerebrospinal fluid of patients in hepatic coma, Science 183 (1974) 81–83. https://doi.org/10.1126/science.183.4120.81.

[189] T. Kuhara, Y. Inoue, M. Ohse, B.F. Krasnikov, A.J.L. Cooper, Urinary 2-hydroxy-5-oxoproline, the lactam form of α-ketoglutaramate, is markedly increased in urea cycle disorders, Anal Bioanal Chem 400 (2011) 1843–1851. https://doi.org/10.1007/s00216-011-4688-x.

[190] D. in Kim, S.C. Jensen, K.A. Noble, B. KC, K.H. Roux, K. Motamedchaboki, K.J. Roux, An improved smaller biotin ligase for BioID proximity labeling, MBoC 27 (2016) 1188–1196. https://doi.org/10.1091/mbc.E15-12-0844.

[191] A.C. Cavanagh, H. Morton, The purification of early-pregnancy factor to homogeneity from human platelets and identification as chaperonin 10, Eur J Biochem 222 (1994) 551–560. https://doi.org/10.1111/j.1432-1033.1994.tb18897.x.

[192] P.V. Viitanen, G.H. Lorimer, R. Seetharam, R.S. Gupta, J. Oppenheim, J.O. Thomas, N.J. Cowan, Mammalian mitochondrial chaperonin 60 functions as a single toroidal ring, Journal of Biological Chemistry 267 (1992) 695–698. https://doi.org/10.1016/S0021-9258(18)48338-X.

[193] A.J.L. Cooper, T.M. Jeitner, Central Role of Glutamate Metabolism in the Maintenance of Nitrogen Homeostasis in Normal and Hyperammonemic Brain, Biomolecules 6 (2016). https://doi.org/10.3390/biom6020016.

[194] A.A. Starkov, G. Fiskum, C. Chinopoulos, B.J. Lorenzo, S.E. Browne, M.S. Patel, M.F. Beal, Mitochondrial alpha-ketoglutarate dehydrogenase complex generates reactive oxygen species, Journal of Neuroscience 24 (2004) 7779–7788. https://doi.org/10.1523/JNEUROSCI.1899-04.2004.

[195] S.S. Saeedi Saravi, E. Eroglu, M. Waldeck-Weiermair, A. Sorrentino, B. Steinhorn, V. Belousov, T. Michel, Differential endothelial signaling responses elicited by chemogenetic H2O2 synthesis, Redox Biol. 36 (2020) 101605. https://doi.org/10.1016/j.redox.2020.101605.

[196] B. Steinhorn, A. Sorrentino, S. Badole, Y. Bogdanova, V. Belousov, T. Michel, Chemogenetic generation of hydrogen peroxide in the heart induces severe cardiac dysfunction, Nat. Commun. 9 (2018) 4044. https://doi.org/10.1038/s41467-018-06533-2.

[197] D. Anastasiou, G. Poulogiannis, J.M. Asara, M.B. Boxer, J. Jiang, M. Shen, G. Bellinger, A.T. Sasaki, J.W. Locasale, D.S. Auld, C.J. Thomas, M.G. Vander Heiden, L.C. Cantley, Inhibition of pyruvate kinase M2 by reactive oxygen species contributes to cellular antioxidant responses, Science 334 (2011) 1278–1283. https://doi.org/10.1126/science.1211485.

[198] M. Ralser, M.M. Wamelink, A. Kowald, B. Gerisch, G. Heeren, E.A. Struys, E. Klipp, C. Jakobs, M. Breitenbach, H. Lehrach, S. Krobitsch, Dynamic rerouting of the carbohydrate flux is key to counteracting oxidative stress, J Biol 6 (2007) 10. https://doi.org/10.1186/jbiol61.

[199] M. Ralser, M.M.C. Wamelink, S. Latkolik, E.E.W. Jansen, H. Lehrach, C. Jakobs, Metabolic reconfiguration precedes transcriptional regulation in the antioxidant response, Nat. Biotechnol. 27 (2009) 604–605. https://doi.org/10.1038/nbt0709-604.

[200] C. Colussi, M.C. Albertini, S. Coppola, S. Rovidati, F. Galli, L. Ghibelli, H2O2-induced block of glycolysis as an active ADP-ribosylation reaction protecting cells from apoptosis, FASEB J. 14 (2000) 2266–2276. https://doi.org/10.1096/fj.00-0074com.

[201] E. Panieri, M.M. Santoro, ROS signaling and redox biology in endothelial cells, Cell. Mol. Life Sci. 72 (2015) 3281–3303. https://doi.org/10.1007/s00018-015-1928-9.

[202] J. Kalucka, L. Bierhansl, N.V. Conchinha, R. Missiaen, I. Elia, U. Brüning, S. Scheinok, L. Treps, A.R. Cantelmo, C. Dubois, P. de Zeeuw, J. Goveia, A. Zecchin, F. Taverna, F. Morales-Rodriguez, A. Brajic, L.-C. Conradi, S. Schoors, U. Harjes, K. Vriens, G.-A. Pilz, R. Chen, R. Cubbon, B. Thienpont, B. Cruys, B.W. Wong, B. Ghesquière, M. Dewerchin, K. de Bock, X. Sagaert, S. Jessberger, E.A.V. Jones, B. Gallez, D. Lambrechts, M. Mazzone, G. Eelen, X. Li, S.-M. Fendt, P. Carmeliet, Quiescent Endothelial Cells Upregulate Fatty Acid β-Oxidation for Vasculoprotection via Redox Homeostasis, Cell Metab. 28 (2018) 881-894.e13. https://doi.org/10.1016/j.cmet.2018.07.016.

[203] K. Beyfuss, D.A. Hood, A systematic review of p53 regulation of oxidative stress in skeletal muscle, Redox Rep. 23 (2018) 100–117. https://doi.org/10.1080/13510002.2017.1416773.

[204] N. Shcherbik, D.G. Pestov, The Impact of Oxidative Stress on Ribosomes: From Injury to Regulation, Cells 8 (2019) 1379. https://doi.org/10.3390/cells8111379.

[205] M.V. Gerashchenko, A.V. Lobanov, V.N. Gladyshev, Genome-wide ribosome profiling reveals complex translational regulation in response to oxidative stress, Proceedings of the National Academy of Sciences 109 (2012) 17394–17399. https://doi.org/10.1073/pnas.1120799109.

[206] Z.G. Jin, M.G. Melaragno, D.F. Liao, C. Yan, J. Haendeler, Y.A. Suh, J.D. Lambeth, B.C. Berk, Cyclophilin A is a secreted growth factor induced by oxidative stress, Circulation Research 87 (2000) 789–796. https://doi.org/10.1161/01.res.87.9.789.

[207] A. Blanc, N. Pandey, A. Srivastava, Synchronous activation of ERK 1/2, p38mapk and PKB/Akt signaling by H2O2 in vascular smooth muscle cells:

Potential involvement in vascular disease (Review), Int J Mol Med (2003). https://doi.org/10.3892/ijmm.11.2.229.

[208] L. Jin, D. Li, G.N. Alesi, J. Fan, H.-B. Kang, Z. Lu, T.J. Boggon, P. Jin, H. Yi, E.R. Wright, D. Duong, N.T. Seyfried, R. Egnatchik, R.J. DeBerardinis, K.R. Magliocca, C. He, M.L. Arellano, H.J. Khoury, D.M. Shin, F.R. Khuri, S. Kang, Glutamate dehydrogenase 1 signals through antioxidant glutathione peroxidase 1 to regulate redox homeostasis and tumor growth, Cancer Cell 27 (2015) 257–270. https://doi.org/10.1016/j.ccell.2014.12.006.

[209] C.A. Fuentes-Almagro, M.-J. Prieto-Álamo, C. Pueyo, J. Jurado, Identification of proteins containing redox-sensitive thiols after PRDX1, PRDX3 and GCLC silencing and/or glucose oxidase treatment in Hepa 1-6 cells, Journal of Proteomics 77 (2012) 262–279. https://doi.org/10.1016/j.jprot.2012.08.025.

[210] S. Liu, L. He, K. Yao, The Antioxidative Function of Alpha-Ketoglutarate and Its Applications, Biomed Res. Int. 2018 (2018) 3408467. https://doi.org/10.1155/2018/3408467.

[211] Y. Chen, W.G. Junger, Measurement of oxidative burst in neutrophils, Methods Mol. Biol. 844 (2012) 115–124. https://doi.org/10.1007/978-1-61779-527-5_8.

[212] T. Kuhara, M. Ohse, Y. Inoue, A.J.L. Cooper, A GC/MS-based metabolomic approach for diagnosing citrin deficiency, Anal Bioanal Chem 400 (2011) 1881–1894. https://doi.org/10.1007/s00216-011-4766-0.

[213] R.F. Butterworth, Hepatic encephalopathy: a central neuroinflammatory disorder?, Hepatology 53 (2011) 1372–1376. https://doi.org/10.1002/hep.24228.

[214] L.B. Poole, The basics of thiols and cysteines in redox biology and chemistry, Free Radic. Biol. Med. 80 (2015) 148–157. https://doi.org/10.1016/j.freeradbiomed.2014.11.013.

[215] L.B. Poole, K.J. Nelson, Discovering mechanisms of signaling-mediated cysteine oxidation, Curr. Opin. Chem. Biol. 12 (2008) 18–24. https://doi.org/10.1016/j.cbpa.2008.01.021.

[216] R. Requejo, T.R. Hurd, N.J. Costa, M.P. Murphy, Cysteine residues exposed on protein surfaces are the dominant intramitochondrial thiol and may protect against oxidative damage, The FEBS Journal 277 (2010) 1465–1480. https://doi.org/10.1111/j.1742-4658.2010.07576.x.

[217] A.R. Cantelmo, L.-C. Conradi, A. Brajic, J. Goveia, J. Kalucka, A. Pircher, P. Chaturvedi, J. Hol, B. Thienpont, L.-A. Teuwen, S. Schoors, B. Boeckx, J. Vriens, A. Kuchnio, K. Veys, B. Cruys, L. Finotto, L. Treps, T.E. Stav-Noraas, F. Bifari, P. Stapor, I. Decimo, K. Kampen, K. de Bock, G. Haraldsen, L. Schoonjans, T. Rabelink, G. Eelen, B. Ghesquière, J. Rehman, D. Lambrechts, A.B. Malik, M. Dewerchin, P. Carmeliet, Inhibition of the Glycolytic Activator PFKFB3 in Endothelium Induces Tumor Vessel Normalization, Impairs Metastasis, and Improves Chemotherapy, Cancer Cell 30 (2016) 968–985. https://doi.org/10.1016/j.ccell.2016.10.006.

[218] L. Jakobsson, C.A. Franco, K. Bentley, R.T. Collins, B. Ponsioen, I.M. Aspalter, I. Rosewell, M. Busse, G. Thurston, A. Medvinsky, S. Schulte-Merker, H. Gerhardt, Endothelial cells dynamically compete for the tip cell position during angiogenic sprouting, Nature Cell Biology 12 (2010) 943–953. https://doi.org/10.1038/ncb2103.

[219] K. Bentley, G. Mariggi, H. Gerhardt, P.A. Bates, Tipping the balance: robustness of tip cell selection, migration and fusion in angiogenesis, PLoS Comput. Biol. 5 (2009) e1000549. https://doi.org/10.1371/journal.pcbi.1000549.

[220] J.-H. Lee, D.H. Bhang, A. Beede, T.L. Huang, B.R. Stripp, K.D. Bloch, A.J. Wagers, Y.-H. Tseng, S. Ryeom, C.F. Kim, Lung stem cell differentiation in mice directed by endothelial cells via a BMP4-NFATc1-thrombospondin-1 axis, Cell 156 (2014) 440–455. https://doi.org/10.1016/j.cell.2013.12.039.

[221] T. Han, de Kang, D. Ji, X. Wang, W. Zhan, M. Fu, H.-B. Xin, J.-B. Wang, How does cancer cell metabolism affect tumor migration and invasion?, Cell Adh. Migr. 7 (2013) 395–403. https://doi.org/10.4161/cam.26345.

[222] M. Parri, P. Chiarugi, Redox molecular machines involved in tumor progression, Antioxidants & Redox Signaling 19 (2013) 1828–1845. https://doi.org/10.1089/ars.2012.5040.

[223] H.Q. Smith, C. Li, C.A. Stanley, T.J. Smith, Glutamate Dehydrogenase, a Complex Enzyme at a Crucial Metabolic Branch Point, Neurochem Res 44 (2019) 117–132. https://doi.org/10.1007/s11064-017-2428-0.

[224] J.E. Miller, G. Litwack, Purification, Properties, and Identity of Liver Mitochondrial Tyrosine Aminotransferase, Journal of Biological Chemistry 246 (1971) 3234–3240. https://doi.org/10.1016/S0021-9258(18)62219-7.

[225] E. Shrawder, M. Martinez-Carrion, Evidence of Phenylalanine Transaminase Activity in the Isoenzymes of Aspartate Transaminase, Journal of Biological Chemistry 247 (1972) 2486–2492. https://doi.org/10.1016/S0021-9258(19)45454-9.

[226] J. Pérez-Escuredo, V.F. van Hée, M. Sboarina, J. Falces, V.L. Payen, L. Pellerin, P. Sonveaux, Monocarboxylate transporters in the brain and in cancer, Biochim. Biophys. Acta 1863 (2016) 2481–2497. https://doi.org/10.1016/j.bbamcr.2016.03.013.

[227] C. Guo, T. Huang, Q.-H. Wang, H. Li, A. Khanal, E.-H. Kang, W. Zhang, H.-T. Niu, Z. Dong, Y.-W. Cao, Monocarboxylate transporter 1 and monocarboxylate transporter 4 in cancer-endothelial co-culturing microenvironments promote proliferation, migration, and invasion of renal cancer cells, Cancer Cell Int. 19 (2019) 170. https://doi.org/10.1186/s12935-019-0889-8.

[228] L. Rochette, A. Meloux, M. Zeller, G. Malka, Y. Cottin, C. Vergely, Mitochondrial SLC25 Carriers: Novel Targets for Cancer Therapy, Molecules 25 (2020). https://doi.org/10.3390/molecules25102417.

[229] J. Wang, Y. Cui, Z. Yu, W. Wang, X. Cheng, W. Ji, S. Guo, Q. Zhou, N. Wu, Y. Chen, Y. Chen, X. Song, H. Jiang, Y. Wang, Y. Lan, B. Zhou, L. Mao, J. Li, H. Yang, W. Guo, X. Yang, Brain Endothelial Cells Maintain Lactate Homeostasis and Control Adult Hippocampal Neurogenesis, Cell Stem Cell 25 (2019) 754-767.e9. https://doi.org/10.1016/j.stem.2019.09.009.

[230] F. Palmieri, The mitochondrial transporter family SLC25: identification, properties and physiopathology, Mol. Aspects Med. 34 (2013) 465–484. https://doi.org/10.1016/j.mam.2012.05.005.

9. Appendix

9.1 Supplementary figures

Figure 43. Vector map of pLVX2-hDAO

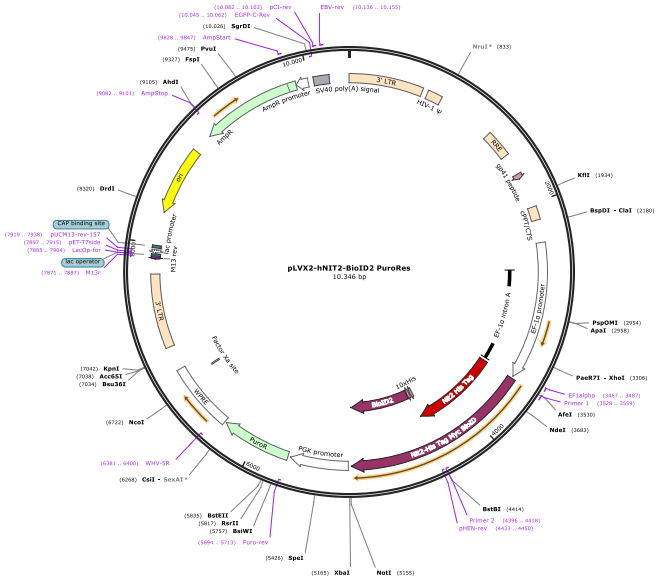

Figure 44. Vector map of pLVX-hNIT2-BioID2

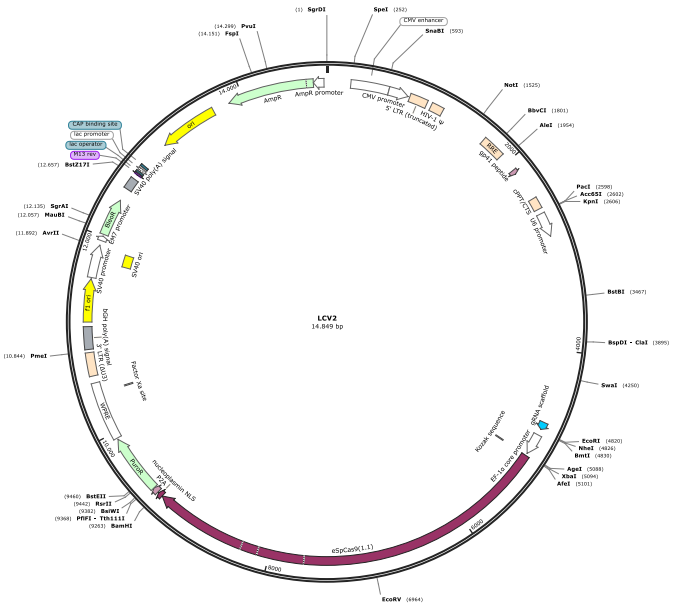

Figure 46. Vector map of LCV2

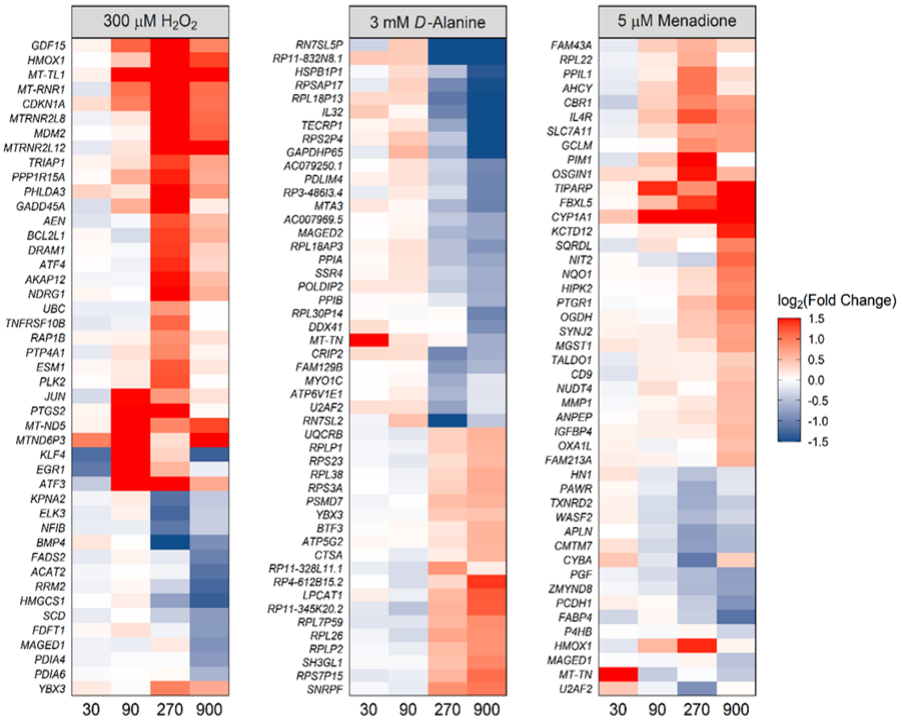

Figure 45. Heat map of DEGs after exposure to different types of ROS

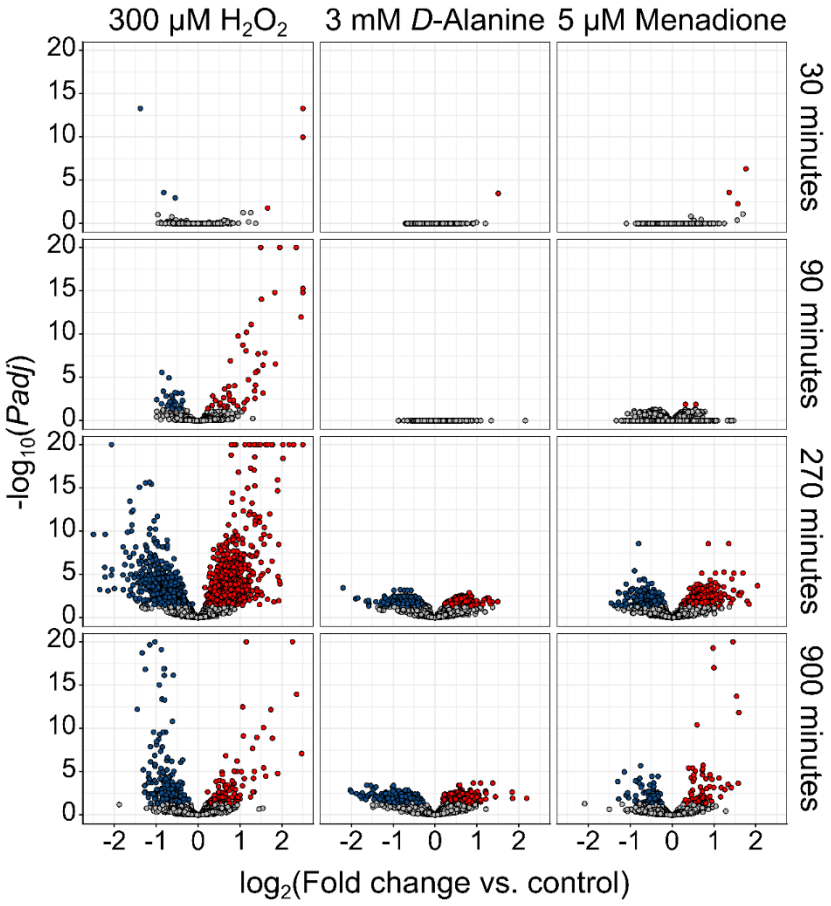

Figure 47. Volcano plot of DEGs (p_{adj} < 0.05) after exposure to different types of ROS

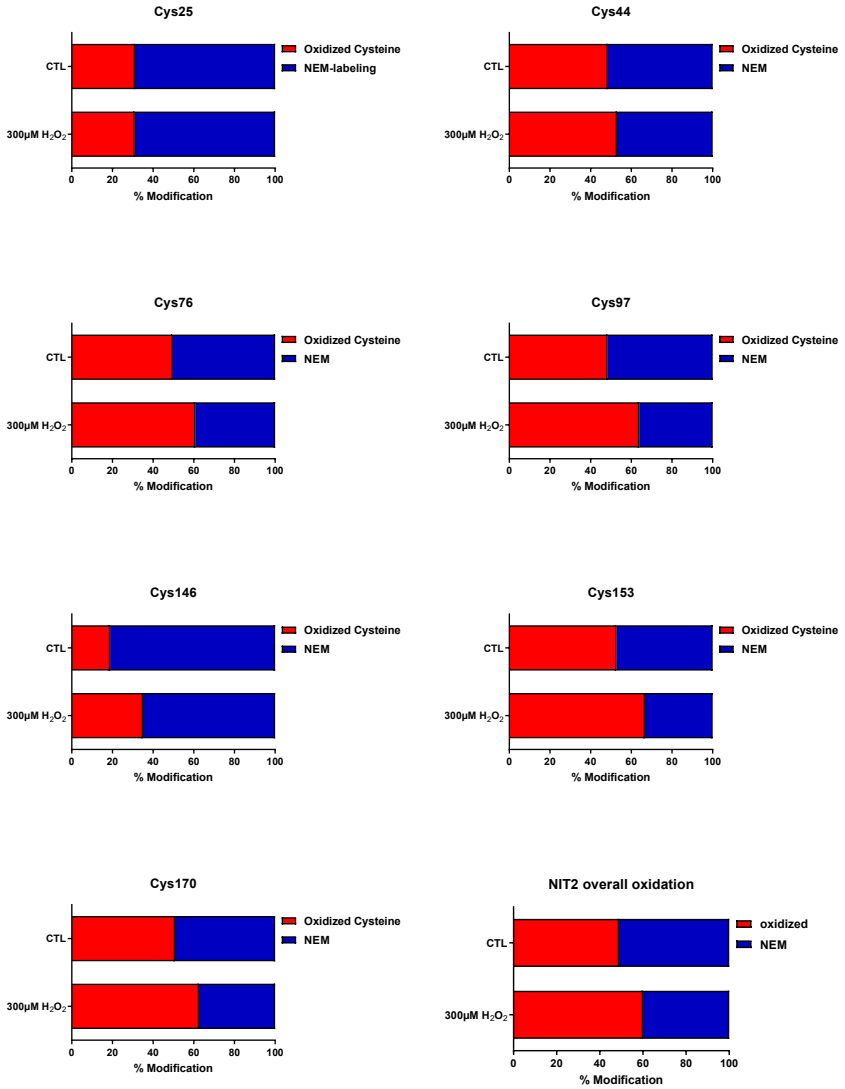

Figure 48. Modified cysteines in NIT2 detected by MS

9.2 Supplementary tables

Table 23. Pathway enrichment analysis of MACE-Seq data

Treatment	Enrichment	logP	Label	Count
3mM_DAla_vs_CTL	5,397233584	23,66409863	Ribosome	55
3mM_DAla_vs_CTL	3,608871234	14,3872219	Coronavirus disease - COVID-19	54
3mM_DAla_vs_CTL	2,506411823	5,833022009	Parkinson disease	43
3mM_DAla_vs_CTL	4,027215614	5,418013232	Bacterial invasion of epithelial cells	20
3mM_DAla_vs_CTL	3,124097486	5,299587052	Oxidative phosphorylation	27
3mM_DAla_vs_CTL	2,129777488	4,963236395	Amyotrophic lateral sclerosis	50
3mM_DAla_vs_CTL	2,059228609	4,691177229	Alzheimer disease	51
3mM_DAla_vs_CTL	2,322578398	4,387013145	Shigellosis	37
3mM_DAla_vs_CTL	2,214968588	4,219823171	Prion disease	39
3mM_DAla_vs_CTL	2,363957506	4,219823171	Chemical carcinogenesis - reactive oxygen species	34
300uM_H2O2_vs_CTL	2,593931362	12,67841908	Ribosome	70
300uM_H2O2_vs_CTL	2,044158471	8,448729934	Coronavirus disease - COVID-19	81
300uM_H2O2_vs_CTL	1,785414766	8,068228214	Amyotrophic lateral sclerosis	111
300uM_H2O2_vs_CTL	1,804885861	5,927747206	Parkinson disease	82
300uM_H2O2_vs_CTL	2,646723703	5,927747206	p53 signaling pathway	33
300uM_H2O2_vs_CTL	1,817029752	5,331420644	Thermogenesis	72
300uM_H2O2_vs_CTL	2,137493553	5,295428779	Cell cycle	46
300uM_H2O2_vs_CTL	1,951624549	5,265100941	Protein processing in endoplasmic reticulum	57
300uM_H2O2_vs_CTL	1,819758025	5,265100941	Human T-cell leukemia virus 1 infection	69
300uM_H2O2_vs_CTL	1,585694946	4,974253863	Alzheimer disease	104
5uM_Menadione_vs_CTL	4,235570645	5,961045312	Bacterial invasion of epithelial cells	22
5uM_Menadione_vs_CTL	2,560053743	5,946001016	Salmonella infection	43
5uM_Menadione_vs_CTL	2,533300164	3,337445189	Ribosome	27
5uM_Menadione_vs_CTL	2,332788909	3,337445189	Pathogenic Escherichia coli infection	31
5uM_Menadione_vs_CTL	2,117785323	3,337445189	Parkinson disease	38
5uM_Menadione_vs_CTL	2,59699222	3,23921902	Yersinia infection	24
5uM_Menadione_vs_CTL	2,172555633	3,23921902	Coronavirus disease - COVID-19	34
5uM_Menadione_vs_CTL	2,100637263	3,128696177	Shigellosis	35
5uM_Menadione_vs_CTL	2,368410804	3,128696177	Tight junction	27
5uM_Menadione_vs_CTL	2,398080439	2,497537228	Apoptosis	22

Table 24. Interaction partners of NIT2 identified by MS

Protein names	Gene names	Significant in NIT2-BIOID2	-Log Student's T-test p-value
Omega-amidase NIT2	NIT2	+	12,98
10 kDa heat shock protein, mitochondrial	HSPE1	+	9,63
		+	2,50
Caveolin	CAV1	+	3,04
Glutamate dehydrogenase 1, mitochondrial;Glutamate dehydrogenase 2, mitochondrial	GLUD1;GLUD2	+	8,32
Dihydrolipoyllysine-residue succinyltransferase component of 2-oxoglutarate dehydrogenase complex, mitochondrial	DLST	+	6,02
Actin-related protein 2/3 complex subunit 1B	ARPC1B	+	3,85
ATP synthase subunit alpha, mitochondrial	ATP5A1	+	3,39
Unconventional myosin-Id	MYO1D	+	1,86
Tropomyosin alpha-1 chain	TPM1	+	1,73
Myosin light chain 6B	MYL6B	+	1,83
Leucine-rich repeat flightless-interacting protein 2	LRRFIP2	+	3,04
Drebrin	DBN1	+	1,35
		+	2,21
	TPM3	+	1,49
Tropomodulin-3	TMOD3	+	1,49
	TPM1	+	1,99
Tropomyosin alpha-4 chain	TPM4	+	1,91
Lipoamide acyltransferase component of branched-chain alpha-keto acid dehydrogenase complex, mitochondrial	DBT	+	1,55
	TPM2b	+	2,04
Supervillin	SVIL	+	1,55
Interleukin-18 receptor 1	IL18R1	+	1,69
Myosin regulatory light chain 12B;Myosin regulatory light chain 12A	MYL12B;MYL12A	+	1,71
Myosin light polypeptide 6	MYL6	+	2,07
Actin-related protein 2/3 complex subunit 5-like protein	ARPC5L	+	2,56
F-actin-capping protein subunit alpha-1	CAPZA1	+	1,85
Actin, alpha skeletal muscle;Actin, alpha cardiac muscle 1;Actin, aortic smooth muscle;Actin, gamma-enteric smooth muscle	ACTA1;ACTC1;ACTA2;ACTG2	+	2,34
Myosin-9	MYH9	+	2,13
		+	1,72
Actin, cytoplasmic 1;Actin, cytoplasmic 1, N-terminally processed	ACTB	+	2,30
Propionyl-CoA carboxylase alpha chain, mitochondrial	PCCA	+	2,85
Zinc finger protein 512	ZNF512	+	2,00
F-actin-capping protein subunit beta	CAPZB	+	1,48
Myosin-10	MYH10	+	2,53
Actin-related protein 2	ACTR2	+	2,42
Ubinuclein-1	UBN1	+	1,56
Propionyl-CoA carboxylase beta chain, mitochondrial	PCCB	+	2,82
Transcription initiation factor TFIID subunit 4	TAF4	+	2,09
Serum deprivation-response protein	SDPR	+	3,37
Nucleolar transcription factor 1	UBTF	+	2,33
Protein polybromo-1	PBRM1	+	2,27
Polymerase I and transcript release factor	PTRF	+	2,68

9.3 List of figures

Figure 1. Sources of ROS in mammalian cells 2
Figure 2. Cysteine residues and their different oxidation states 4
Figure 3. Mitochondria as a source of ROS and their effects on energy metabolism . 8
Figure 4. Metabolic demands of angiogenesis 11
Figure 5. Glutamine metabolism of endothelial cells 14
Figure 6. The glutaminase II pathway..... 16
Figure 7. Reaction catalyzed by the ω-amidase/NIT2 18
Figure 8. The methionine salvage pathway 19
Figure 9. DAO as a tool to generate intracellular H_2O_2..... 52
Figure 10. Characterization of DAO as a tool to generate intracellular H_2O_2 in HUVECs 53
Figure 11. DAO-derived H_2O_2 oxidizes peroxiredoxins in HUVECs..... 55
Figure 12. A synthetic construct to generate a cell type specific DAO knock-in mouse 56
Figure 13. Characterization of yDAO-HyPer7 construct in HEK293 cells 57
Figure 14. Experimental design 58
Figure 15. Metabolic changes after exposure to different types and concentrations of ROS..... 59
Figure 16. Changes in glutathione metabolism upon exposure to different types of ROS 60
Figure 17. Changes in glycolysis of HUVECs upon exposure to different types of ROS 61
Figure 18. rRNAs are commonly changed upon exposure to different types of ROS 62
Figure 19. Metabolic response by HUVECs upon exposure to H_2O_2..... 64
Figure 20. Exposure to menadione reduces relative isocitrate levels in HUVECs 65
Figure 21. High H_2O_2 affects glutamine metabolism of HUVECs..... 66
Figure 22. The ω-amidase/NIT2 is potentially inhibited by 300 µM H_2O_2 67
Figure 23. BIAM switch assay shows redox-sensitivity of NIT2 68
Figure 24. High concentrations of H_2O_2 are necessary to oxidize NIT2..... 69
Figure 25. Redox-proteomics reveals Cys146 and Cys153 as potentially oxidized in NIT2..... 70
Figure 26. Mutation of Cys146 affects protein stability 71

Figure 27. Ping-pong mechanism for the hydroxaminolysis of succinamate 71
Figure 28. Mutation of Cys146 affects activity and stability of NIT2..... 72
Figure 29. CRISPR/Cas9 mediated knockout of key enzymes of glutamine metabolism in HUVECs 73
Figure 30. Knockout of NIT2 affects proliferation but not migration of HUVECs..... 74
Figure 31. Knockout of NIT2 impairs angiogenic sprouting 75
Figure 32. α-Ketoglutaramate is only detectable in NIT2 knockout cells 76
Figure 33. Deletion of NIT2 reduces α-ketoglutarate levels in HUVECs..... 77
Figure 34. Knockout of the glutamine transaminases reduces methionine levels in HUVECs and increases its α-keto acid analogue (KMBA)..... 78
Figure 35. KGM levels of healthy volunteers 79
Figure 36. Successful knockout of NIT2 in mice..... 80
Figure 37. Workflow of the BioID2 approach to identify interaction partners 80
Figure 38. BioID2 as a tool to identify interaction partners of NIT2 in HUVECs..... 81
Figure 39. NIT2 interacts with key enzymes of mitochondrial glutamine metabolism 82
Figure 40. GLUD1, DLST and HSPE1 are specific interaction partners of NIT2 83
Figure 41. NIT2 localizes in both cytoplasm and mitochondria..... 84
Figure 42. Glutamine metabolism revised 96
Figure 43. Vector map of pLVX2-hDAO..... 130
Figure 44. Vector map of pLVX-hNIT2-BioID2..... 130
Figure 45. Heat map of DEGs after exposure to different types of ROS 131
Figure 46. Vector map of LCV2 131
Figure 47. Volcano plot of DEGs ($p_{adj} < 0.05$) after exposure to different types of ROS 132
Figure 48. Modified cysteines in NIT2 detected by MS..... 133

9.4 List of tables

Table 1. List of chemicals 22
Table 2. List of equipment 25
Table 3. List of materials 27
Table 4. List of buffers and solutions 27
Table 5. Bacterial growth medium 28
Table 6. List of cell culture media 28
Table 7. List of eukaryotic cells 29
Table 8. List of competent cells 29
Table 9. List of synthetic oligonucleotides including overhangs 29
Table 10. List of plasmids 30
Table 11. List of cloning enzymes 30
Table 12. List of antibodies 31
Table 13. List of kits 32
Table 14. List of software 32
Table 15. List of packages 33
Table 16. List of databases 33
Table 17. PCR approach 37
Table 18. PCR program 38
Table 19. Protocol for restriction digestion 38
Table 20. Protocol for DNA ligation 38
Table 21. Total biochemicals (RNA-normalized) changed in untargeted metabolomics approach 59
Table 22. Machine learning approach to predict potentially oxidized cysteine residues in mNIT2 70
Table 23. Pathway enrichment analysis of MACE-Seq data 134
Table 24. Interaction partners of NIT2 identified by MS 135
Table 25. List of abbreviations 139
Table 26. List of amino acid abbreviations 142

9.5 Abbreviations

Table 25. List of abbreviations

AMP	Adenosine monophosphate
AMPK	AMP-activated protein kinase
AMPS	2-Acrylamido-2-methylpropane sulfonic acid
AP	Apurinic/apyrimidinic
ASK1	Apoptosis signal-regulating kinase 1
ATP	Adenosine triphosphate
BH_4	Tetrahydrobiopterin
BIAM	Biotinylated iodoacetamide
BPTES	Bis-2-(5-phenylacetamido-1,3,4-thiadiazol-2-yl)ethylsulfid
bZIP	Basic leucine zipper domain
CAT	Catalase
CCBL	Cysteine-s-conjugate beta-lyase
CHAPS	3-[(3-Cholamidopropyl)dimethylammonio]-1-propanesulfonate hydrate
CREB	Camp response element binding
CRISPR	Clustered regularly interspaced short palindromic repeats
CSF	Cerebrospinal fluid
DAO	D-Amino acid oxidase
DEG	Differentially expressed genes
DLL4	Delta-like 4
DLST	Dihydrolipollysine-residue succinyltransferase
DMSO	Dimethyl sulfoxide
DNA	Deoxyribonucleic acid
DUOX	Dual oxidases
ECs	Endothelial cells
EC-SOD	Extracellular superoxide dismutase
EDTA	Ethylenediaminetetraacetic acid
EGF	Epidermal growth factor
EGTA	Ethylene glycol-bis(β-aminoethyl ether)-n,n,n′,n′-tetraacetic acid
eNOS	Endothelial nitric oxidase synthase
FCS	Fetal calf serum
FMN	Flavin mononucleotide
FOXO	Forkhead family of transcription factors

G6PD	Glucose-6-phosphate dehydrogenase
GABA	γ-Aminobutyric acid
GAD	Glutamic acid decarboxylase
GADD45A	Growth arrest and DNA-damage-inducible protein
GAPDH	Glyceraldehyde 3-phosphate dehydrogenase
GLRX	Glutaredoxins
GLS	Glutaminase
GLUD	Glutamate dehydrogenase
GLUL	Glutamine synthetase
GLUT1	Glucose transporter 1
GR	Glutathione reductase
GSH	Glutathione (reduced)
GSH-Px	Glutathione peroxidase
GSSG	Glutathione (oxidized)
GTK	Glutamine transaminase K
GTL	Glutamine transaminase L
GTP	Guanosine triphosphate
HEK293	Human embryonic kidney cells
HEPES	4-(2-Hydroxyethyl)-1-piperazineethanesulfonic acid
HIF1	Hypoxia-inducible factor-1
HMOX-1	Heme oxygenase-1
HRP	Horseradish peroxidase
HSPE1	10 kDa heat shock protein
HUVECs	Human umbilical vein endothelial cells
IKB	Inhibitor of nuclear factor kappa B
IKK	IkappaB kinase
KEAP1	Kelch-like ech-associated protein 1
KEGG	Kyoto Encyclopedia of Genes and Genomes
αKG	α-Ketoglutarate
αKGDHC	α-Ketoglutarate dehydrogenase complex
KGM	α-Ketoglutaramate
KLF	Krüppel-like factor
KMBA	α-Keto-γ-methylthiobutyrate/2-oxo-4-methylthiobuytric acid
KSM	α-Ketosuccinamate
KYAT	Kynurenine aminotransferase

LCV2	Lenti CRISPR plasmid version 2
LDH-A	Lactate dehydrogenase
MACE	Massive analysis of cDNA ends
MAPK	Mitogen-activated protein kinase
MEKK4	Mitogen-activated protein kinase kinase kinase 4
MS	Mass spectrometry
MTA	5´-Methylthioadenosine
NAD	Nicotinamide adenine dinucleotide
NADPH	Nicotinamide adenine dinucleotide phosphate
NEM	*N*-Ethylmaleimide
NF-κB	Nuclear factor kappa b
NICD	Notch intracellular domain
NIT2	Nitrilase family member 2
NO	Nitrogen monoxide
NOX	NADPH oxidase
NRF2	Nuclear factor erythroid 2-related factor2
NTC	Non target control
NTP	Nucleoside triphosphate
$ONOO^-$	Peroxynitrite
PDHC	Pyruvate dehydrogenase complex
PFKFB3	6-Phosphofructo-2-kinase/fructose-2,6-bisphosphatase-3
PHLDA3	Pleckstrin Homology Like Domain Family A Member 3
PLA	Proximity ligation assay
PLP	Pyridoxal- 5´-phosphate
PPP	Pentose phosphate pathway
PRA	5-Phosphoribosyl-1-amine
PRPP	5-Phosphoribosyl-1-pyrophosphate
PRX	Peroxiredoxin
RET	Reverse electron transfer
RNA	Ribonucleic acid
ROS	Reactive oxygen species
SLC25	Solute carrier family 25
SMC	Smooth muscle cells
$-SO_2H$	Sulfinic acid group
$-SO_3H$	Sulfonic acid group

SOD	Superoxide dismutase
-SOH	Sulfenic acid group
STAT3	Signal transducer and activator of transcription 3
TCA	Tricarboxylic acid
TCAA	Trichloroacetic acid
TF	Transcription factor
TOMM20	Translocase of outer mitochondrial membrane
TRR	Thioredoxin reductase
TRX	Thioredoxin, thioredoxin
VEGF	Vascular endothelial growth factor
VEGFR	Vascular endothelial growth factor receptor

Table 26. List of amino acid abbreviations

Abbreviation	One letter abbreviation	Amino acid name
Ala	A	Alanine
Arg	R	Arginine
Asn	N	Asparagine
Asp	D	Aspartic acid
Cys	C	Cysteine
Gln	Q	Glutamine
Glu	E	Glutamic acid
Gly	G	Glycine
His	H	Histidine
Ile	I	Isoleucine
Leu	L	Leucine
Lys	K	Lysine
Met	M	Methionine
Phe	F	Phenylalanine
Pro	P	Proline
Pyl	O	Pyrrolysine
Ser	S	Serine
Sec	U	Selenocysteine
Thr	T	Threonine
Trp	W	Tryptophan
Tyr	Y	Tyrosine
Val	V	Valine

9.6 Declaration

Except where stated otherwise by reference or acknowledgement, the work presented was generated by myself under the supervision of my supervisors Prof. Dr. Katrin Schröder, Dr. Flávia Rezende and Prof. Dr. Ralf P. Brandes or during my doctoral studies. Quantitative proteomics were carried out by Dr. Ilka Wittig (Proteomics Core Facility, Institute for Cardiovascular Physiology, Goethe-University Frankfurt/Main) and quantitative metabolomics were carried out by Dr. Stephan Klatt (Metabolomics Core Facility, Institute for Vascular Signaling, Goethe-University Frankfurt/Main). Furthermore, untargeted metabolomics were carried out by Metabolon Inc. (Morrisville, North Carolina, USA) and MACE-Sequencing by GenXPro (Frankfurt/Main, Hessen, Germany). The metabolite α-Ketoglutaramate (KGM) was kindly provided by Prof. Dr. Travis T. Denton (Washington University, Spokane, WA, USA). All contributions from colleagues are explicitly referenced in the thesis. The material listed below was obtained in the context of collaborative research:

Figure 25C: Redox-proteomics reveals Cys146 and Cys153 as potentially oxidized in NIT2, Prof. Dr. Eugen Proschak (Pharmaceutical Institute, Goethe-University, Frankfurt), Prof. Dr. Eugen Proschak did the protein modeling and structural representation.

Figure 28 B-D: Mutation of Cys146 affects activity and stability of NIT2, Dr. Steffen Brunst (Pharmaceutical Institute, Goethe-University, Frankfurt), Dr. Steffen Brunst provided the protocol and reagents. Furthermore he helped analyzing the raw data. I did the statistics and the final visualizations.

Figure 32: α-Ketoglutaramate is only detectable in NIT2 knockout cells. Prof. Dr. Travis T. Denton (Washington State University, Spokane, WA, USA) provided the KGM.

Table 22: Machine learning approach to predict potentially oxidized cysteine residues in mNIT2, Marcus Keßler (Molecular Bioinformatics, Goethe-University, Frankfurt/Main), Marcus Keßler ran the algorithm and provided the table.

The following parts of the thesis have been previously published:

Chapter	Published in
1.1.2	partially in Müller *et al.* (2022) [177]
2	in a modified version in Müller *et al.* (2022) [177]
4.2.1	Müller *et al.* (2022) [177]
4.2.2	Müller *et al.* (2022) [177]
5.2	Müller *et al.* (2022) [177]

Figure Number	Published in
9	Müller *et al.* (2022) [177]
10	Müller *et al.* (2022) [177]
11	Müller *et al.* (2022) [177]
14	Müller *et al.* (2022) [177]
15	Müller *et al.* (2022) [177]
16	Müller *et al.* (2022) [177]
17	Müller *et al.* (2022) [177]
18	Müller *et al.* (2022) [177]

9.7 Acknowledgements

9.8 Curriculum vitae

9.9 Publications

Müller N, Warwick T, Noack K, Malacarne PF, Cooper AJL, Weissmann N, Schröder K, Brandes RP, Rezende F. Reactive Oxygen Species Differentially Modulate the Metabolic and Transcriptomic Response of Endothelial Cells. *Antioxidants (Basel)*. 2022 Feb 21;11(2):434. doi: 10.3390/antiox11020434

Pedro Felipe Malacarne, Corina Ratiu, Anna Gajos-Draus, **Niklas Mueller**, Melina Lopez, Beatrice Pflüger-Müller, Xinxin Ding, Timothy Warwick, James Oo, Mauro Siragusa, Carlo Angioni, Stefan Günther, Andreas Weigert, Gerd Geisslinger, Dieter Lütjohann, Wolf-Hagen Schunck, Ingrid Fleming, Ralf Brandes, and Flavia Rezende. Loss of endothelial cytochrome P450 reductase induces vascular dysfunction in mice. *Hypertension*. 2022. (resubmitted after revision, March 2022)

Rezende, F., Malacarne, P. F., **Müller, N.**, Rathkolb, B., Hrabě de Angelis, M., Schröder, K., & P Brandes, R. (2021). Nox4 Maintains Blood Pressure during Low Sodium Diet. *Antioxidants*, *10*(7), 1103.

Schader, T., Löwe, O., Reschke, C., Malacarne, P., Hahner, F., **Müller, N.**, ... & Schröder, K. (2020). Oxidation of HDAC4 by Nox4-derived H2O2 maintains tube formation by endothelial cells. *Redox biology*, *36*, 101669.

Seimetz, Michael; Sommer, Natascha; Bednorz, Mariola; Pak, Oleg; Veith, Christine; Hadzic, Stefan Marija Gredic, Nirmal Parajuli, Baktybek Kojonazarov, Simone Kraut, Jochen Wilhelm, Fenja Knoepp, Ingrid Henneke, Alexandra Pichl, Zeki I. Kanbagli, Susan Scheibe, Athanasios Fysikopoulos, Cheng-Yu Wu, Walter Klepetko, Peter Jaksch, Christina Eichstaedt, Ekkehard Grünig, Katrin Hinderhofer, Miklós Geiszt, **Niklas Müller**, Flavia Rezende, Giulia Buchmann, Ilka Wittig, et al. (2020): NADPH oxidase subunit NOXO1 is a target for emphysema treatmentin COPD. In: *Nature metabolism* 2 (6), S. 532‑546. DOI: 10.1038/s42255-020-0215-8.

Rezende, F., Löwe, O., **Müller, N**., Malacarne, P. F., Pfitzner, M., Walter, M., ... & Schröder, K. (2017). Redox control of renal metabolism and transport function by the NADPH oxidase Nox4. *Free Radical Biology and Medicine*, *112*, 174.

9.10 Selbstständigkeitserklärung

Ich erkläre hiermit, dass ich die im Fachbereich Biochemie, Chemie und Pharmazie der Goethe-Universität Frankfurt am Main zur Promotionsprüfung eingereichte Arbeit mit dem Titel:

„**The ω-Amidase/NIT2 is a novel redox-sensitive key regulator of glutamine metabolism in endothelial cells**“

im Institut für Kardiovaskuläre Physiologie unter Betreuung und Anleitung von Frau Prof. Dr. Katrin Schröder, Herrn Prof. Dr. Ralf P. Brandes und Frau Dr. Flávia Rezende ohne sonstige Hilfe selbst durchgeführt und bei der Abfassung der Arbeit keine anderen als die in der Dissertation angeführten Hilfsmittel benutzt habe. Ich versichere, die Grundsätze der guten wissenschaftlichen Praxis beachtet, und nicht die Hilfe einer kommerziellen Promotionsvermittlung in Anspruch genommen zu haben.

Ich habe bisher an keiner in- oder ausländischen Universität ein Gesuch um Zulassung zur Promotion eingereicht. Die vorliegende Arbeit wurde bisher nicht als Dissertation eingereicht.

Vorliegende Ergebnisse der Arbeit sind zum Teil veröffentlicht in:

Müller N, Warwick T, Noack K, Malacarne PF, Cooper AJL, Weissmann N, Schröder K, Brandes RP, Rezende F. Reactive Oxygen Species Differentially Modulate the Metabolic and Transcriptomic Response of Endothelial Cells. *Antioxidants (Basel)*. 2022 Feb 21;11(2):434. doi: 10.3390/antiox11020434

Frankfurt am Main, März 2022

Niklas Müller